Spring 2021

Source reconstruction in near field scanning for RFI application

Hosseien Rezaei

Department: Electrical and Computer Engineering

Recommended Citation

Rezaei, Hosseien, "Source reconstruction in near field scanning for RFI application" (2021). *Doctoral Dissertations*. 2983.
https://scholarsmine.mst.edu/doctoral_dissertations/2983

SOURCE RECONSTRUCTION IN NEAR FIELD SCANNING FOR RFI APPLICATION

by

HOSSEIN REZAEI VARNOUSAFADERANI

A DISSERTATION

Presented to the Graduate Faculty of the

MISSOURI UNIVERSITY OF SCIENCE AND TECHNOLOGY

In Partial Fulfillment of the Requirements for the Degree

DOCTOR OF PHILOSOPHY

in

ELECTRICAL ENGINEERING

2021

Approved by:

Dr. Daryl Beetner, Advisor
Dr. Jun Fan
Dr. Chulsoon Hwang
Dr. Victor Khilkevich
Dr. Daniel Stutts

PUBLICATION DISSERTATION OPTION

This dissertation consists of the following five articles, formatted in the style used by the Missouri University of Science and Technology:

Paper I, found on pages 4–28, Mechanical Magnetic Field Generator for Communication in the ULF Range, has been published in IEEE Transactions on Antennas and Propagation.

Paper II, found on pages 29–53, Source Reconstruction in Near Field Scanning using Inverse MoM for RFI Application, has been published in IEEE Transactions on Electromagnetic Compatibility.

Paper III, found on pages 54–82, A Methodology for Predicting Near-Optimal Dipole Sources in a Source Reconstruction Implementation, will be submitted to IEEE Transactions on Electromagnetic Compatibility.

Paper IV, found on pages 83–116, Analysis of Imbalanced 2 or 3 Wire VHF LISN Influence to Radiated Emission from AC Cable, will be submitted to IEEE Transactions on Electromagnetic Compatibility.

Paper V, found on pages 117–145, An investigation on the effects of variable complex impedance to the reference plane using post processing in MATLAB, will be submitted to IEEE Transactions on Electromagnetic Compatibility.

ABSTRACT

This research is divided into three major topics. The first topic, mechanical magnetic field generator for communication in the ULF range, is discussed in the first paper. The second topic, source reconstruction in near field scanning for RFI application, is discussed over the course of two papers. The third topic, analysis of imbalanced 2 or 3 Wire VHF LISN, is discussed in the last two papers.

In the first topic, the possibility to use a mechanical system (a rotating magnet) as a source (generator or antenna combined) of the ULF magnetic field is investigated. Ultra-low frequency (ULF) communication systems have advantage over the RF systems in lossy media such as soil or water. A conventional way to create ULF fields is to use coils. It is demonstrated that the mechanical sources have advantage over coils in terms of occupied volume or dissipated power and can be a viable alternative for low-size, weight, and power applications. In the second topic, methods are presented to predict the high-frequency near electric- and magnetic- fields from a component using a Method of Moment (MoM) approach. Additionally, the impact of three major sources of error in near field scans: random measurement noise, cross field coupling, and position error, is investigated on field prediction. A clear decision-making process with examples is provided to guide the user toward selection of the "best" representation. In the third topic, an analysis of an imbalanced two- or three-wire VHF LISN is conducted in terms of its mode conversion and termination impedance. It is demonstrated that an imbalanced termination impedance provides a specified degree of conversion from differential- to common-mode, which can lead to more representative radiated emission test results.

ACKNOWLEDGMENTS

I would like to express my sincere gratitude to Dr. David Pommerenke for guiding me throughout the course of my Ph.D. degree program. I would like to thank my Ph.D. degree advisor, Dr. Daryl Beetner, for his continuous guidance in my research work and enhancing my learning experience through numerous discussions. They guided me in developing both technical and non-technical skill sets, which helped me grow as an individual.

I would like to thank Dr. Jun Fan, Dr. Chulsoon Hwang, Dr. Victor Khilkevich, and Dr. Daniel Stutts for helping me with many useful discussions related to my research work. I would also like to thank all the former and current members of the EMC laboratory for their teamwork and help in my research and coursework. I am proud that I was a member of such an exceptional lab in the EMC area.

I am deeply grateful to my lovely wife, Elham Abedi, for her constant support and encouragement towards achieving this goal. I also extend warm thanks to my family and friends for their encouragement and guidance. I finally thank God, almighty for making all this possible.

This work was supported in part by the National Science Foundation (NSF) under Grant IIP-1916535.

TABLE OF CONTENTS

SECTION

LIST OF ILLUSTRATIONS

PAPER I Page

PAPER II

PAPER III

PAPER IV

PAPER V

LIST OF TABLES

PAPER I Page

PAPER III

PAPER IV

1. INTRODUCTION

1.1. MECHANICAL MAGNETIC FIELD GENERATOR

Magnetically coupled coils are commonly used for near-field magneto-inductive (MI) communication. Normally the MI fields are created using resonant coils. However, due to the high-energy density of permanent magnets, it is possible to create low-frequency magnetic fields of sufficient magnitude by rotating permanent magnets. The first article explores the possibility to use mechanical generators to organize communication in the ULF range by comparing them to the traditional coil sources and proposing an amplitude modulation method.

1.2. SOURCE RECONSTRUCTION IN NEAR FIELD SCANNING

Near-field scanning is commonly used to characterize RFI noise sources. The results of the scan may be used to find an equivalent source representation, which is then used to predict both near-field and far-field behavior of the noise source. The problem of estimating fields next to sources like an IC is solved by representing the noise source using two Method of Moment (MoM) planes such that there is always a representation plane between the true source and the location where fields are estimated. This MoM representation is evaluated based on its ability to estimate fields both above the scan plane and next to the DUT when the scans are noisy and when measurements are only performed in a plane above the DUT. Additionally, a semi-automated source reconstruction method is proposed for finding a near-optimal dipole representation from phase-resolved electric or magnetic field measurements. The study considers field prediction both above and to the side of the DUT with far fields and the total radiated power (TRP). The impact of three major sources of error in near field scans: random measurement noise, cross field coupling, and position error, was investigated on field prediction. A clear decision-making process with examples is provided to guide the user toward selection of the "best" representation.

1.3. ANALYZING THE INFLUENCE OF DIFFERENT TERMINATION ON RADIATED EMISSIONS

Power line EMI noise sources are often rather symmetric with respect to inputs L and N. Some devices, like those using power line communication, intentionally drive differential mode currents. In EMI testing there are conflicting interests: One wants to have a setup which mimics realistic radiation conditions, but the setup needs to be repeatable from a test site to test site. The common-mode, differential mode and CM-DM conversion of power systems leads to resonances and conversion which may differ from site to site, leading to reproducibility problems.

One solution is the usage of LISNs. They suppress resonances, which may reduce the EMI below the values one would experience in real installations, improve repeatability, but introduce a significant problem for compliance in those devices that have strong differential mode current. Real power systems are not symmetric in the higher frequency range, thus, they convert DM to CM. Here an imbalanced LISN is suggested as a solution.

This study analyzes the radiation from a test case e.g, power cable connected to a power line communication device, which can generate a strong DM signal. The device under test (DUT) was terminated to a balanced and an imbalanced LISN with different power networks. It was shown that both LISNs improved test result repeatability for different power nets as the LISNs isolate well. Furthermore, the imbalanced LISN creates a non-perfect termination condition which converts DM current into CM current. This conversion increased the radiation about 12 dB compared to a balanced LISN which has no conversion. This result proves that without imbalance termination, an important mode of emission is not tested, i.e., a potentially serious DM to CM conversion in the AC network which causes strong radiation is ignored.

PAPER

I. MECHANICAL MAGNETIC FIELD GENERATOR FOR COMMUNICATION IN THE ULF RANGE

Hossein Rezaei

Department of Electrical Engineering
Missouri University of Science and Technology
Rolla, Missouri 65409–0050
Tel: 573–308–9313
Email: hrr7d@mst.edu

ABSTRACT

Electromagnetic (EM) fields at radio frequencies (RF) cannot penetrate deep into media with high conductivity such as sea water, wet soil, etc. However, moving to the ultra-low frequency (ULF) range (300 Hz - 3 kHz) allows a considerable range of communication due to the decreased medium loss at low frequencies and a possibility to use the penetrating near field.

Magnetically coupled coils are commonly used for near-field magneto-inductive (MI) communication. Alternatively, it is possible to create ULF magnetic fields of sufficient amplitude by rotating permanent magnets.

In this work, an ULF magnetic field generator has been created using a rotating permanent magnet. It has been shown that the proposed field generator outperforms a conventional coil source (23 dB of field strength for the same volume and dissipated power that is 0.35 W), which can be a considerable advantage for low size, weight, and power

applications. A method to produce amplitude shift keying (ASK) modulation signals using a modulation coil was proposed and analyzed.

It was demonstrated that the inductance of the modulation coil is not critical for achieving acceptable modulation ratios, which opens a possibility for a compact ASK generator design. A simple circuit model and analytical formula for modulation efficiency of the generator was proposed and validated by measurement.

1. INTRODUCTION

Magneto-inductive (MI) communication is a technique commonly used for underwater or underground communication or wireless power transmission, in biomedical applications [1]-[8]. In MI communication, the transmission and reception are accomplished using two coils which are normally tuned to resonance to ensure maximum efficiency [9], [10]. Alternatively, to the coils, permanent magnets can be used for both receiving [2] and generating [11], [12] the penetrating near field, although the intended applications in [2] and [11] are limited to wireless power transfer and biomedical uses.

In this paper, we propose the design of a mechanical magnetic field generator, including the carrier modulation method, and compare its efficiency to the conventional coil sources. The mechanical magnetic field prototype is explained in Section 2. In Section 3, the comparison of efficiencies of coil and rotating magnet MI sources is provided. In Section 4, we proposed ASK modulation method. In Section 5, ASK modulation is calculated from simulation results and compared and measurement. The conclusion is provided in Section 6.

2. MI FIELD GENERATOR

A time-changing magnetic field is created each time the orientation of the magnetic moment of the permanent magnet is altered. The magnetic field of the permanent magnet (at the direction of its magnetic moment) at sufficiently large distances is given by [13]

$$B(r) = \frac{\mu_0 m}{2\pi r^3} \tag{1}$$

where r is the distance from the magnet and m is its magnetic moment. In the quasi-static approximation (which is quite accurate for the near field) the magnetic field vector at the observation point would roughly follow the direction of the magnetic moment vector (at least when the magnetic moment changes direction by 180 degrees, the magnetic field vector would also flip the direction), allowing a time-changing field by changing the orientation of the magnetic moment of the magnet.

The easiest way to create a periodic magnetic field is to rotate a permanent magnet over the axis perpendicular to its magnetic moment. This method was used in the mechanical generator prototype with a diametrically magnetized cylindrical magnet [14] (Figure 1).

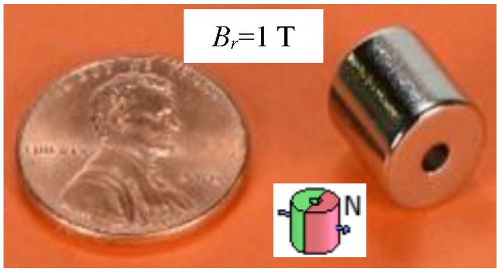

Figure 1. Diametrically magnetized cylindrical magnet R6036DIA.

The dimensions of the magnet are the following: outer diameter – 3/8 inch (9.525 mm), inner diameter – 3/32 inch (2.38 mm), length – 3/8 inch (9.525 mm), and the mass is 4.77g. As shown in Figure 2, the magnet is placed on a brass shaft, which is rotated by two high-speed DC motors [15].

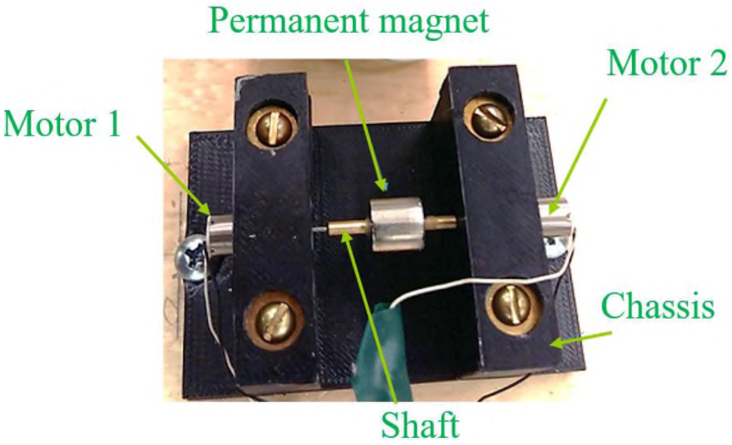

Figure 2. Prototype of the mechanical magnetic field generator.

The shaft is connected directly to the rotors of the motors, such that the magnet is supported by the bearings of the motors. Two motors are used to increase the torque and avoid the need for additional bearings. It should be noted that the permanent magnet should be placed at a considerable distance from the motors (around 1 cm), otherwise the interaction between the rotating magnet and the magnets inside the motors prevents them from running. The entire structure is supported by a plastic chassis. The rotation frequency is determined by the DC voltage applied to the motors and can reach nominally 56,000 rpm, which corresponds to 933 Hz. In the experiments, a frequency close to 700 Hz was reached, which corresponded to 2.5 V DC voltage. Achieving higher rotation speeds requires a well-balanced set-up to avoid excessive vibration.

To detect the magnetic field generated by the magnet a simple solenoid coil was used (Figure 3).

Figure 3. Magnetic field detection coil.

The coil had a diameter of 60 mm and 48 turns of 22 AWG wire. The probe factor of the coil, defined as the ratio of the magnetic B field at the coil location to the voltage induced at the coil terminals, can be calculated analytically. According to Faraday's law the voltage induced at the terminals of the coil exposed to the uniform magnetic field can we written as:

$$v_{coil} = -N \cdot A \frac{dB}{dt}, \tag{2}$$

where N is the number of turns in the coil, A is the area of the coil cross section, and B is the magnetic field parallel to the axis of the coil.

For the harmonic magnetic field with complex amplitude B at frequency ω, (2) can be written as:

$$v_{coil} = -j\omega BNA, \tag{3}$$

and the probe factor is therefore

$$A_{coil} = \left|\frac{B}{v_{coil}}\right| = \frac{1}{\omega NA}. \tag{4}$$

For the dimensions listed above, the probe factor is $A_{coil} = \frac{7.4}{\omega}$ [T/V]. The calculated probe factor was validated using a Helmholtz coil that creates almost a uniform magnetic field close to its axis (Figure 4). The difference between the actual induced voltage in the receiving coil and predicted using the calculated probe factor was 1.3 dB. Such an error was deemed acceptable.

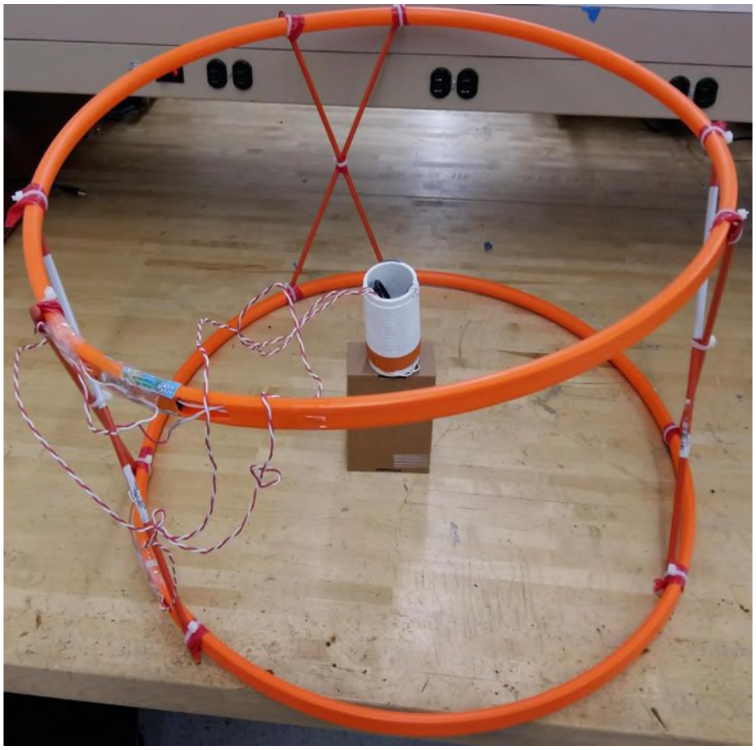

Figure 4. Validation of the receiving coil probe factor using a Helmholtz coil.

The magnetic moment of the permanent magnet can be found by integrating the residual magnetization of the magnet Br over its volume V [2]:

$$m = \int_V \frac{B_r}{\mu_0} dv \tag{5}$$

The calculation can be simplified by assuming a uniform residual field inside the volume as:

$$m \approx \frac{B_r V}{\mu_0}. \tag{6}$$

Using the average value of the residual field (Br) for R6036DIA provided by the manufacturer (1 T), the magnetic moment of the magnet can be estimated using (6) as $m = 0.51\ \mathrm{A \cdot m^2}$.

According to (1), the amplitude of the magnetic field at 1 m from the magnet can be estimated as -140 dBT, which agrees well with the measured value of -141 dBT obtained by measuring the voltage induced in the receiving coil and applying the probe factor to it. The achieved rotation speed of 700 Hz corresponded to 0.35 W of power consumed by the motors. This value will be used as a reference for the efficiency comparison in the next section. Field strength at greater distances can be calculated using (1). The useful communication range can be estimated based on the known sensitivity of the receiver.

3. COMPARISON OF EFFICIENCIES OF COIL AND ROTATING MAGNET MI SOURCES

Of course, similar field intensities can be achieved by a conventional coil structure driven by the sinusoidal current. Furthermore, new coil designs – e.g., metamaterial, ferrite core coils, or MIMO – were proposed recently to enhance the magnetic field or improve channel capacity.

The magnetic field of a multi-turn coil with a ferrite core can be increased by about 10 dB over its air core counterpart [16]. However, high permeability materials are susceptible to saturation in the presence of strong magnetic fields [17] which does not allow use of these solutions at magnetic field strengths comparable to that of permanent neodymium magnets (around 1 T).

Using metamaterials increases the effectiveness of the coil significantly [18]-[19]. Unidirectional [19], bidirectional [20], or tri-directional [21] metamaterial coils can generate up to about a 20 dB stronger field compared to a conventional coil of the same size at a resonance frequency. Nevertheless, intrinsic resonance of metamaterial coils would result in a narrow bandwidth of the communication system and low data exchange rates because of already low carrier frequencies of MI communication (typically hundreds of Hz).

To address this problem MIMO coil antenna arrays are proposed to increase MI communication bandwidth [22]. Each element in the array is resonant at its own frequency, but the antenna array as a whole system has a resonant frequency which might be different from its elements.

Although MIMO antenna arrays improve channel capacity in MI communications, the need for multiple coils increases the volume, cost, and complicates the design process of the system.

As will be demonstrated further, the proposed mechanical generator can generate up to about 24 dB stronger magnetic field compared to a conventional coil of the same size, which is comparable with recently reported field enhancement with metamaterial coil (for equal efficiencies) [18]-[19]. This might be an important factor for low size, weight, and power applications. In contrast to the metamaterial coils which are designed to work at a resonance frequency with limited bandwidth, the proposed mechanical generator allows tuning the carrier frequency easily just by changing the rotation speed of the DC motors and modulate at fast rates.

The efficiency of the near field generator is difficult to define rigorously because if the radiation loss is neglected (which is the case in this study), such a generator does not dissipate any energy through the magnetic field. Nevertheless, the energy is dissipated in the generator itself (in the motor or in the coil due to the Ohmic loss in the wire). Since the role of the generator is to produce the magnetic field of a certain intensity, it makes sense to define the efficiency as the generated field intensity per amount of power lost in the generator.

Following this definition, the generators can be compared by, for example, amount of lost power needed to generate fields of equal intensity, or alternatively by the field intensity corresponding to the same power of loss. The latter definition is used further in the study.

Another important parameter is the volume occupied by the generator. It is easy to create a coil that would produce a stronger field than the permanent magnets (for equal lost power), but at the expense of occupying a considerably larger volume.

This can be demonstrated by considering the following coil model. Suppose a copper wire of diameter D_w is wound around the cylindrical air core of radius R_c in N_t turns and N_l layers (Figure 5).

Figure 5. Photo of a typical coil illustrating the parameter definition of the coil model.

The magnetic field generated by each turn at a distance r along the axis of the coil core can be calculated as follows [23]:

$$B_t = \frac{\mu_0 I R_t^2}{2\left(\sqrt{r^2 + R_t^2}\right)^3}, \tag{7}$$

where I is the current in the turn, R_t is the turn radius. Because of the layered structure of the coil model all turns have different radii, and the distance to the observation point is also different due to the length of the coil. In order to simplify the field calculation, the following approximations are used: 1) the distance to the observation point is equal for all turns (which corresponds to the case when the distance to the observation point is much larger than the length of the coil); and 2) the mean turn radius R_m is used for all turns, which is calculated as:

$$R_m = \frac{R_{min} - R_{max}}{2} + R_{min}, \tag{8}$$

where $R_{min} = R_c - \frac{2t+D_w}{2}$ and $R_{max} = R_{min} + N_l(D_w + 2t)$ are the minimum and maximum radii of turns, and t is the thickness of the insulator which is considered to be 10% of the wire diameter in (8).

The field generated by the coil is, therefore, calculated as:

$$B_{coil} \approx \frac{\mu_0 I R_m^2}{2\left(\sqrt{r^2 + R_m^2}\right)^3} N_t. \tag{9}$$

It is obvious that by increasing the current in the coil it is possible to achieve any desired field strength. Therefore, to make the comparison to the mechanical source meaningful, the dissipated power in the coil is required to be equal to the power consumed by the rotating magnet source achieved in the experiment described above (0.35 W). This condition ensures equal efficiencies of both sources in terms of dissipated power per unit of the generated magnetic field (in the case of equal field strength generated).

The current in the coil is therefore calculated as:

$$I = \sqrt{P_{magnet}/R_{coil}}, \tag{10}$$

where $P_{magnet} = 0.35\ W$ and R_{coil} is the resistance of the coil wire:

$$R_{coil} = \frac{\rho L_w}{A_w}, \tag{11}$$

where ρ is the copper resistivity ($1.73 \cdot 10^{-8}$ Ohm $\cdot$ m), L_w is the wire length, and $A_w = \pi\left(\frac{D_w}{2}\right)^2$ is the cross-section area of the wire. The length of the wire is estimated as:

$$L_w = 2\pi R_m \lceil N_t/N_l \rceil, \tag{12}$$

where N_t is number of turns and $\lceil\cdot\rceil$ is the operator of rounding up to the nearest integer which is needed to avoid a physically impossible number of turns (N_t) to number of layers (N_l) ratios below 1.

The volume occupied by the coil is calculated as:

$$V_{coil} = A_{coil} L_{coil}, \tag{13}$$

where $A_{coil} = \pi[R_{min} + N_l(D_w + 2t)]^2$ is the cross-section area of the coil, $L_{coil} = (D_w + 2t)\lceil N_t/N_l \rceil$ is the length of the coil.

The coil model has therefore four parameters: number of turns N_t, number of layers N_l, wire diameter D_w, and core radius R_c.

The optimal coil design is defined as creating the largest possible magnetic field strength (at a given distance) for a specified volume. Since both field strength (9) and volume (13) are non-linearly related to the parameters of the coil, analytical optimization is problematic, and a random one is performed instead. To perform the random optimization all parameters of the coil model are represented as random variables as:

$$P_i = 10^{X_i}, \tag{14}$$

where the order of magnitude of the parameter $X_i = \text{unif}(X_i^{min}, X_i^{max})$ is the uniformly distributed random number on the interval (X_i^{min}, X_i^{max}), i.e., all parameters are exponentially distributed (this results in more uniform distribution of designs when plotted in the logarithmic scale). For each combination of parameters, the field strength at a distance of 1 m and the coil volume are calculated. Eventually 50,000 combinations of the input parameters are analyzed with the limits specified in Table 1.

Table 1. Limits of the coil parameters.

Parameter	Minimum order X^{min}	Maximum order X^{max}	Minimum value P^{min}	Maximum value P^{max}
Number of turns	0	2	1	100
Number of layers	0	2	1	100
Wire diameter	-5	-3	0.01 mm	1 mm
Core radius	-2	-1	1 cm	10 cm

The resulting designs are plotted in Figure 6 as blue dots on the field intensity/volume chart with the orange dot representing the rotating magnet field source.

As seen in the figure, the coil of comparable volume would produce the magnetic field which is approximately 24 dB lower than the field generated by the magnet (-164 dBT vs -140 dBT). Therefore, the smallest conventional coil capable of producing the field of the same strength (for 0.35 W dissipated power in Figure 6) would occupy 30 times more space than a rotating magnet ($2 \cdot 10^{-5}\ m^3\ vs\ 6.4 \cdot 10^{-7}\ m^3$). To organize a bidirectional communication, the system needs to be equipped with a receiver. Potentially the magnet of the mechanical generator can be used as a mechanical detector of magnetic field [12]; however, the feasibility of this approach requires additional investigation. Alternatively, the modulation coil, which is introduced in the next section, can be used as the receiving antenna. Of course, introduction of the additional coil increases the overall volume occupied by the system.

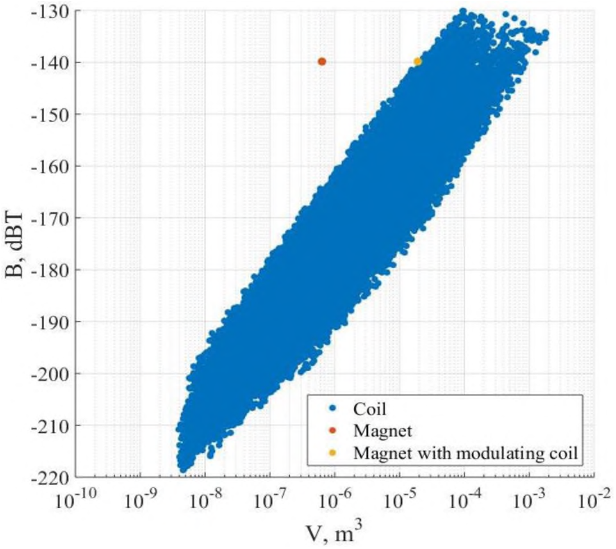

Figure 6. Comparison of magnet and coil sources in terms of field strength at 1 m and occupied volume.

4. ASK MODULATION METHOD FOR THE ROTATING MAGNET GENERATOR

The source of continuous sinusoidal signal is virtually useless for communication and requires a modulation method. The easiest way to achieve modulation in the rotating magnet generator is to change the rotation frequency implementing the phase or frequency modulation of the generated signal. However due to large inertia of the magnet and low torque and power of the high-speed motors, only very small modulation bandwidths can be achieved using this method.

Alternatively, an amplitude modulation (or more precisely, amplitude shift keying - ASK) can be achieved by placing the rotating magnet inside a modulation coil loaded by a variable resistor (a switch) such that the magnetic field vector rotates in the longitudinal plane of the coil. The principle of operation of this method is demonstrated by the following analysis.

The magnet placed inside the modulation coil will generate the inductive EMF in it. The magnet itself is not affected by the coil (assuming that the back EMF effect is neglected). In this case the magnet can be represented by a coil driven by an AC current source, which is coupled to the modulation coil. Both the magnet and the modulation coil are coupled to the receiving coil. The entire model is shown in Figure 7.

The inductor L1 driven by the AC current source SRC1 represents the rotating magnet. The inductor L2 (modulation coil) is relatively strongly coupled to the inductor L1 (magnet) and is loaded by the resistor Rs (switch). Both coils L1 and L2 are weakly coupled to the receiving coil L3. The coupling in the circuit is described by the coupling coefficients $k_{12} = M_{12}/\sqrt{L_1 L_2}$, $k_{13} = M_{13}/\sqrt{L_1 L_3}$, and $k_{23} = M_{23}/\sqrt{L_2 L_3}$. Since the coils L1 and L2 are in the vicinity of one another, and the coil L3 is placed at a large distance from L1 and L2, the following conditions are true: $k_{12} \gg k_{13}$ and $k_{12} \gg k_{23}$.

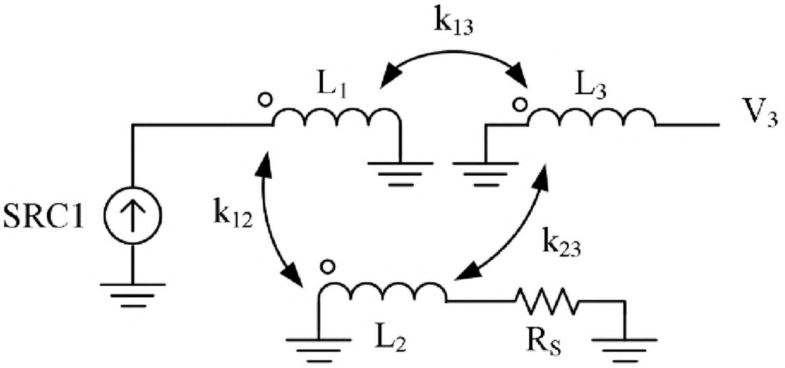

Figure 7. Model of the AM modulation for the rotating magnet source.

The current I_1 in the inductor L1 is set by the current source which induces the EMF in the inductor L2; at the same time, the contribution of the current in the inductor L3 to the current in L2 is negligible because of the weak coupling, therefore, the EMF induced in the L2 is:

$$V_2 = -j\omega M_{12} I_1, \tag{15}$$

and the current in L2 is:

$$I_2 = -\frac{j\omega M_{12} I_1}{R_s + j\omega L_2}. \tag{16}$$

Both currents I_1 and I_2 induce the EMF in the inductor L3:

$$V_3 = -j\omega M_{13} I_1 - j\omega M_{23} I_2. \tag{17}$$

By substituting (16) into (17) the EMF V_3 can be expressed as:

$$V_3 = I_1 \frac{\omega^2 (M_{13} L_2 - M_{12} M_{23}) - j\omega M_{13} R_s}{R_s + j\omega L_2}. \tag{18}$$

Equation (18) describes the steady state amplitude of the voltage induced in the receiving coil, which depends on the resistance of the switch R_s.

Assuming the resistance of the switch is infinite in the open circuit condition $R_{s,oc} = \infty$ and is equal to some constant value in the short-circuit condition $R_{s,sc} = R_0$ (representing the residual resistance of the switch and the resistance of the modulation coil), two possible amplitudes of the induced voltage can be found as

$$V_{3,sc} = I_1 \frac{\omega^2 (M_{13} L_2 - M_{12} M_{23}) - j\omega M_{13} R_0}{R_0 + j\omega L_2}, \tag{19}$$

$$V_{3,oc} = j\omega M_{13} I_1.$$

Two different amplitudes in (19) allow implementing the ASK modulation with the ratio of values (modulation ratio)

$$K = \frac{V_{3,sc}}{V_{3,oc}} = \frac{(M_{13} L_2 - M_{12} M_{32}) - jM_{13} R_0/\omega}{jM_{13} R_0/\omega - L_2 M_{13}}. \tag{20}$$

Expressing the mutual inductances through the coupling coefficients shows the modulation ratio is

$$K = \frac{k_{13}\left(1 + \frac{R_0}{j\omega L_2}\right) - k_{12} k_{23}}{-k_{13}\left(1 + \frac{R_0}{j\omega L_2}\right)}. \tag{21}$$

Introducing the effective coupling coefficient from the magnet to the receiving coil

$$k'_{13} = k_{13}\left(1 + \frac{R_0}{j\omega L_2}\right), \tag{22}$$

the modulation ratio can be expressed as:

$$K = k_{12} \frac{k_{32}}{k'_{13}} - 1. \tag{23}$$

In the case when the resistance of the switch/coil is negligible relative to the reactive impedance of the modulation coil (i.e., when $R_0 \ll |j\omega L_2|$), the modulation ratio becomes

$$K = k_{12}\frac{k_{32}}{k_{13}} - 1. \tag{24}$$

In this situation, the modulation ratio is determined solely by the coupling coefficients between the magnet (L1) and modulation coil (L2), between both of them to the receiving coil (L3) and does not depend on coil inductances. In practice the short circuit resistance is not always negligible, which increases the absolute value of the modulation ratio (23) (i.e., makes the modulation less efficient) relative to (24).

The ratio between the amplitudes (23) can be related to the modulation index, which is the ratio between the modulation amplitude (or half difference between the modulation levels $M = \frac{V_{3,oc} - V_{3,oc}K}{2} = V_{3,oc}\frac{k_{12}k_{23}}{2}$) and the carrier amplitude (or the average between two modulation levels

$A = \frac{V_{3,oc} + V_{3,oc}K}{2} = V_{3,oc}\frac{2k'_{13} - k_{12}k_{23}}{2}$) as

$$m_A = \frac{M}{A} = \frac{1-K}{1+K} = \frac{k_{12}k_{23}}{2k'_{13} - k_{12}k_{23}}. \tag{25}$$

The analysis presented above is simplified, as it does not take into account transitions between the high/low impedances in the modulation coil and assumes steady state signals for both states of the modulation coil (short and open). However, as numerical simulation of circuit in Figure 7 shows, the accuracy of estimation (25) is good. For example, the first harmonic of the side band of the voltage in the receiving coil V_3 obtained numerically for $R_0 = 0$, $k_{12} = 0.8$, $k_{13} = k_{23} = 1 \cdot 10^{-4}$ with $f_c = 1$ kHz and $f_{AM} = 123$ Hz, and 50% duty cycle has a value of -7.5 dBc as Figure 8 demonstrates.

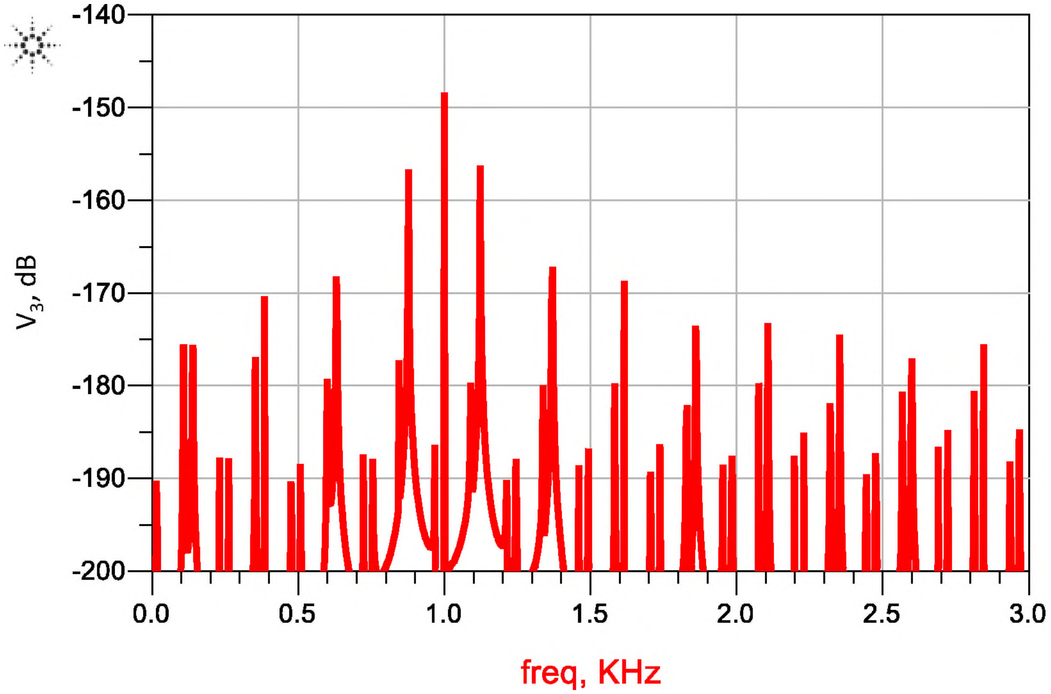

Figure 8. Spectrum of the AM modulated voltage in the receiving coil for $R_0 = 0$ $k_{21} = 0.8$, $f_c = 1$ kHz, $f_{AM} = 123$ Hz, 50% duty cycle. Obtained using transient analysis.

A similar value can be determined using the approximated analysis presented above. In a one-tone AM modulation, the carrier to side band ratio is $m_{AM}/2$. In the circuit at Figure 7 the modulation is performed using a rectangular signal, which has an increased amplitude of the first harmonic compared to the sinusoidal signal of the same amplitude. The value of the first harmonic of the rectangular waveform of amplitude M is $M_1 = \frac{4M}{\pi} sin\, \pi \frac{t_p}{T}$, where t_p is the pulse width, and T is the period of the signal. For the 50% duty cycle signal with unit amplitude the first harmonic amplitude is: $M_1 = \frac{4}{\pi}$. Therefore the relative amplitude of the first harmonic of the side band estimated using (25) for $k_{21} = 0.8$ is $S_1 = \frac{m_A}{2} M_1 = \frac{k_{12}k_{23}}{2k_{13} - k_{12}k_{23}} \frac{2}{\pi} = 0.42$, corresponding to -7.44 dBc, which is very close to the value obtained by a circuit simulator.

To test the ASK modulation method described above, the rotating magnet was placed inside the coil as illustrated in Figure 9.

The coil in Figure 9 was shorted by the parallel channels of six low-channel resistance MOSFETS (TPHR6503PL, on-channel resistance 0.4 mΩ), driven by the signal generator at 10-500 Hz as shown in Figure 10.

A typical signal induced in the receiving coil in the set-up in Figure 9 is shown in Figure 11, demonstrating ASK modulation. As shown in Figure 11, frequency of the carrier and the modulation signals are about 440 Hz and 107 Hz, respectively, with a modulation ratio of about 0.32.

Even though no optimization of the ASK prototype was performed, the size of prototype ($1.88 \cdot 10^{-5}\, m^3$) is close to the smallest coil ($1.8 \cdot 10^{-5}\, m^3$) capable of producing the field of the same strength (see Figure 6).

Further minimization of the modulation system might create the mechanical source outperforming the conventional MI coil.

Knowing that the modulation ratio in ideal circumstances does not depend on the inductance of the modulation coil, it might be possible to create the effective ASK system even with smaller modulation coil.

An obvious solution would be to wind the modulation coil as close to the magnet as possible. However, as experiments show, when the modulation coil becomes too strongly coupled to the magnet, the inductive force applied to the magnet when the modulation coil is switched becomes too strong, which leads to undesirable effects such as carrier frequency decrease, increased power consumption, and parasitic frequency modulation.

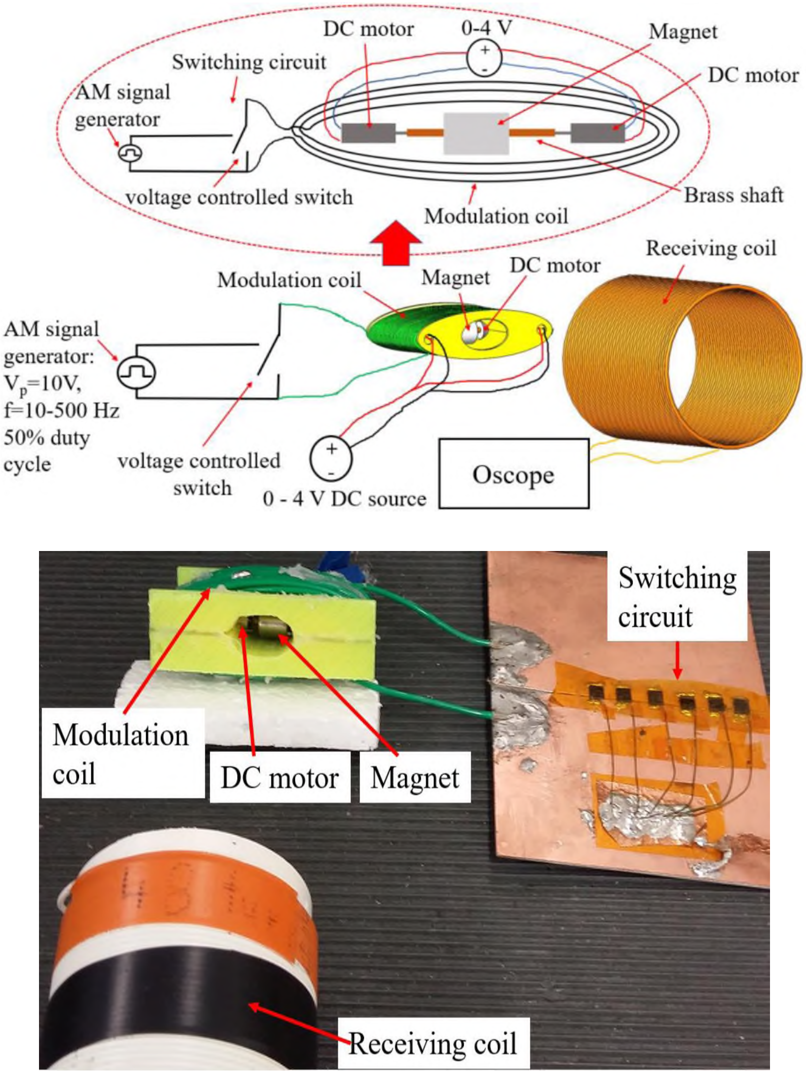

Figure 9. ASK modulation prototype.

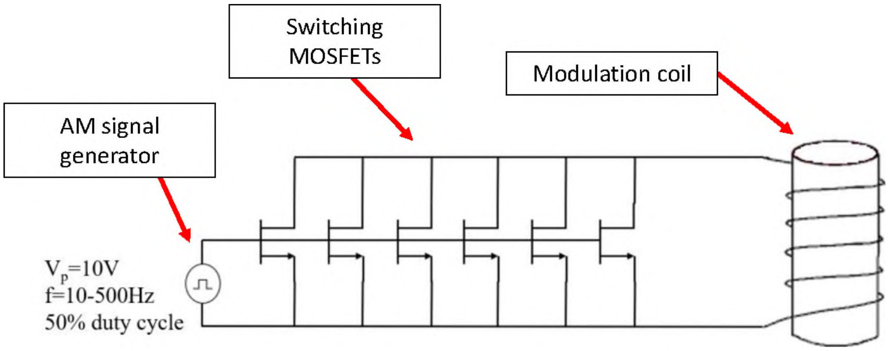

Figure 10. Circuit for the ASK modulation.

5. ESTIMATION OF THE COUPLING BETWEEN THE MAGNET AND THE MODULATION COIL

In order to design the magnetic generator with ASK the coupling coefficients k_{12}, k_{13}, k_{23} need to be estimated. This can be achieved using electromagnetic simulation. A magnetostatic solver in CST [24] can be used to determine the coupling coefficients in a model shown in Figure 12.

The model corresponds to the prototype in Figure 9, with three coaxial coils. Coils 2 and 3 reproduce the dimensions of the modulation and receiving coil, and coil 1 – roughly the dimensions of the magnet (the magnet shape cannot be modelled exactly because its magnetic moment rotates perpendicular to the magnet symmetry axis).

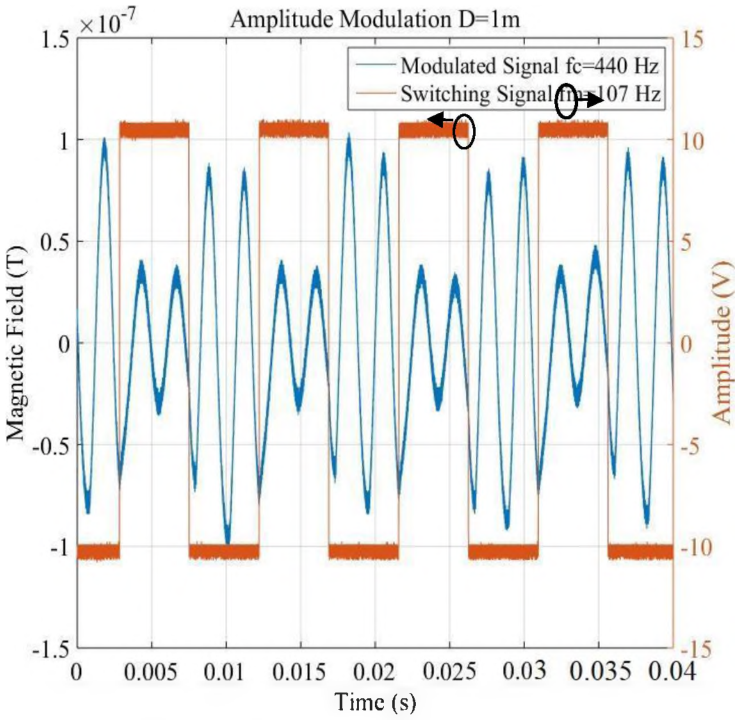

Figure 11. Measured time domain waveform of the AM modulated signal.

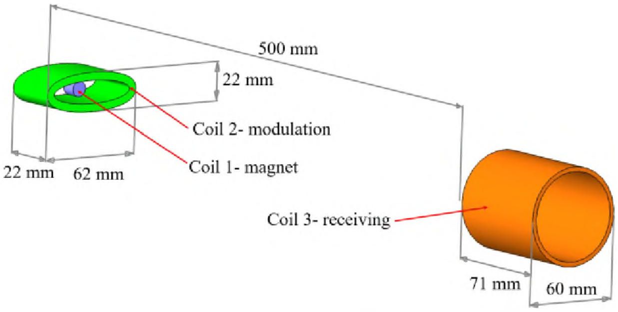

Figure 12. EM model for the coupling coefficient calculation.

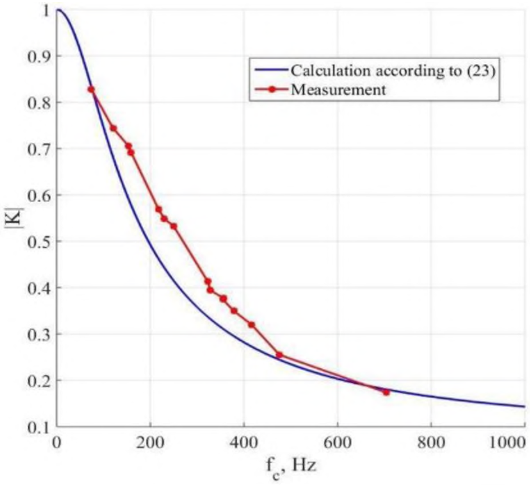

Figure 13. Measured and calculated modulation ratio.

The simulation in Figure 12 resulted in the following values of the coupling coefficients: $k_{12} = 0.14$, $k_{23} = 0.038$, and $k_{13} = 48 \cdot 10^{-4}$. The inductance of the modulation coil is 34 µH and its resistance is 26 mΩ. Using the values above the absolute value of the modulation ratio was calculated according to (23). Also, the modulation ratio was measured by recording waveforms similar to one in Figure 11 at different carrier frequencies. Both measured and calculated ratios are presented in Figure 13. As the figure demonstrates, the EM simulation with (23) estimates the modulation ratio with acceptable accuracy.

6. CONCLUSION

Analysis of the rotating permanent magnet in terms of its efficiency was conducted. It was demonstrated that the rotating magnet source outperforms a conventional coil source by a large margin (23 dB of field strength for the same volume and dissipated power), which might be a considerable advantage for low size, weight, and power applications.

A method to produce ASK signals using a modulation coil was proposed and analyzed. It was demonstrated that the inductance of the modulation coil is not critical for achieving acceptable modulation ratios, which opens a possibility for a compact ASK generator design.

A simple circuit model and analytical formula for modulation efficiency of the generator was proposed and validated by measurement. Besides modulation, the modulation coil can be used as a receiving antenna in a bi-directional communication system.

Modulation coil increases the overall volume of the system, reducing its efficiency to the levels comparable to that of the conventional coil generator. Further optimization of the system is needed to surpass the coil generator efficiency.

REFERENCES

[1] M. C. Domingo, "Magnetic Induction for Underwater Wireless Communication Networks," *IEEE Trans. on Antennas and Propagation*, vol. 60, no. 6, June 2012.

[2] V. R Challal, J. Oscar, M. Miranda, and D. P Arnold, "Wireless power transmission to an electromechanical receiver using low-frequency magnetic fields," *Smart Materials and Structures*, vol. 21, pp. 1-11, 2012.

[3] A. Kurs, A. Karalis, R. Moffatt, J. D. Joannopoulos, P. Fisher and M. Soljavcic, “Wireless power transfer via strongly coupled magnetic resonances,” *Science*, vol. 317, pp. 83–86, Jul. 6, 2007.

[4] F. C. Flack, E. D. James, and D. M. Schlapp, “Mutual inductance of air-cored coils - effect on design of radio-frequency coupled implants,” *Med. Biol. Eng. Comput*er, pp. 79-85, Jan. 1971.

[5] R. Bansal, “Near-field magnetic communication,” *IEEE Antennas and Propagation Magazine*, vol 46, no. 2, April 2004.

[6] C. Bunszel, “Magnetic induction: a low-power wireless alternative,” *RF Design*, vol. 24, no. 11, pp. 78-80, November 2001.

[7] M. P. Theodoridis and S. V. Mollov, “Distant Energy Transfer for Artificial Human Implants,” *IEEE Trans. On Biomedical Engineering*, vol. 52, no. 11, pp. 1931-1938, Nov. 2005.

[8] G.Wang, W. Liu, M. Sivaprakasam, and G. Kendir, “Design and analysis of an adaptive transcutaneous power telemetry for biomedical implants,” *IEEE Trans. Circuits Syst. I*, Reg. Papers, vol. 52, no. 10, pp. 2109–2117, Oct. 2005.

[9] Zhi Sun and Ian F. Akyildiz, “Underground Wireless Communication using Magnetic Induction,” *ICC’09 Proceedings of the 2009 IEEE international conference on Communications*, pp. 4234-4238, June 2009.

[10] N. D. N. Donaldson and T. A. Perkins, “Analysis of resonant coupled coils in the design of radio frequency transcutaneous links,” *Med. Biol. Eng. Comput.*, vol. 21, no. 5, pp. 612–627, Sep. 1983.

[11] H. Jiang, J. Zhang, D. Lan, K. K. Chao, S. Liou, H. Shahnasser, R. Fechter, S. Hirose, M. Harrison, and S. Roy, “A Low-Frequency Versatile Wireless Power Transfer Technology for Biomedical Implants,” *IEEE Trans. on biomedical circuits and systems*, vol. 7, no. 4, August 2013.

[12] O. C. Fawole, and M. Tabib-Azar, “An Electromechanically Modulated Permanent Magnet Antenna for Wireless Communication in Harsh Electromagnetic Environments,” *IEEE Trans. on Antennas and Propagation*, vol. 65, no. 12, pp. 6927-6936, Dec. 2017.

[13] A. J. Petruska and Jake J. Abbott, “Optimal Permanent-Magnet Geometries for Dipole Field Approximation,” *IEEE Trans. on Magnetics*, vol. 49, no. 2, Feb. 2013.

[14] K&J Magnetics, Inc. [Online]. Available: https://www.kjmagnetics.com/proddetail.asp?prod=R6036DIA

[15] NdFeB HM Motor Large torque 615 Hollow cup motor 3.4-3.7V 52000-56000 RPM Hot, "https://www.ebay.com/i/322427122000?chn=ps".

[16] R. DeVore and P. Bohley, "The electrically small magnetically loaded multiturn loop antenna," *IEEE Trans. On Antennas and Propagation*, vol. AP-25, no. 4, pp. 496–505, Jul. 1977.

[17] B. E. Huey and A. L. Anderson, "Active Field Cancellation to Prevent Saturation in Ferromagnetic-Core Loop Antennas," *IEEE Trans. On Electromagnetic Compatibility*, vol. 60, no. 6, pp. 1686–1699, Dec. 2018.

[18] Y. Cho, S. Lee, D. H. Kim, H. Kim, C. Song, S. Kong, J. Park, C. Seo, and J. Kim, "Thin Hybrid Metamaterial Slab with Negative and Zero Permeability for High Efficiency and Low Electromagnetic Field in Wireless Power Transfer Systems," *IEEE Trans. on Electromagnetic Compatibility*, vol. 60, no. 4, pp. 1001-1009, August 2018.

[19] H. GUO, Z. SUN, J. Sun, AND N. M. Litchinitser, "M2I: Channel Modeling for Metamaterial-Enhanced Magnetic Induction Communications," *IEEE Trans. On Antennas and Propagation*, vol. 63, no. 11, pp. 5072-5087, Nov. 2015.

[20] V. P. Pathak, V. Kumar, and R. K. Barik, "Magnetic Induction Communication based Transceiver Coil and Waveguide Structure Modeling for Non-Conventional WSNs," *International Conference on Computing, Communication and Network Technologies (ICCCNT)*, vol. 60, no. 6, pp. 1–7, July 2018.

[21] H. Guo and Z. Sun, "Full-duplex Metamaterial-enabled Magnetic Induction Networks in Extreme Environments," *IEEE Conference on Computer Communications (IEEE INFOCOM)*, pp. 558-566, April 2018.

[22] H.-J. Kim, J. Park, K.-S. Oh, J. P. Choi, J. E. Jang, and J.-W. Choi, "Near-Field Magnetic Induction MIMO Communication Using Heterogeneous Multipole Loop Antenna Array for Higher Data Rate Transmission," *IEEE Trans. on Antennas and Propagation*, vol. 64, no. 5, pp. 1952-1962, May 2016.

[23] F. Fiorillo, "Measurement and Characterization of Magnetic Materials," Amsterdam: Elsevier, 1st edition, 2004, pp. 106-108.

[24] Magneto-static solver in CST [Online]. Available: https://www.cst.com/products/cstems/solvers/solvermagnetostatics

II. SOURCE RECONSTRUCTION IN NEAR FIELD SCANNING USING INVERSE MOM FOR RFI APPLICATION

Hossein Rezaei

Department of Electrical Engineering
Missouri University of Science and Technology
Rolla, Missouri 65409–0050
Tel: 573–308–9313
Email: hrr7d@mst.edu

ABSTRACT

The ability to predict the electric and magnetic fields generated by a component can solve many in-system interferences problems before they occur. Methods are presented to predict the high-frequency near electric- and magnetic- fields from a component using a Method of Moment (MoM) approach. The current representation is estimated from a near electric-field scan by solving the electric field integral equation (EFIE). The reconstruction method was validated with measurements of a test board containing a buffer IC. The current representation was shown to accurately predict fields at locations both above and to the side of the buffer with less than a 3.5 dB average error. Here, a near-field scan was only performed on a flat plane above the emitter and was used to predict sources to the side of the emitter.

To accurately predict fields to the side of the emitter, the current representation must be defined on a surface between the emitter and the prediction location. An error analysis was performed to understand the impact of scan plane parameters like the size of

the scan plane, the size of the current representation, and the relative distance between the current representation and the estimated fields on prediction accuracy.

1. INTRODUCTION

Due to the complexity and reduced size of new wireless products, it is important to predict the potential for radio frequency interference (RFI) between components, like from integrated circuits (ICs) and high-speed traces to nearby antennas. Unwanted coupling from high-frequency components may degrade the radio frequency (RF) performance of the wireless receivers. Potential problems can be mitigated by predicting the near electric and magnetic fields generated by components early in the design process, and then modifying the design to minimize coupling issues.

Near-field scanning is commonly used to characterize RFI noise sources. The results of the scan may be used to find an equivalent source representation, which is then used to predict both near-field and far-field behavior of the noise source. One representation is the equivalent dipole method [1, 2], which represents near electric and magnetic fields using an array of infinitesimal electric and/or magnetic dipoles. The amplitude and phase of each dipole is set to best reconstruct electric and magnetic fields measured near to the source.

In another representation, noise sources are represented with a Huygens box, where tangential electric and magnetic fields on a surface entirely enclosing the source or a surface only between the source and the victim are set to values which best reconstruct the scanned fields [3, 4]. These fields on the Huygens box may then be treated as sources to generate fields outside of this surface [3, 4]. Another approach for representing noise sources is related to the electromagnetic solution carried out by the method of moments (MoM). Practically, this method is based on the theorem of equivalent surface currents. Essentially, electric, and magnetic currents on a surface allow prediction of the fields generated by the source [5]. Conversely, if the measured fields are known one can estimate source currents by solving an inverse problem [5 - 7]. Current distributions can be found from known electric or magnetic fields, or a combination of the two.

In the following study, a current representation is inferred from near electric fields measured only in a plane above an emitter of interest. To accurately reconstruct the current representation, phase-resolved near field data was used. The inferred representation was then used to estimate fields both above the scan plane and on a vertical plane located to the side of the emitter. The fields to the side of the emitter may lie above or below the scan plane, so the measurement may not entirely capture the characteristic of these fields. This scenario is of interest in RF de-sense applications since measurements can often only be performed above the emitter, but one is interested in coupling to the side, for example when an IC couples to a nearby antenna on the same printed circuit board. This coupling could be estimated using an approach like the one in [8], where transfer coefficients are calculated between a victim antenna and equivalent dipoles representing the noise source in order to estimate the RFI. For the work presented here, the transfer coefficient would be calculated using a MoM representation.

In the following sections, methods will be derived to estimate current sources from near electric field measurements. The accuracy of the approach will be studied through simulations of the fields generated by a trace and an IC, based on the ability of the current sources to accurately reconstruct fields both above and to the side and the emitter. As the scan is made in a plane above the emitter, and sources to the side of the emitter are estimated imperfectly, a study of scan and estimation parameters is conducted to better understand what errors can be expected in realistic measurements. Measurement over a real IC package were performed to validate the proposed methods.

2. MOM BASED CURRENT RECONSTRUCTION METHOD

An MoM representation of near-field sources can be found by solving [9 - 11]:

$$E = -j\omega A - \nabla\phi \tag{1}$$

where A, the magnetic vector potential, and ϕ, the scalar electric potential, can be expressed as [9 - 11]:

$$\mathrm{A(r)} = \mu \int_S \vec{J}\left(\vec{r'}\right) G_0(\vec{r},\vec{r'})dS' \tag{2}$$

$$\phi(\mathrm{r}) = \frac{1}{\varepsilon}\int_S \sigma(\vec{r'})G_0(\vec{r},\vec{r'})dS' \tag{3}$$

where J is the source current and σ is surface charge density. The Green's function in a homogeneous medium is defined by:

$$G_0\left(\vec{r},\vec{r'}\right) = \frac{e^{-jk\left|\vec{r}-\vec{r'}\right|}}{4\pi\left|\vec{r}-\vec{r'}\right|} \tag{4}$$

where $k = \omega\sqrt{\varepsilon\mu} = 2\pi/\lambda$ is the wavenumber and λ is the wavelength. The permeability and permittivity of the surrounding medium are μ and ε, respectively, and $\left|\vec{r}-\vec{r'}\right|$ is the distance between an arbitrary observation point r and a source point r' on domain S. Both r and r' are defined with respect to the origin 0. The unknowns in (1) are $\boldsymbol{J}\left(\vec{r'}\right)$ and $\sigma(\vec{r'})$.

The surface charge density σ is related to the surface divergence of J through the equation of continuity [9, 11],

$$\nabla_S . J = -j\omega\sigma \tag{5}$$

The E field can therefore be calculated as:

$$\boldsymbol{E}^s(r) = -j\omega\mu \int_S G(r, r') \left[\boldsymbol{J}(r') + \frac{1}{k^2} \nabla' \nabla' . \boldsymbol{J}(r') \right] dr' \tag{6}$$

A similar equation can be derived using the H field instead of the E field [7, 11]. Contrary to the equations derived in [7], all three current components are considered in (6). To use (6) in a simulation, the surface integral can be approximated with a summation of currents over a discretized domain multiplied with proper basis functions as [7, 9, 10, 11]:

$$\boldsymbol{J}\left(\vec{r'}\right) = \sum_{n=1}^{M} \boldsymbol{J}_{\mathrm{n}} \vec{f}_{\mathrm{n}}(\vec{r'}) \qquad n = 1, \ldots, M. \tag{7}$$

where Jn are unknown coefficients, f_n are Rao-Wilton-Glisson (RWG) basis functions, and M is the total number of basis functions. Each basis function is associated with an interior edge, i.e., non-boundary edge (Figure 1), of the patch model and vanishes everywhere on S except in the two triangles attached to that edge.

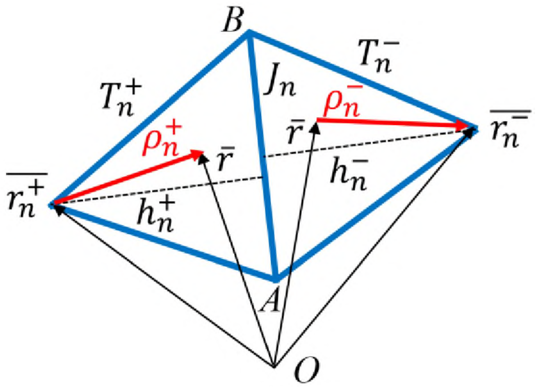

Figure 1. A triangle pair and the geometrical parameters associated with the interior edge.

Figure 1 shows two such triangles, T_n^+ and T_n^-, corresponding to the nth edge of a triangulated surface modeling a scatterer. The nth basis function (that is associated with the nth edge) is defined as:

$$\vec{f}_n(\vec{r}) = \begin{cases} \frac{\vec{\rho}_n^+}{h_n^+}, & \vec{r} \in T_n^+ \\ \frac{-\vec{\rho}_n^-}{h_n^-}, & \vec{r} \in T_n^- \\ 0, & elsewhere \end{cases} \tag{8}$$

where the local coordinates are defined as: $\vec{\rho}_n^+ = \vec{r} - \vec{r}_n^+$ and $\vec{\rho}_n^- = \vec{r}_n^- - \vec{r}$. For the nth interior edge, this representation uniquely defines two adjacent triangular cells T_n^+ and T_n^-. Their corresponding heights are h_n^+ and h_n^-, respectively. Using RWG basis functions (8) and discretized current (7), the electric field (6) can be written as:

$$[E]_{n\times 1} = [T]_{n\times m} \times [J]_{m\times 1} \tag{9}$$

where n is the number of observation points, and m is the number of current densities along inner edges on the conductor surface of the MoM domain. To calculate the surface current from a known field, a transfer function matrix is calculated. To calculate each integral in (6), consider an RWG element m with two inner triangles $T_m^\pm$ adjacent to the edge of length l_m (Figure 1), and the current on the m^{th} edge over the surface of this element, giving:

$$[T]_{n\times m} = -j\omega\mu \sum_{i=1}^{n} \sum_{i=1}^{m} G(r,r') \left[\vec{f}_i(\vec{r'}) + \frac{1}{k^2} \nabla' \nabla' . \vec{f}_i(\vec{r'})\right] \tag{10}$$

In case of having incident electric field E, current on each edge can be easily calculated with the least square method from (9). The surface current on each edge can be calculated as:

$$[J]_{m\times 1} = [T'T]_{m\times m}^{-1} \times T'_{n\times m} \times [E]_{n\times 1} \tag{11}$$

Here, the least square method is used because the number of unknowns is not always the same as the number of measured field points, n, in (9) [7, 12, 13]. The accuracy of the elements of transfer matrix $[T]$ depends on the accuracy of the integration done in (6). This integration has to be done on a source consisting of triangular patches. The integral in (6) can be solved using the weighted Gaussian quadrature method [7] or the sub triangle method (Figure 2), in which the position of sample points, ai, inside the triangles can be obtained from the vertices of triangle (r1, r2, r3). In this study, the integrals were solved with a summation over nine sub triangles (Figure 2a).

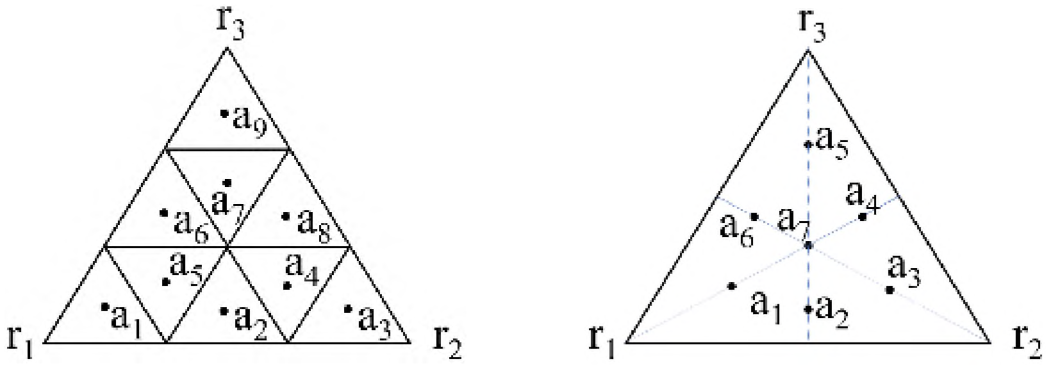

(a) (b)

Figure 2. (a) Nine sub triangles with the corresponding centers as sample points, (b) 7-points Gaussian quadrature elements.

As $T'T$ in (10) is ill-conditioned, (11) must be performed with regularization to find a meaningful approximate solution in the presence of noise [12]. A common approach uses Tikhonov zero-order regularization, which minimizes the total energy in reconstructed current sources as [12, 13]:

$$J^{reg}_{m\times1}(\lambda) = [T'_{nm\times1}T_{nm\times1} + \lambda^2 I]^{-1}T'_{nm\times1}[E]_{n\times1} \tag{12}$$

where I is the identity matrix and λ is a regularization coefficient tuned to maximize the accuracy of the result and minimize the impact of noise or errors. Here we used the discrepancy principle to determine the value of λ, where the value is selected to balance the accuracy of the solution for the sources in the linear system of equations Ax = y, to within the accuracy of the measurements of y [13]. The relative error between the measured and reconstructed electric fields at the measured locations is defined as [12]:

$$RE = \frac{\|E_n - T_{nm} J_m^{reg}\|}{\|E_n\|} \tag{13}$$

where ||·|| is the Euclidean norm. When λ =0, the relative error is minimized, but the solution may be non-optimal. From [12], a suitable value of λ is found when:

$$RE_{Prediction\,(\lambda)} = RE_{Data} \tag{14}$$

where $RE_{Prediction\,(\lambda)}$ is the relative error in the predicted data as shown in (13) and RE_{Data} is the expected error in the measured data, as defined based on experience [12]. The process for determining a 2D planar patch of sources is shown in Figure 3, for the case where the patch is located on a planar surface at height Z = 0.

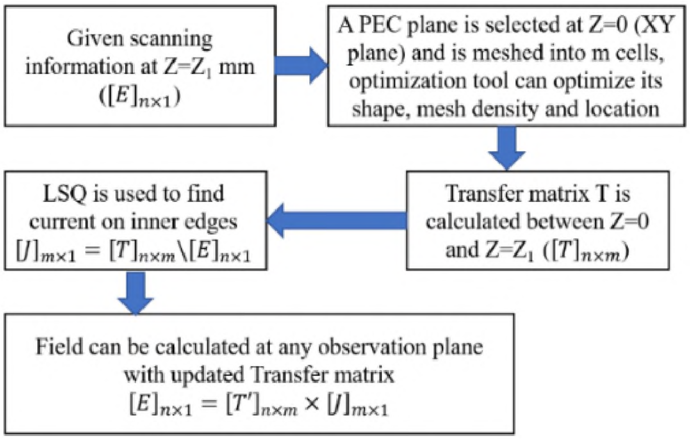

Figure 3. Determination of source currents, J.

Given the scanning information, a perfect electric conductor (PEC) plane is placed on the XY plane at Z = 0 mm and discretized into triangles e.g., 200 cells. This plane will be called the source plane. The transfer function matrix [T] is calculated with RWG basis functions between any observation plane, e.g., Z = 1 mm, or Z = 5 mm, and the source plane. The currents forming the sources are found using (12). These sources can then be used to find the fields at any location, not just the measurement locations.

3. VERIFICATION THROUGH SIMULATION

Strong noise coupling from neighboring components to system antennas may degrade the RF performance of the system. The sources inferred from (12) may be used to predict fields to the side of a component (i.e., in the x or y direction), as well as above (i.e., in the z direction). In [14] current sources were inferred from electric field information (Ex, Ey and Ez) in an observation plane and were used to predict fields above the observation plane in a 3D full wave simulation.

It was also shown that the proposed method can accurately predicted fields to the side of a ring or bowtie antenna (the emitters) when using noisy scanning data above the antenna to predict the sources. Noise was added to the simulated data to make the signal to noise ratio (SNR) 10 dB in the examples. For these antennas, the emitting currents run only in the x and y directions since the antenna has a 2D geometry.

The inverse solution was therefore able to accurately represent current flowing within the antenna, and the error in the estimated fields in all directions was less than 2 dB for the cases studied [14].

Most unintentional radiators, however, cannot be entirely represented as planar. An IC, for example, is a common source of interference and will have currents flowing in the z-direction as well as in the x and y directions. The interference from these more complex structures must also be considered. The IC and trace shown in Figure 4 was used to study these more complex scenarios. The IC and trace together may generate interference. The dimensions of the ground plane was 60 mm × 60 mm (2 λ×2 λ at 10 GHz). The trace was excited on one side at 10 GHz with a 1-V, 50 Ω port and was terminated on the other side with a 50 Ω load. The IC is a commercial microcontroller in a quad flat package (QFP). An electromagnetic model for the IC package was developed as part of the work described in [15]. The IC was mounted 0.4 mm above the PEC ground plane and was excited at two different 1-V, 50 Ω ports at 10 GHz. The fields generated by each stimulation source were found separately and then added to determine the emissions from the noise source DUT. Electric Fields with phase were simulated from these sources in CST Studio Suites [16] and used to validate methods for predicting interference using the source reconstruction technique.

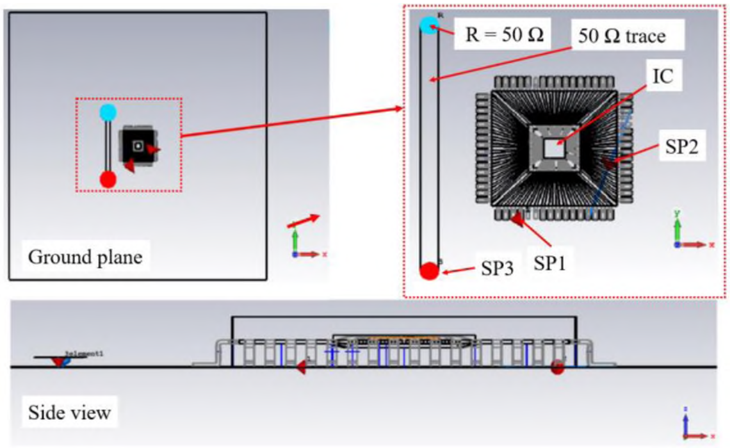

Figure 4. Fields generated by an IC and a trace represented with sources.

Initially, sources were found only on a 40 mm × 40 mm planar meshed PEC patch as shown in Figure 5.a. The patch was located in the XY plane at Z = 0 mm and discretized into 376 mesh cells with 540 adjacent edges. The transfer function matrix [T] was calculated with RWG basis functions assuming the data was captured in a 60 mm x 60 mm observation plane at Z = 2 mm, with step size 1 mm (i.e., there were 3600 measurements of Ex, Ey and Ez within the plane).

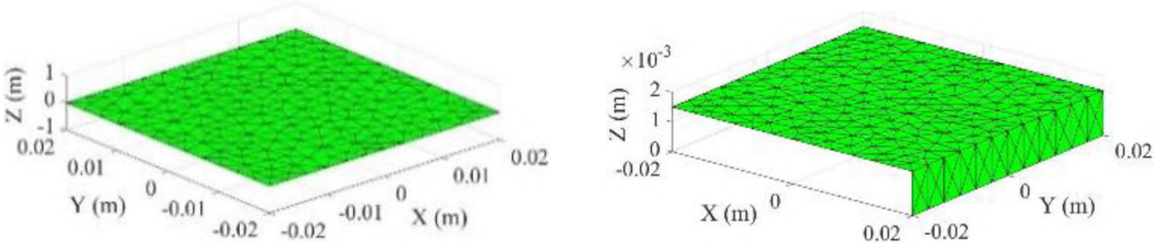

(a) (b)

Figure 5. The current sources were represented with a) a plane just above the IC and trace in initial estimates, and b) two perpendicular planes in later studies.

White noise was added to the measurements to give them an SNR of 10 dB. The noisy scanning data was used with (12) to estimate the sources. These sources were then used to predict the fields above the measurement plane, at Z = 6 mm.

Fields were also estimated on a YZ plane at X = 25 mm. The trace and IC (which will be referred to as the device under test, or DUT) occupy an area from X = -20 mm up to X = 20 mm. Placing the reconstruction plane at X = 25 mm puts it slightly outside the boundary for the Huygens' box surrounding the DUT.

The reason for this selection will be further discussed in the next section. The simulated and predicted results are shown in Figure 6a and Figure 6b. The predicted fields above the measurement plane, at Z = 6 mm, had less than a 2 dB relative error [14], but the average error in the fields to the side of the sources, in the YZ plane at X = 25 mm, was as high as 6 dB (Figure 6b). The reason the errors were higher in this test than found for planar antennas in [14] is the current flowing in the Z direction on the 3D structures.

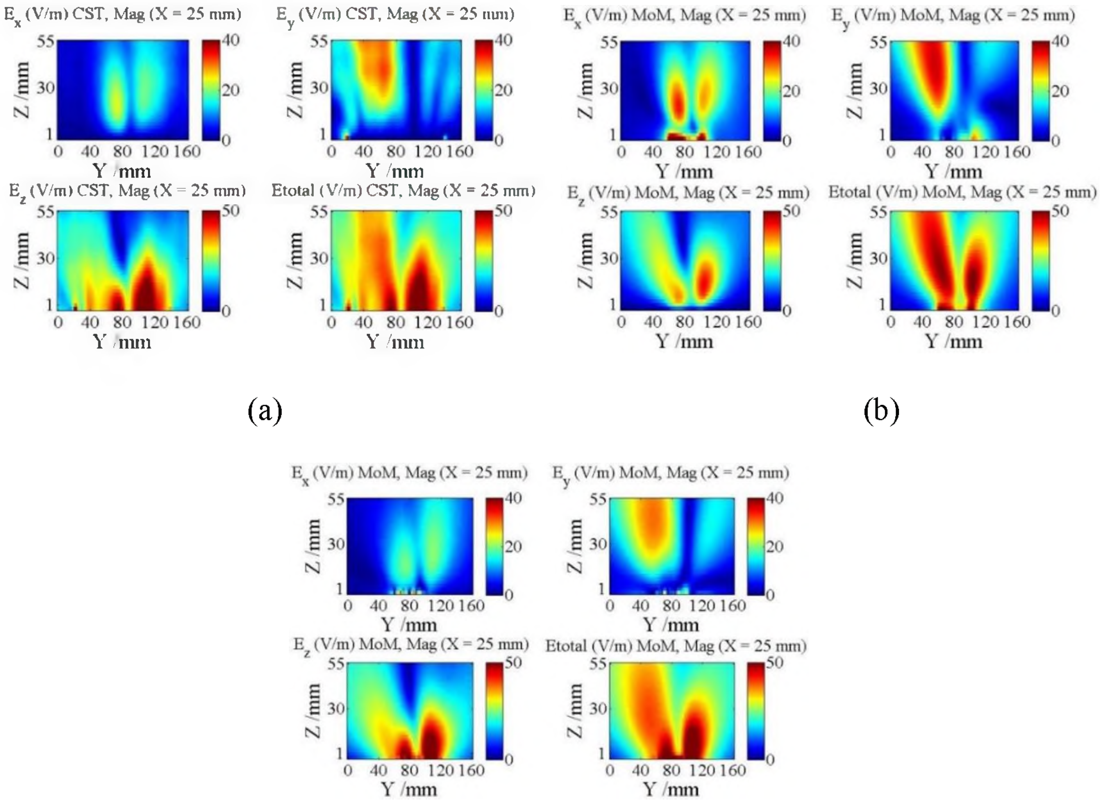

(a) (b)

(c)

Figure 6. Simulated and predicted E-fields from the IC and trace (Figure 4) at X = 25 mm with step size of 1 mm: a) Noiseless scanning data; b) Reconstructed E-field from noisy data using 2D planar surface to represent sources (average error ≈ 6 dB); c) Reconstructed E-field from noisy data using two source planes (average error ≈ 2 dB).

3.1. ESTIMATION OF SOURCES ON SURFACE SURROUNDING EMITTER

Errors in fields to the side of the emitter can be reduced by estimating equivalent sources on a surface surrounding the sources of interest, similar to a Huygens box [17].

Strictly speaking, the surface should surround the source. When only predicting fields to one side of the source, however, an open surface like a half-sphere, open box, or two simple planes (Figure 5b) can be sufficient. The most important idea is that equivalent sources should be located between the real source and observation points (Figure 7).

3.2. IMAGE THEORY

For the problem at hand, the fields are predicted over a conducting surface (i.e., the return plane) rather than in free space. The impact of the ground plane can be accounted for by using image theory [18], such that fields are calculated from both the source and its image as though they are in free-space and are summed together to estimate the fields above the ground plane. Although the ground plane is not infinitely large, one may be able to assume that both the emitter and the susceptible antenna sit above this plane so that image theory will apply. For cases where the victim does not sit above the return plane, however, image theory cannot be used, and sources muse be represented on the return plane itself.

Including the image, the sources in Figure 7 may be represented as shown in Figure 8. Transfer coefficients are be calculated from both the source (T1) and its image (T2), and the electric field can be represented as:

$$[E]_{\mathrm{n}\times 1} = [T_1 \;\; T_2]_{\mathrm{n}\times 2\mathrm{m}} \times \begin{bmatrix} J_1 \\ J_2 \end{bmatrix}_{2\mathrm{m}\times 1} \tag{15}$$

where J_1 and J_2 are appropriately symmetric if the ground plane is infinite.

3.3. ACCURACY OF ESTIMATED FIELDS

Estimated fields above the measurement plane and to the side of the IC and trace, in the YZ plane at X = 25 mm, are shown in Figure 6c, when the SNR of the field measurements was 10 dB and when using two perpendicular planes to represent the sources. As when finding current sources only in a plane above the IC and trace, the predicted fields above the measurement plane, at Z = 6 mm, had less than a 2 dB relative error. When predicting the fields to the side of the sources, in the YZ plane at X = 25 mm, however, the average relative error in the fields reduced dramatically from 6 dB to 2 dB.

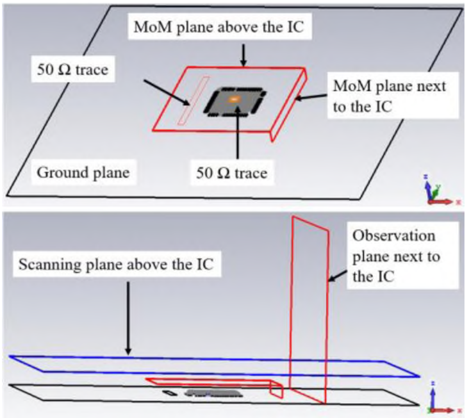

Figure 7. The current sources were represented on a surface roughly surrounding the IC and trace.

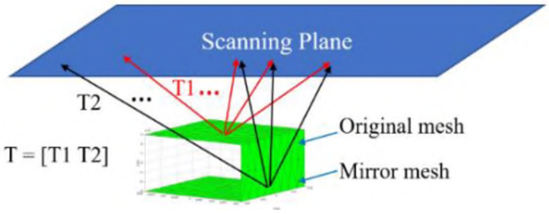

Figure 8. MoM surfaces and their images.

To further analyze error, Figure 9 shows the RMS error using (13) for locations in the X=25 mm YZ plane as a function of their height, Z. As expected, the error is highest for fields closest to the return plane, and smallest for fields located closer to the observation plane. This result is expected in part because less information is available for the components far from the observation plane. The relative error is 3-4 dB smaller using two source planes than using only a single plane.

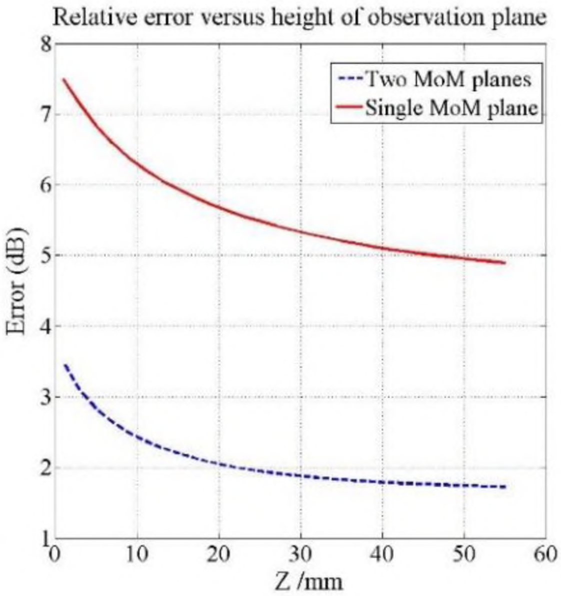

Figure 9. Relative error versus height for fields predicted in the YZ plane at X = 25 mm using a single source plane and using two perpendicular planes.

The accuracy of the estimated fields also depends on the size and location of the scan plane, and the distance between the equivalent sources and the prediction plane. Figure 10 shows a schematic representation of the IC, the source planes, the scan plane, and the prediction plane. Simulations were performed to demonstrate the impact of the size of the scan plane, X1, the relative height of the scan plane, H1, and the relative distance between the sources and the prediction plane, X2. Simulations were done with a full wave solver with scan plane sizes of 60 mm × 60 mm, 80 mm × 80 mm, 120 mm × 120 mm, and 160 mm × 160 mm, and at heights of 2, 2.5, 3, 4, 6, 8, and 10 mm. Fields were predicted using the source representation on observation planes at X2 = 1, 3, 5, 7, 9, 11, 13, 15, 17, 19, 21, 23, 25, 27, 29, 31, 35, 40, 45, 50, 55, 60, and 70 mm, and were compared to results found directly through simulation.

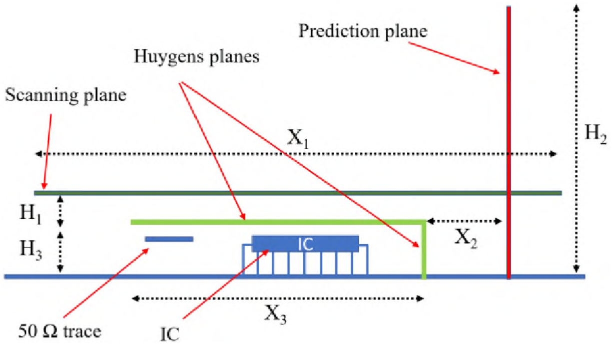

Figure 10. Schematic of scanning, prediction, and source planes.

Increasing the size of the scan plane from 60 mm × 60 mm to 80 mm × 80 mm decreased the average error by about 0.5 dB at X = 25 mm and 1 dB at X = 70 mm. As expected, a larger scan plane provides more information for current reconstruction. However, the improvement is less important for an observation plane at X = 25 mm since the scanning plane is already much larger than the source (at least three times bigger).

The error in the predicted fields is expected to depend both on the distance to the sources and on the height of the scan plane. To capture how these parameters impact the accuracy of the predicted fields, relative error is plotted in Figure 11 as a function of distance from the sources, (X2). Not surprisingly, the error is smaller for a lower scanning height (H1) when X2 < H1. In a real application, however, some problems will occur if the probe is too close to the DUT, as the definition of the "height" of the center of the probe becomes less clear. A 1 mm loop probe should not be used at 0.2 mm height, as we do not really know what the probe is measuring, and the probe's electrical center depends on the distance to the DUT. This issue is relevant if the probe and DUT are less than one probe size apart. If the region of interest is close to the DUT (X2 < H1 + H3), the scanning height should be as small as possible. When predicting fields far away from the DUT (X2 > H1 + H3), however, the height of the scanning plane is less important.

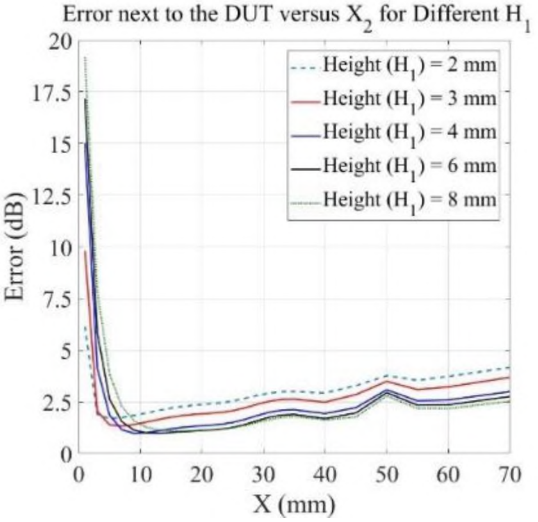

Figure 11. Average relative error (dB) versus the distance from source plane.

4. VALIDATION THROUGH MEASUREMENT

Simulated results were validated through measurements of the near electric fields over a test IC. The x-, y-, and z-components of the electric field were measured with a near-field scan system. To obtain accurate phase-resolved results, the probes were calibrated and compensated first [19] and then the IC was scanned second using a Vector Network Analyzer (VNA) together with a reference signal to obtain the phase at each measurement location. The IC, test board, and measurement plane are shown in Figure 12. A diagram of the measurement setup is shown in Figure 13, and a picture of the setup is shown in Figure 14.

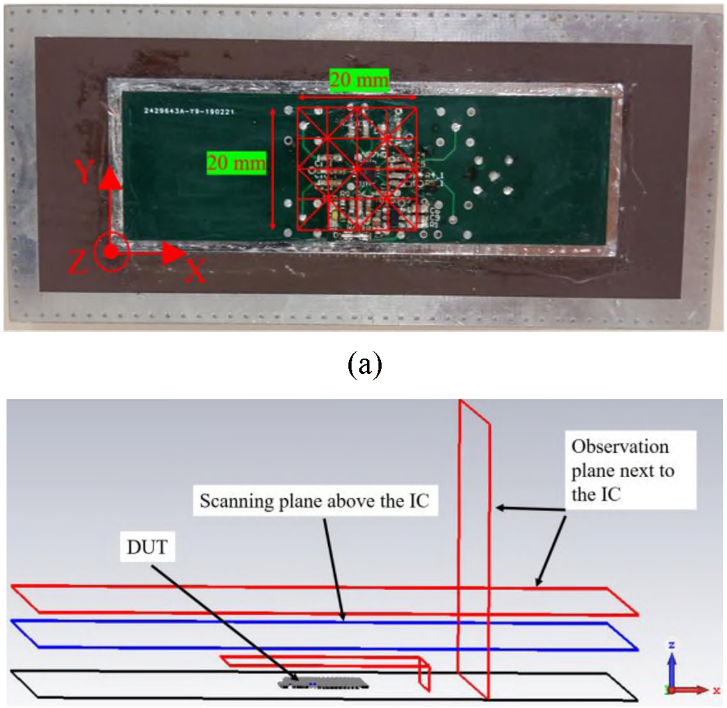

(a)

(b)

Figure 12. Near-field scans were performed over a buffer IC: a) test board with buffer IC overlaid with the source surface; b) measurement and observation planes relative to the noise source.

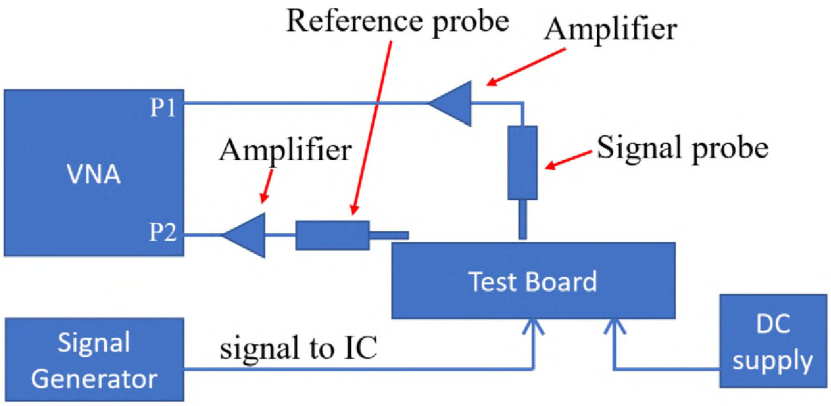

Figure 13. Block diagram of measurement setup.

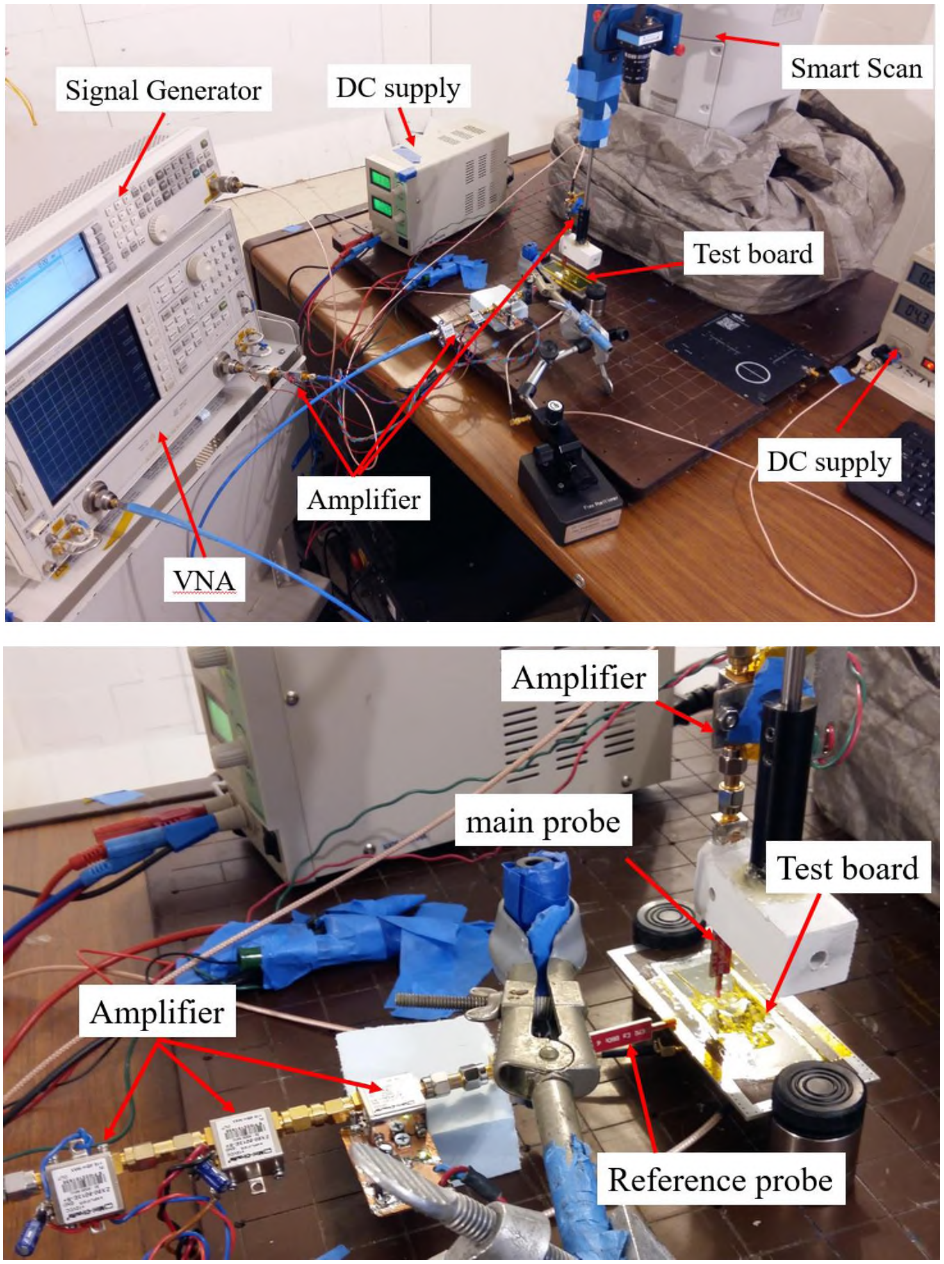

Figure 14. Measurement setup.

The test IC used here was a buffer IC [20] fed by a 5 dBm signal at 500 MHz. Near-field scans were performed at 1.5 GHz at the third harmonic of the buffer output. The scanning plane was 20 mm × 80 mm with a step size of 1 mm (1600 measurement points). The scanning height was 2 mm above the PCB.

The current sources were constructed on two planes as shown in Figure 12: a 25 mm × 20 mm plane above the IC and a 1.5 mm × 20 mm plane next to the IC. The YZ plane next to the IC is located at X = 45 mm, since the DUT noise sources were located between X = 25 mm to around X = 45 mm, as shown in Figure 12. The planes were discretized into 424 triangles (611 adjacent edges) for expansion using RWG basis functions.

The transfer function matrix [T] was calculated with RWG basis functions assuming the scan plan was located at Z = 2 mm, and the observation planes were located at Z = 5 mm, and at X = 48 mm.

The measured and predicted fields in the XY plane above the scan plane, at Z = 5 mm, are shown in Figure 15. The shape of the fields is reconstructed well. The average error is less than 3 dB between the measurements and the prediction.

Figure 16 shows the measured and predicted fields in the ZY-plane at X = 48 mm. Here, the shape of the electric fields is also constructed well, and the average relative error in the predicted fields is less than 3.5 dB (~50%).

5. DISCUSSION

The fields to the side of an emitter are often of interest in RF de-sense applications. Prediction of these fields can be challenging, however, since measurements can often only be performed above the emitter. In this paper the MoM method using electric field integral equation (EFIE) was used to represent the noise source and to predict fields to the side. While all high-frequency noise sources will emit both electric and magnetic fields, one of the two fields will often dominate in the near-field region. Because the output of a near-field probe will always be influenced by both fields, the output of a magnetic field probe in a strong electric field will tend to depend on the electric rather than the electric field, and vice versa. Practically speaking, it is generally better to characterize near electric field sources by measuring the electric field, and near magnetic field sources by measuring the magnetic field. The approach proposed here depends on measurements of the electric field, so is expected to perform best when characterizing near-electric field sources. Strong magnetic field sources might be better characterized using an approach that depends on the magnetic field like the one in [7].

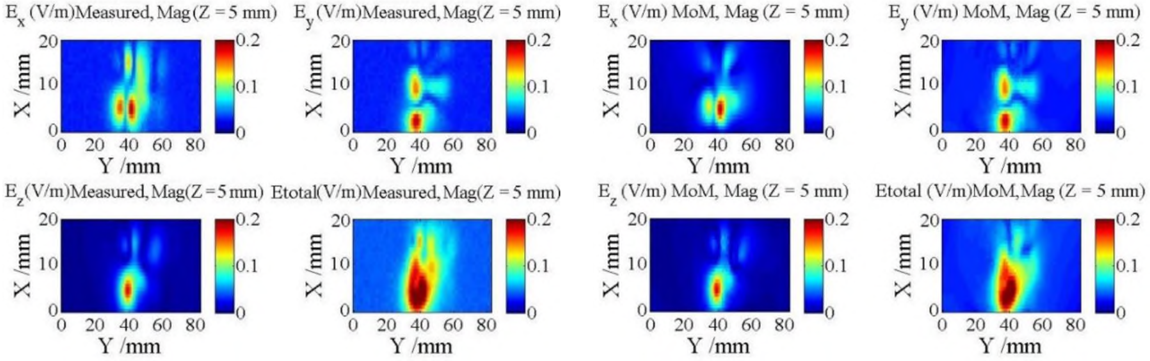

(a) (b)

Figure 15. Measured and estimated electric fields in the XY plane above the test IC at Z = 5 mm: a) Measured fields; b) Reconstructed fields.

To be useful in many systems, the location of the source plane should often be very close to, if not inside of, the DUT. To demonstrate proof-of-concept in this paper, the source plane lay just outside the IC. In an application within a dense system, however, there may be a metal can, heat sink, flex cable, or other object in the region just above or to the side of the IC. The source plane cannot intersect with these objects and still generate a valid result. Locating the source plane just within the IC prevents this possibility.

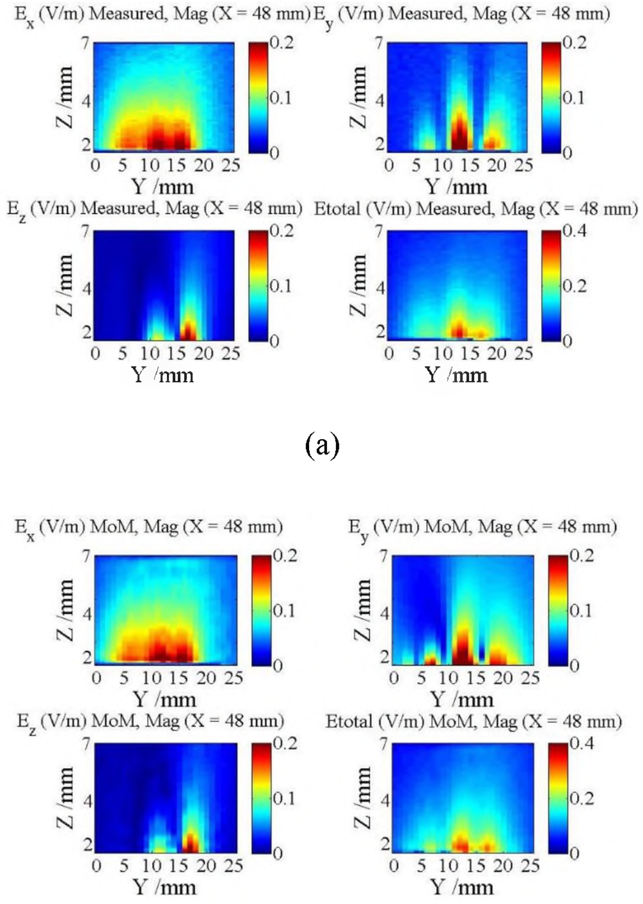

(a)

(b)

Figure 16. Measured and reconstructed electric fields next to test IC in the ZY plane at X = 48 mm: a) Measured fields; b) Reconstructed fields.

An error analysis was performed to understand the impact of scan plane parameters like the size of the scan plane, the size of the source representation, and the relative distance between the estimated fields and the source plane on prediction accuracy. For the present analysis, the performance of the approach was also characterized by adding zero-mean white noise to simulated data. Real measurements, however, include many other errors like bias, cross-field coupling, errors in phase and probe position, among others. The impact of these errors should be investigated in the future.

6. CONCLUSION

Methods were developed to estimate an equivalent representation of sources from near-field scans of the electric fields. This representation was evaluated based on its ability to estimate fields both above the scan plane and next to the DUT when the scans were noisy and only performed in a plane above the DUT. The proposed reconstruction method was validated with measurements of a test board containing a buffer IC. The representation was shown to accurately predict fields at locations both above and to the side of the DUT with less than a 3.5 dB average error for this test case. It was demonstrated that a larger scanning plane provides more information for source representation. Furthermore, it was shown that the error will decrease for a lower scanning height (H1). There are some practical limitations to reducing the height, however, like accurately determining the coupling to the probe or the probe's electrical center, which depends on the distance to the DUT. Further studies are needed to calculate the error considering these and other practical limitations on different types of sources which are E field or H field dominant.

REFERENCES

[1] P. Wilson, "On Correlating TEM Cell and OATS Emission Measurements," *IEEE Transaction on Electromagnetic Compatibility*, vol. 37, no. 1, pp. 1-16, Feb. 1995.

[2] Z. Yu, J. A. Mix, S. Sajuyigbe, K. P. Slattery and J. Fan, “An improved dipole-moment model based on near-field scanning for characterizing near-field coupling and far-field radiation from an IC,” *IEEE Transaction on Electromagnetic Compatibility*, vol. 55, no. 1, pp. 97-108, Feb. 2013.

[3] M. Sørensen, I. B. Bonev, O. Franek and G. F. Pedersen, "Assessment of the Huygens’ Box Method with Different Sources Near Obstacles," *IEEE Transactions on Electromagnetic Compatibility*, vol. 62, no. 2, pp. 433-442, April 2020.

[4] L. Li, J. Pan, C. Hwang, G. Cho, H. Park, Y. Zhang, J. Fan, “Near-field Coupling Estimation by Source Reconstruction and Huygens's Equivalence Principle”, *IEEE Symposium on Elec. Compatibility and Signal Integrity, pp. 324-329, March, 2015.*

[5] R. Rafiee Alavi, A. Kiaee, R. Mirzavand, P. Mousavi, “Locally Corrected Nyström Technique and Its Relationship with RWG Method of Moment for Current Reconstruction Using Very-Near-Field Measurements”, *11th European Conference on Antennas and Propagation (EUCAP)*, pp. 319-323, March 2017.

[6] Y. Álvarez, F. Las-Heras, M. Rodríguez Pino, “Reconstruction of Equivalent Currents Distribution Over Arbitrary Three-Dimensional Surfaces Based on Integral Equation Algorithms,” *IEEE Transaction on Antennas and Propagation*, vol. 55, no. 12, Dec. 2007.

[7] Q. Huang, L. Li, X. Yan, B. Bae, H. Park, C. Hwang, J. Fan, “MoM-Based Ground Current Reconstruction in RFI Application,” *IEEE Transaction on Electromagnetic compatibility*, vol. 60, no. 4, August 2018.

[8] Q. Huang, T. Enomoto, S. Seto, K. Araki, J. Fan, C. Hwang, “A Transfer Function Based Calculation Method for Radio Frequency Interference,” *IEEE Transaction on Electromagnetic compatibility*, vol. 61, no. 4, August 2019.

[9] S. M. Rao, D. R. Wilton, A. W. Glisson, “Electromagnetic Scattering Surface of Arbitrary Shape,” *IEEE Trans. on Antennas and Propag.*, vol. 30, no. 3, May 1982.

[10] J. S. Meiguni, M. Kamyab, and A. Hosseinbeig, “Theory and experiment of spherical aperture coupled antennas,” *IEEE Transaction Antennas Propagation,* vol. 61, pp. 2397–2403, 2013.

[11] Walton C. Gibson, “The method of Moment in Electromagnetics”, Chapman and Hall/CRC, Taylor, and Francis Group, 2014.

[12] Z. Yu, J. A. Mix, S. Sajuyigbe, K. P. Slattery, and J. Fan, “An Improved Dipole-Moment Model Based on Near-Field Scanning for Characterizing Near-Field Coupling and Far-Field Radiation From an IC”, *Transaction on Electromagnetic Compatibility*, Vol. 55, No. 1, pp. 97-108, Feb. 2013.

[13] R. Kress, Numerical Analysis. New York: Springer-Verlag, 1998.

[14] H. Rezaei, J. Meiguni, M. Soerensen, J. Fan, D. Pommerenke, “Source Reconstruction in Near Field Scanning using Inverse MoM for RFI Application”, *IEEE International Symposium on Electromagnetic Compatibility, Signal & Power Integrity (EMC+ SIPI)*, pp. 584-589, July, 2019.

[15] L. Zhang, D. J. Pommerenke, and J. Fan, “Determining Equivalent Dipoles Using a Hybrid Source-Reconstruction Method for Characterizing Emissions from Integrated Circuits”, *IEEE Transaction on Electromagnetic Compatibility*, vol. 59, no. 2, April 2017.

[16] “CST microwave studio,” [Online]. Available: https://www.cst.com

[17] M. Sorensen, O. Franek, G. Frolund Pedersen, A. Radchenko, K. Kam, and D. Pommerenke, “Estimate on the uncertainty of predicting radiated emission from near-field scan caused by insufficient or inaccurate near-field data”, *International Symposium on Electromagnetic Compatibility - EMC EUROPE*, Sep. 2012.

[18] J. Ming Jin, “Theory and Computation of Electromagnetic Fields,” in Magnetism, *Second Edition. Wiley*, 2015, pp. 94–101.

[19] J. Zhang, K. Keong, M. Jin, V. Khilkevich, D. Pommerenke, and J. Fan, “An effective method of probe calibration in phase-resolved near-field scanning for EMI application,” *IEEE Transaction on Instrumentation and Measurement*, vol. 62, no. 3, pp. 648–658, Mar. 2013.

[20] A high-performance differential 1:4 CML fanout buffer with a selectable Equalizer receiver [online]. Available: “https://www.onsemi.com/pub/Collateral/NB7HQ14M-D.PDF”

III. A METHODOLOGY FOR PREDICTING NEAR-OPTIMAL DIPOLE SOURCES IN A SOURCE RECONSTRUCTION IMPLEMENTATION

Hossein Rezaei

Department of Electrical Engineering
Missouri University of Science and Technology
Rolla, Missouri 65409–0050
Tel: 573–308–9313
Email: hrr7d@mst.edu

ABSTRACT

Predicting near electric-and magnetic-field emissions can solve many interference problems before they occur. The three main field reconstruction methods are based on a Method of Moments representation, dipole representation, and on the Huygens' Box principle. In this work, a methodology is proposed for estimating a near-optimal dipole source-representation in a noisy environment.

The dipole representation is found from electric or magnetic near-field scan data and with some help from the user. A near field scan is done on a plane above the noise source and is used to predict fields above and to the side of the noise source.

In order to accurately predict fields to the side of the device under test (DUT), dipole combinations must be located properly within the noise source area, typically close to the physical height of the DUT.

The impact of three major sources of error in near field scans: random measurement noise, cross field coupling, and position error, was investigated on field prediction. A clear

decision-making process with examples is provided to guide the user toward selection of the "best" representation.

1. INTRODUCTION

Prediction of the near electric and magnetic fields generated by devices can be used to mitigate potential radiofrequency interference (RFI) problems early in the design process. Near-field scanning is commonly used to characterize RFI noise sources. An equivalent source representation can be found using the Method of Moments [1-2], the Huygens' Box principle [3-4], or equivalent dipoles [5-6]. These representations can be found using near-field scan data with or without phase information [6-7]. Once found, the sources can be used to predict the near- and far-field emissions generated by the device. The Method of Moments represents near electric fields [1, 2] based on the theorem of equivalent surface currents.

The electric current which flow on a surface can be used to predict the fields generated by the source. Conversely, if the measured fields are known, one can estimate source currents by solving an inverse problem. Current distributions can be found from known electric (EFIE) or magnetic fields (MFIE), or a combination of the two (CFIE).

A near-field scan on a volume surrounding the noise source can be used to predict the maximal radiated emission from the source using the Huygens' box principle [3-4]. The significance of the step size of the near field scan, its phase accuracy, and the importance of scanning over a full Huygens' box were investigated by simulation in [4]. This study also investigated the effect of scanning area and scanning height and showed that equivalent sources on all six surfaces are needed. A study of the limitation of the Huygens' box method was performed in [3] for a few EMC test cases.

An equivalent dipole model represents the source with a number of dipoles placed throughout the source domain [6, 8]. The value (both magnitude and phase) of dipoles at fixed locations can be found using the least-squares method with regularization from the near-field scanning data [6].

Although, different methods have been developed to solve a source reconstruction problem and provide a possible solution for the EMI source reconstruction through the near-field scanning, there should be a technique for making decision about when you have a good result since minimizing the least square error does not necessarily lead to a good representation in the presence of perturbation noise or other measurement or modeling errors [9]. The user needs to determine if a solution, which is a combination of source type, location, number of sources, etc. and mathematical process for determining the moments is good or not good.

Table 1 summarizes some of the studies which are self-critical and try to guide the user finding a solution. As shown, the only practical limitation which has been considered in the literature, is the presence of white gaussian noise with different signal to noise ratio (SNR). White gaussian noise is very bad method for EMC application because noise floor is what exists in a near field scanning and white noise will be canceled out if the number of scanning point is very high.

Additionally, there are not any exact theoretical criteria to choose the source for an inverse problem without applying predefined information of the source. The predefined sources are used based on some experimental rules and the results are provided for just a couple of test cases in each study at a few frequency points [6-23] (Table 1).

To be best of our knowledge, there is no clear approach in literature to help the user find the best equivalent source e.g., dipole combination, to represent the source for a source structure with multiple origins of the noise.

Therefore, a study is needed which considers the capability of the field reconstruction approach for near and far field applications over a wide frequency range for electrically large and small DUTs in the presence of typical measurement errors e.g., random measurement noise in the scan data, errors in scan height, cross coupling between electric and magnetic field measurements.

It is also important to analyze the impact on field reconstruction to the side of the device (where most RFI problems occur) when using sparse scan data from above the DUT made.

In this paper, a semi-automated source reconstruction method is proposed for finding a near-optimal dipole representation from phase-resolved electric or magnetic field measurements. The study considers field prediction both above and to the side of the DUT with far fields and the total radiated power (TRP).

The ability of the method to reconstruct fields both above and to the side of the emitter was tested through simulation of several test cases which had either electric or magnetic field dominant sources, or a combination of the two. 2D feature selective validation (2D FSV) [24] was used to evaluate the performance of the method. Measurements over a test board were performed to validate the proposed method.

Table 1. Summary of different field reconstruction methods.

Ref.	Method (DUT)	Freq. (GHz)	Any measurement error studied?	Any predefined source?
[6]	Dipole moment[1] (buffer IC)	0.87 & 5	No	Yes.
[7]	Equivalent current1 (Trace and DC-DC buck convertor)	1	Different SNR	Yes.
[8]	Dipole moment1 (IGBT and a power diode)	< 0.1	No	GA found dipole moment, position, and orientation.
[9]	Huygens' box & dipole (patch antenna & IC)	<6	No	Yes.
[10]	Dipole method[2,3] (Clock buffer IC)	≈ 1.6	No	No, GA found number of dipoles and their location.
[11]	current distribution[1] (DC-DC convertor)	< 0.1	No	Yes.
[12]	Current distribution (The CK505 die)	1	5% of white noise	Yes.
[13]	Current distribution (Transmission Lines)	20	Different SNR	Yes.
[14]	Dipole moment (a trace, & the PLL IC)	0.45	No	No, guidelines to find height, source spacing, and scanning spacing.
[15]	Huygens' box and equivalent dipoles (Patch antenna & trace)	2-3	No	Yes.
[16]	MoM, Current source (trace & CBS antenna)	5.8 and 20	White noise SNR=30dB	Yes.
[17]	Dipole method[2] (two patch antennas)	2.5	No	Yes
[18]	Equivalent dipole (a patch antenna with four metallic surroundings)	2.2	No	Yes.
[19-22]	Equivalent Dipole[4] (Magnetic dipoles)	2.2	No	No, Dipole moment, location and number are obtained.
[23]	Equivalent Dipole[5] (Magnetic/Electric dipoles)	2-3	No	No, Dipole moment, location and number are obtained.

1) Iterative approach, 2) LSQ, 3) GA, 4) ANN method with iteration, 5) Machine learning method.

2. DIPOLE BASED SOURCE RECONSTRUCTION METHOD

A dipole representation of near-field sources can be found starting with the vector potential formulation [5]:

$$\bar{A}(\bar{r}) = \frac{\mu_0}{4\pi}\int_v \bar{J}(\overline{r'})\frac{e^{-jk_0|\bar{r}-\overline{r'}|}}{|\bar{r}-\overline{r'}|}dv', \tag{1}$$

where A is the magnetic vector potential, J is the source current, $k = \omega\sqrt{\varepsilon\mu} = 2\pi/\lambda$ is the wavenumber, and λ is the wavelength. The permeability and permittivity of the surrounding medium are μ and ε, respectively, and $|\vec{r} - \overrightarrow{r'}|$ is the distance between an arbitrary observation point r and a source point r' on domain v. Both r and r' are defined with respect to the origin 0. The Green's function in a homogeneous medium is defined as:

$$G_0(\vec{r},\overrightarrow{r'}) = \frac{e^{-jk|\vec{r}-\overrightarrow{r'}|}}{4\pi|\vec{r}-\overrightarrow{r'}|} \tag{2}$$

The electric and magnetic fields can be calculated from A [5]:

$$\mu_0\bar{H}(\bar{r}) = \nabla \times \bar{A}(\bar{r}) \tag{3}$$

$$j\omega\varepsilon_0\bar{E}(\bar{r}) = \nabla \times \bar{H}(\bar{r}) \tag{4}$$

The sources are considered to be infinitesimal electric and magnetic dipoles. The electric dipole moment is defined as $\bar{P}$, and the magnetic dipole moment as $\bar{M}$ [5]. The electromagnetic fields which radiate from electric and magnetic dipoles are given by [5]:

$$\begin{bmatrix} E_x \\ E_y \\ H_x \\ H_y \end{bmatrix} = [T] \times \begin{bmatrix} P_x \\ P_y \\ P_z \\ M_x \\ M_y \\ M_z \end{bmatrix} \tag{5}$$

where Ex or Hx and Ey or Hy are the x and y components of the electric and magnetic fields, respectively. The contribution of each dipole to corresponding field component is represented as T matrix, e.g., THx,Px represents the Hx field component which is generated with Px dipole. The unknown electric and magnetic dipoles can be found from known field measurements as [5]:

$$\begin{bmatrix} P_x \\ P_y \\ P_z \\ M_x \\ M_y \\ M_z \end{bmatrix} = [T'T]^{-1} \times T' \times \begin{bmatrix} E_x \\ E_y \\ H_x \\ H_y \end{bmatrix} \tag{6}$$

where T is the field generation matrix given in (5).

A typical source representation would place the electric and magnetic dipoles on an XY plane just above the device whose emissions they are intended to represent. This plane will be called the source plane. The transfer function matrix [T] can be calculated between the source plane and any observation point outside a volume containing the dipoles and the device, for example on planes above and to the side of DUT. There are two common approaches to quantifying the error in the predicted fields: using the root-mean-square (RMS) error in the predicted fields at known measurement points [1, 7, 10] and using feature selective validation (FSV) over a scan plane [24]. FSV was chosen by an IEEE standard committee as a reference method [24] and is widely used in the EMC community. FSV determines a figure of merit which is roughly equivalent to a visual comparison of the measured and predicted data by a human observer. The output of FSV is found from a point-by-point comparison and is represented in the form of the Amplitude Difference Measure (ADM) or Feature Difference Measure (FDM) which represents the feature differences between data sets. The combination of the ADM and FDM is reflected in the Global Difference Measure (GDM). The comparison is considered to be Excellent for GDM ≤ 0.1, Very Good for $0.1 \leq$ GDM < 0.2, Good for $0.2 \leq$ GDM < 0.4, Fair for $0.4 \leq$ GDM < 0.8, Poor for $0.8 \leq$ GDM < 1.6, and Very Poor for $1.6 \leq$ GDM [24], which makes the comparison much easier for the user.

3. DETERMINING THE NEAR-OPTIMAL CONFIGURATION

With the presence of uncompensated errors in the measurement, the accuracy of the predicted fields will decrease. There are three main sources of error in near field scanning: cross field coupling, position error, and random noise in the measured field levels. The impact of each noise type will be studied through simulations.

Cross field coupling is caused when the near field measurement probes are sensitive to more than one field component. In a real measurement, H-field probes also detect the E-field, and E-field probes detect the H-field, causing errors in the measured field components [25]. The cross-coupling becomes worse at higher frequencies, especially above 1 GHz. To consider cross coupling effects in simulation, up to 30 % of the unwanted field (≈ -10.5 dB suppression) has been added to the intended field measurements.

Position error is caused by the systematic error in the probe position throughout the scan [26, 27]. The position error can distort the phase distribution [27], as well as the magnitude of the measured fields. About a 1.5 mm position error has been considered when creating "measured" field data to mimic the size of this error in a practical measurement.

Additive random noise in the measured field levels is caused primarily by quantization errors in the measurement instrument or by thermal noise within the system. This error is represented here by setting the affective noise floor of the measurement such that the maximum signal to noise ratio across the measurement is SNR ≈ 15 dB. These noise sources will be used later in this work to demonstrate methodology for finding a near-optimal dipole representation of an RFI source. The reconstruction method will be repeated multiple times with different values of random noises to investigate the robustness of the reconstruction method. To find a near-optimal dipole representation, we propose to find a dipole combination with relatively low values of GDM, of the standard deviation of the GDM, and of the standard deviation of the total radiated power (TRP), over multiple applications of the approach with different instantiations random level noise. While other parameters like the value of fields to the side of the DUT, or the value of fields on other planes were in the far field or TRP could substantially improve results, it is assumed the user does not have any information other than scanning data above the source plane. Using these measures, we propose the following process for determining the near-optimal configuration of the equivalent dipoles:

1. Given scanning information above the DUT e.g., E(x, y, z) and H(x, y, z).
2. Add random noise, cross field coupling noise, and position error to the system.

$$E_p(x,y,z) = E(x+\Delta\mathrm{x}, y+\Delta\mathrm{y}, z+\Delta\mathrm{z}) + n(x,y,z) + \alpha_i H(x,y,z), \qquad (7)$$

   where n(x, y, z) is random noise and α_i is cross coupling coefficient.

3. consider N different dipole combinations as source representations. Each dipole combination has a different number of dipoles in the x- and y- directions as well as

different spacing between them. There are six dipole types on each location of source e.g., Px(x,y,z), Py(x,y,z), Pz(x,y,z), Mx(x,y,z), My(x,y,z), and Mz(x,y,z).

4. Use least-squares to determine the value of sources for each dipole combination using (6).
5. Repeat steps 2, 3, and 4 for M combinations of additive random noise.
6. Result will be a matrix of N × M solutions at each frequency.
7. The best solution is the one which has the lowest value of δ on the measurement plane:

$$\delta = \sum GDMi + STD(GDMi) + STD(TRPi) \qquad (8)$$

4. VERIFICATION THROUGH SIMULATION

As shown in Table 1, there is no clear approach in literature which finds the best equivalent source e.g., dipole combination, to represent the source for different types of DUT over wide frequency range using minimum number of scanning points. To address these concerns, two different DUTs were used for verification, e.g., an EMI filter with different scanning points and an IC with nearby traces over a wide frequency range.

4.1. EMI FILTER

Some unintentional radiators primarily create near magnetic fields, and some primarily create electric fields. An EMI filter, for example, is a common source of interference with a strong near magnetic field due to a big inductor creating interference particularly at lower frequencies. The EMI filter shown in Figure 1 was used to study such a source, focusing on emissions at 100 MHz. The big inductor and two capacitors occupy an area of 20 mm × 25 mm. The big inductor generates a strong magnetic field, which may interfere with a nearby victim. The dimension of the inductor was 10 mm × 20 mm (0.003 $\lambda \times 0.006\ \lambda$ at 100 MHz). The dimension of the ground plane was 120 mm × 120 mm (0.04 $\lambda \times 0.04\ \lambda$ at 100 MHz). The input ports were excited with 100 MHz sinusoidal signals with magnitudes of 1 V and -1.1 V (to have a 180° phase change).

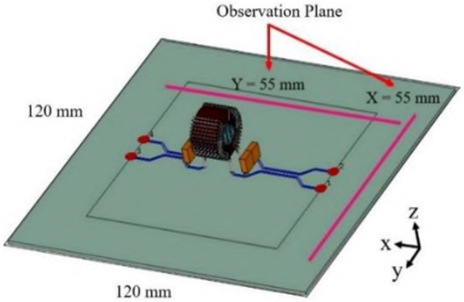

Figure 1. EMI filter with ground plane (120 mm × 120 mm).

These inputs create both a differential and common mode excitation, to create a more realistic source. An electromagnetic model for the EMI filter was developed as part of the work described in [28]. Electric and magnetic fields were simulated from this source in CST Studio Suites [29] and used to validate methods for predicting interference using the source reconstruction technique. Initially, the data was captured in a 120 mm × 120 mm observation plane at Z = 50 mm above the ground plane, with step size 2 mm (i.e., there were 3721 measurements of Ex, Ey, Hx and Hy within the plane). The cross-field coupling (about 30%) and then random noise was added to the noiseless field so that the maximum SNR ≈ 15 dB (Figure 2). As shown in Figure 2, the additive noise has more effects on E fields compared to H fields as the DUT is magnetic field dominant. The noisy information (Figure 2) with position error was used to estimate the sources from (7).

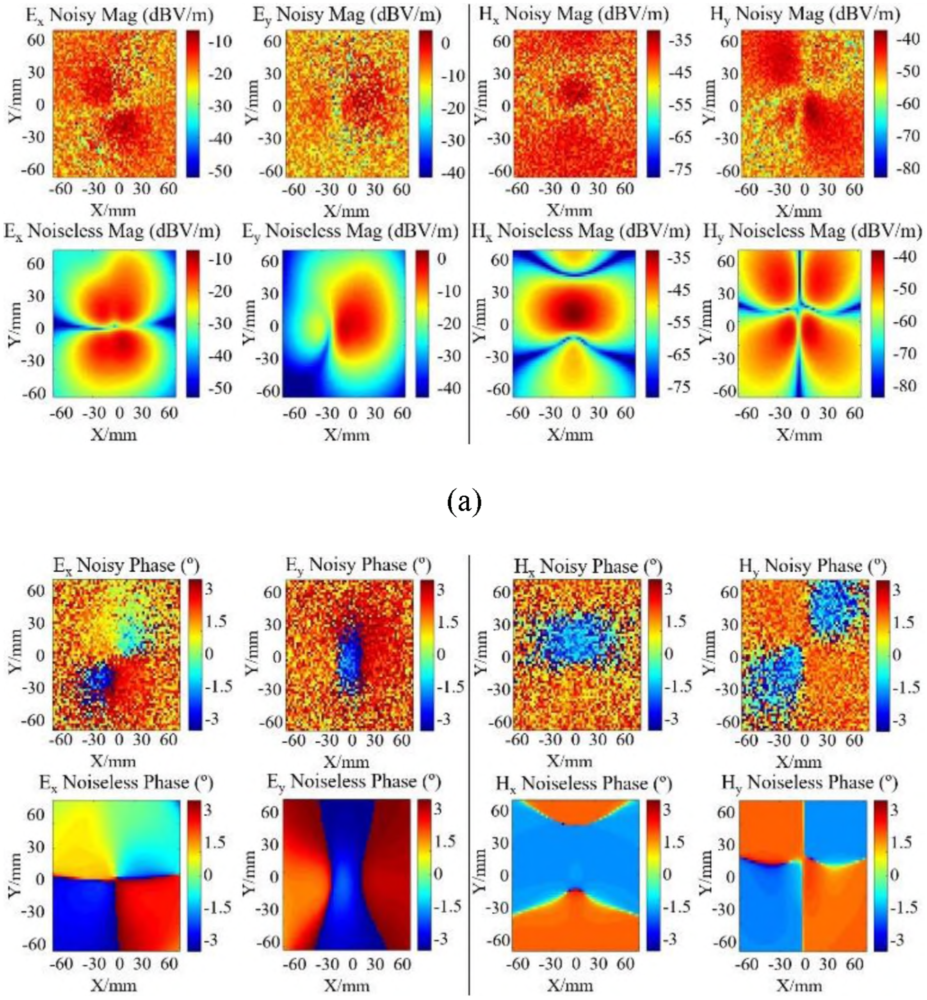

(a)

(b)

Figure 2. Effect of adding cross field coupling and random noise to the captured fields above EMI filter: a) Magnitude of noisy and noiseless data for Ex, Ey, Hx and Hy, b) Phase of noisy and noiseless data for Ex, Ey, Hx and Hy.

The prediction algorithm was applied to 40 combinations of additive random noise, each combination with 43 randomly selected dipole combinations. Each dipole combination has a different number of dipoles in the x- and y- directions as well as different spacing between them. Figure 3 shows the result of the prediction algorithm (weighted coefficient δ) which was calculated with (8). As shown, the weighted coefficient δ is very small for three combinations e.g., combinations 21, 22 and 23. Combination 22, with 2 dipoles in the x- and y-directions, and a 4 mm gap, gave the minimum weighted coefficient (δ) (Figure 3).

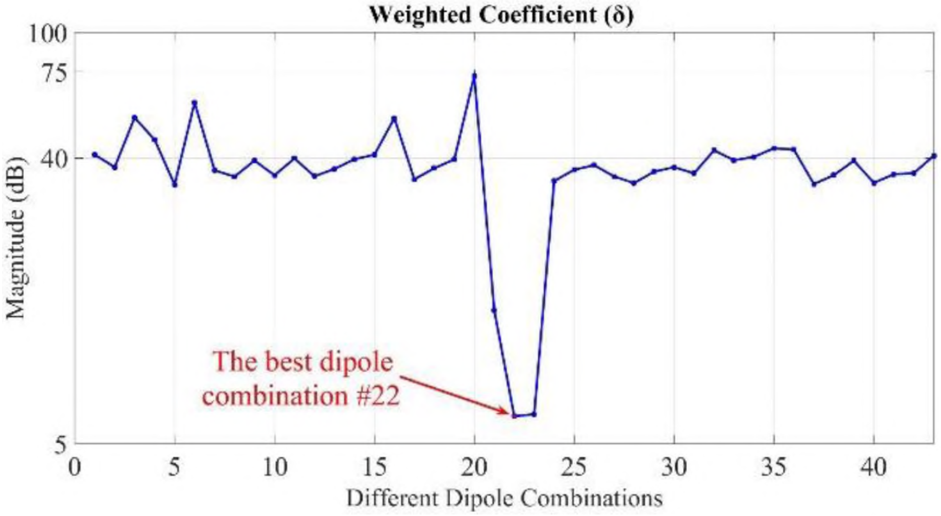

Figure 3. The magnitude of δ for different dipole combinations. The best dipole combination shows the lowest value of δ.

The variation of the GDM value (minima, maxima, and average) for the EMI filter model on three planes e.g., primary, secondary, and side plane, is shown in Figure 4 for different dipole combinations.

Secondary and side planes are used for validation of the method. As shown, the GDM is very sensitive to noise except for combination 21, 22 and 23. Additionally, the value of GDM is higher for all combinations except 21, 22 and 23, especially on the side plane. However, the best dipole combination (combination 22) has the lowest GDM value on all planes. The fact that this combination has the lowest GDM and is very robust against noise i.e., it has the lowest standard deviation of GDM and TRP, guarantees the repeatability of the result in a noisy environment. The best dipole combination was shown to predict the TRP with less than a 2 dB error.

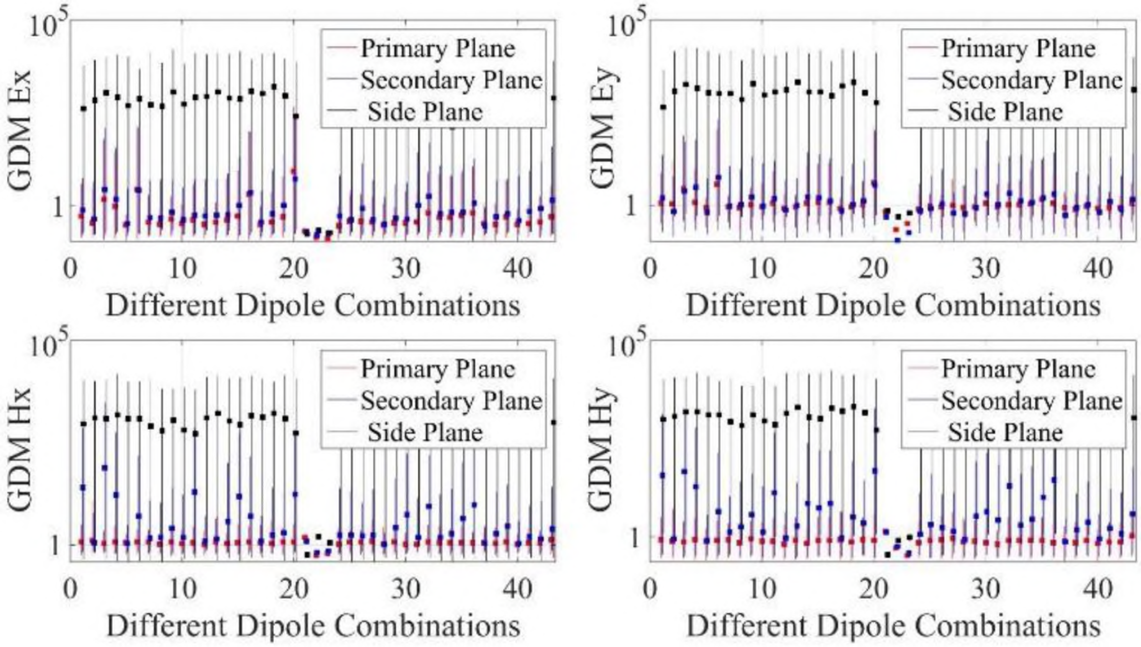

Figure 4. The variation of the GDM value (minima, maxima, and average) for the EMI filter model on three planes.

Figure 5 shows the reconstructed fields when using combination 22 from Figure 3 as the source. The predicted fields are compared with simulated noiseless data in the XY plane above the scan plane at Z = 62 mm and to the side of the DUT at X = 55 mm. The shape of the fields are reconstructed well. The GDM value is also lower than 1 which is considered as “Fair” for FSV evaluation.

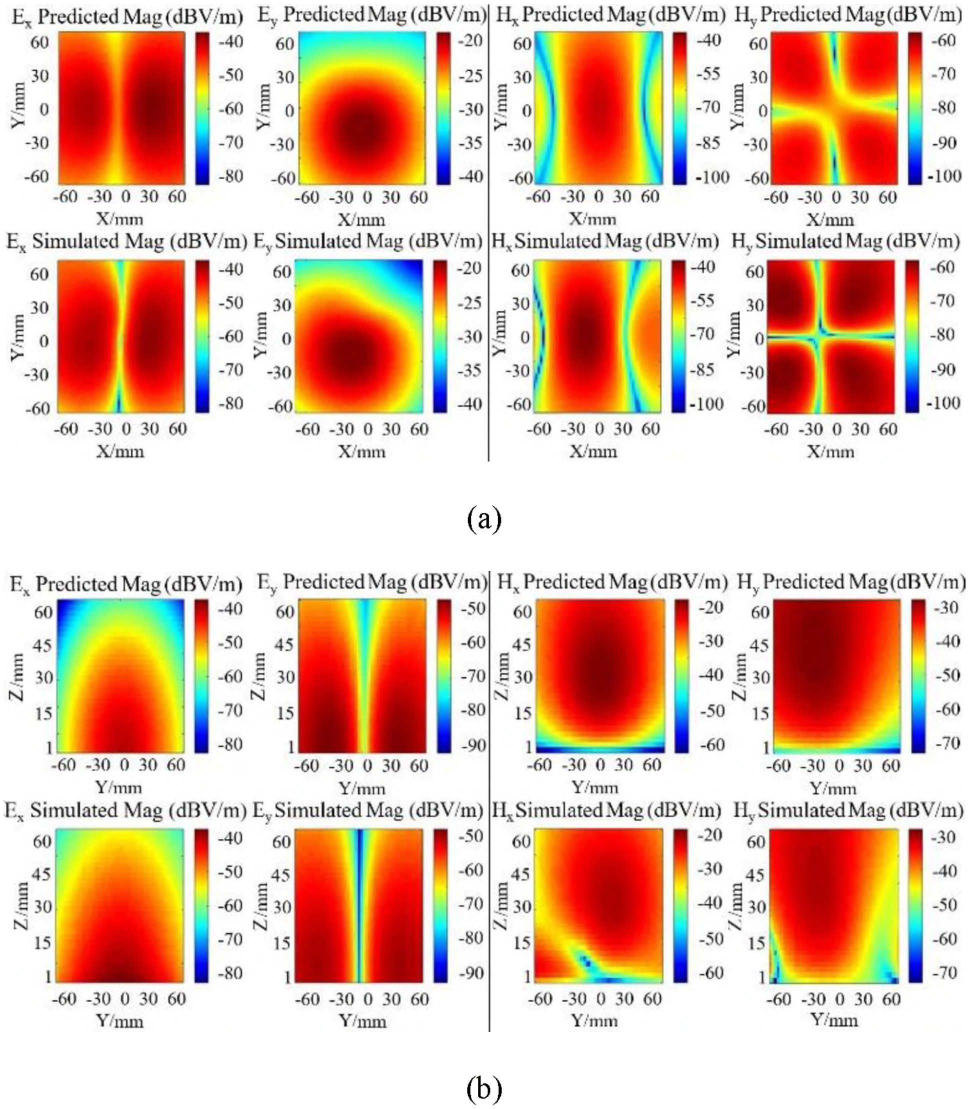

(a)

(b)

Figure 5. Noiseless simulated fields and predicted fields from noisy data for the EMI filter (Figure 1) using the best dipole combination (combination 22 from Figure 3): a) at Z = 62 mm and b) at X = 55 mm.

The accuracy of the estimated fields depends on the number of scanning points, as well as which field components are scanned e.g., Ex, Ey, Hx and Hy. Generally, either the electric or magnetic field (alone) can be used to reconstruct the source as long as the noise source is either electric or magnetic field dominant [6, 7, 9]. An EMI filter is a strong near magnetic field source due to a big inductor. Figure 6 shows the GDM value of the predicted fields on different planes using different numbers of scanning points and only using the measured value of magnetic fields over the scan plane. As shown, for an EMI filter which has magnetic-field dominated emissions, it is possible to use only around 30 measurements of only the magnetic field on a plane above the DUT (from Z = 40 mm to Z = 60 mm) to adequately reconstruct the source.

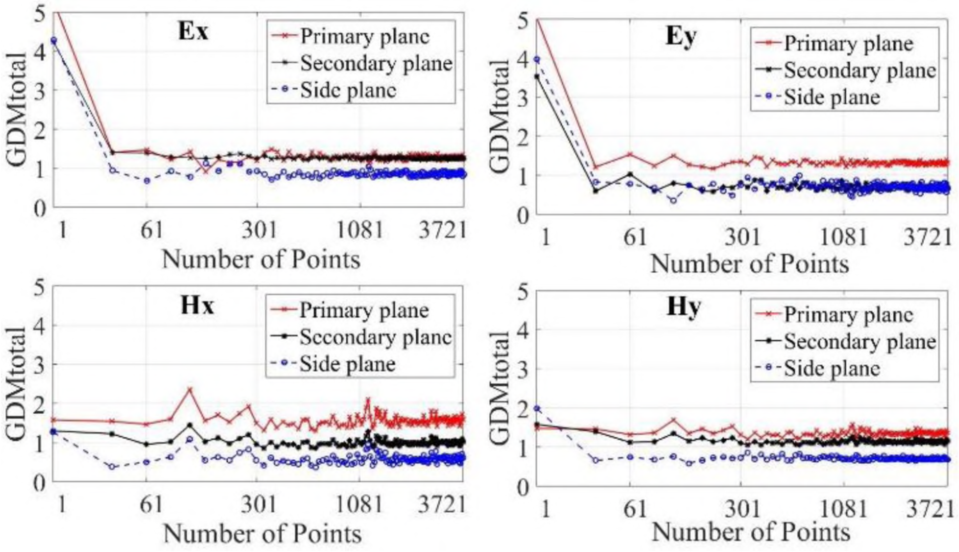

Figure 6. FSV evaluation on different planes using only magnetic field components for prediction versus different scanning points.

4.2. IC WITH OPEN AND SHORT TRACES

Another source of interference would be a more complex structure with both electric and magnetic fields. The IC with open and short traces shown in Figure 7 was used to study these more complex scenarios. The IC and two traces together may generate interference. The dimension of the ground plane was 120 mm × 120 mm (0.24 λ×0.24 λ at 600 MHz). Both traces were excited on one side at 600 MHz with a 1-V, 50 Ω port. One trace was terminated on the other side with a 1 Ω load and the other trace was left open.

The IC is a commercial microcontroller in a quad flat package (QFP). An electromagnetic model for the IC package was developed as part of the work described in [1]. The IC was mounted 0.4 mm above the PEC ground plane and was excited by two different 1-V, 50 Ω ports at 600 MHz. The fields generated by each stimulation source were found separately and then added to determine the emissions from the noise source DUT. Both magnetic and electric fields with phase were generated from these sources in CST Studio Suites [29] and used to validate methods for predicting interference using the source reconstruction technique.

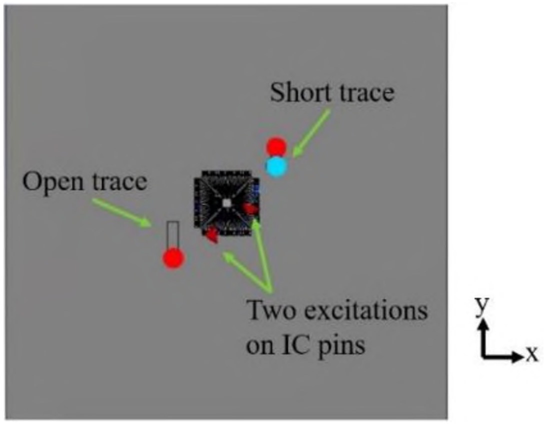

Figure 7. IC with two nearby traces.

Initially, the data was captured in a 120 mm × 120 mm observation plane at Z = 5 mm, with step size 2 mm (i.e., there were 3721 measurements of Ex, Ey, Hx and Hy within the plane). In order to investigate the effects of practical limitations on reconstruction, the cross-field coupling (about 30%) and random noise was added to the noiseless field so that the maximum SNR ≈ 15 dB. Figure 8 shows the magnitude and phase of the noiseless and noisy E- and H-fields. The noisy fields of Figure 8 with 1.5 mm position error have been used with (6) to estimate the sources.

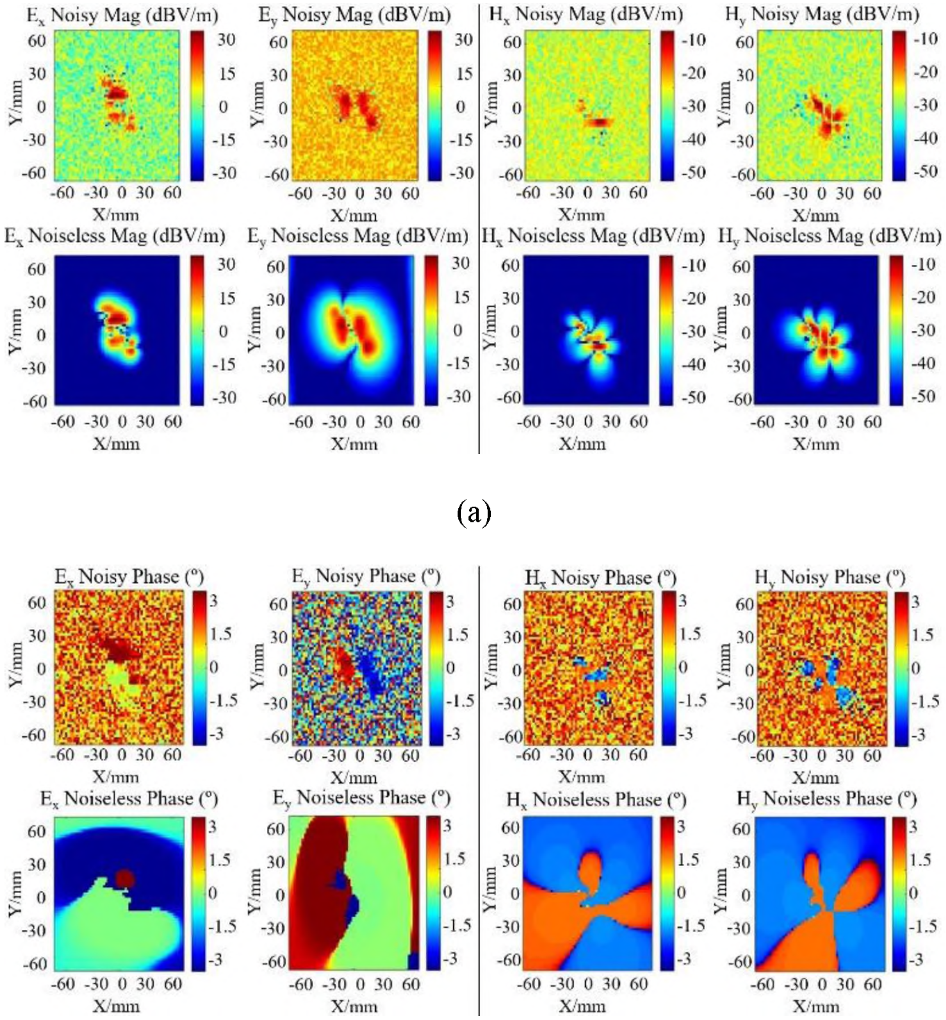

(a)

(b)

Figure 8. Effect of adding cross field coupling and random noise to captured fields above IC and two nearby traces: a) Magnitude of noisy and noiseless data for Ex, Ey, Hx and Hy, b) Phase of noisy and noiseless data for Ex, Ey, Hx and Hy.

Using noisy captured fields above the IC and trace model at Z = 5 mm, the prediction algorithm was repeated 40 times with 120 different dipole combinations. Each combination has different dipoles in the x- and y- directions as well as a different gap between them. The weighted coefficient (δ) was calculated with (8) and is shown in Figure 9. As shown, the weighted coefficient (δ) has a minimum value for combination 73 with 10 dipoles in the x- and y-directions, with a 3 mm gap. According to the proposed method, the combination 73 will show the lowest GDM value on the primary, secondary, and side planes (Figure 10). Additionally, total GDM value over the entire repetition of algorithm for 40 combinations of additive random noise will be minimum among all other dipole combinations (Figure 10).

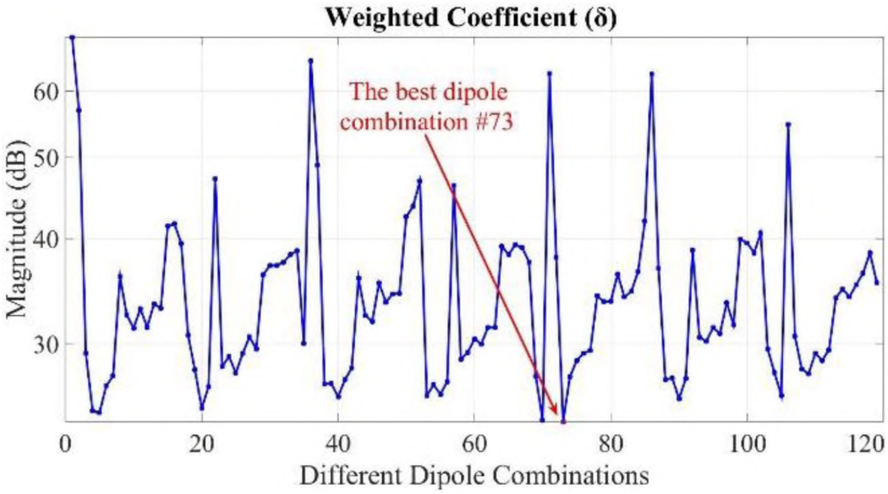

Figure 9. The weighted coefficient (δ) for different dipole combinations. The best dipole combination has the lowest δ for all 40 combinations of additive random noise.

The fact that combination 73 has the lowest total GDM for the primary, the secondary and the side planes is a strong evidence for the robustness of this combination against noise. Therefore, the weighted coefficient (δ) is a well-defined parameter which help the user find the best dipole combination with the best repeatability in a noisy environment. The best dipole combination was shown to predict the TRP with less than a

2.2 dB error. The best combination (combination 73 shown in Figure 9) was used to predict the fields from the noisy scan field at Z = 5 mm. Figure 11 compares the predicted fields with the noiseless simulated fields to the side of the DUT, at X = 20 mm. The shape of the fields is reconstructed well.

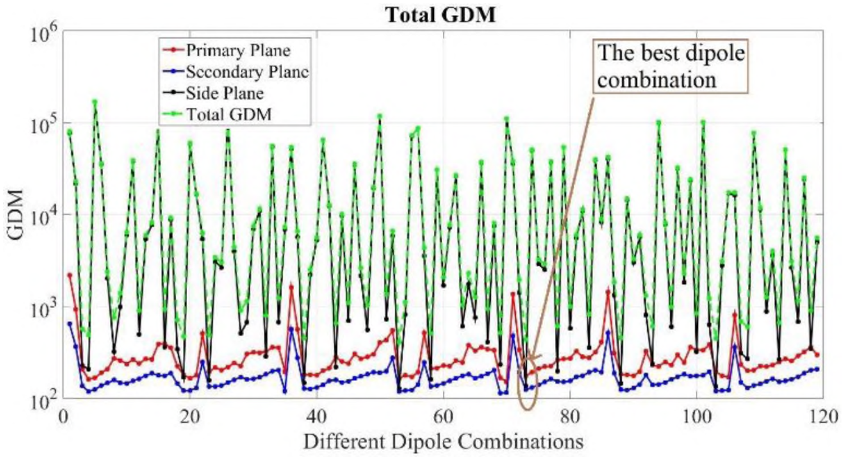

Figure 10. FSV evaluation on different planes versus different combinations.

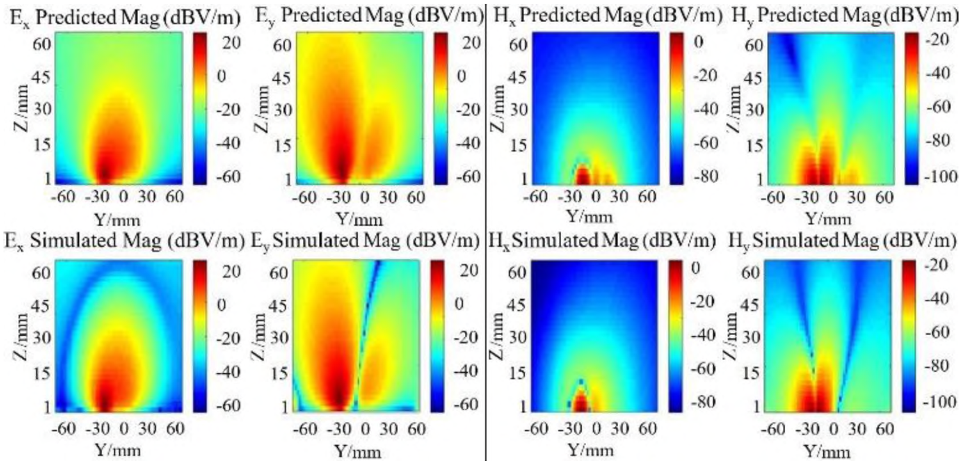

(a) (b)

Figure 11. Simulated and predicted E- and H-fields at X = 20 mm for the best dipole combination (combination 73 from Figure 10). a) E- b) H- fields.

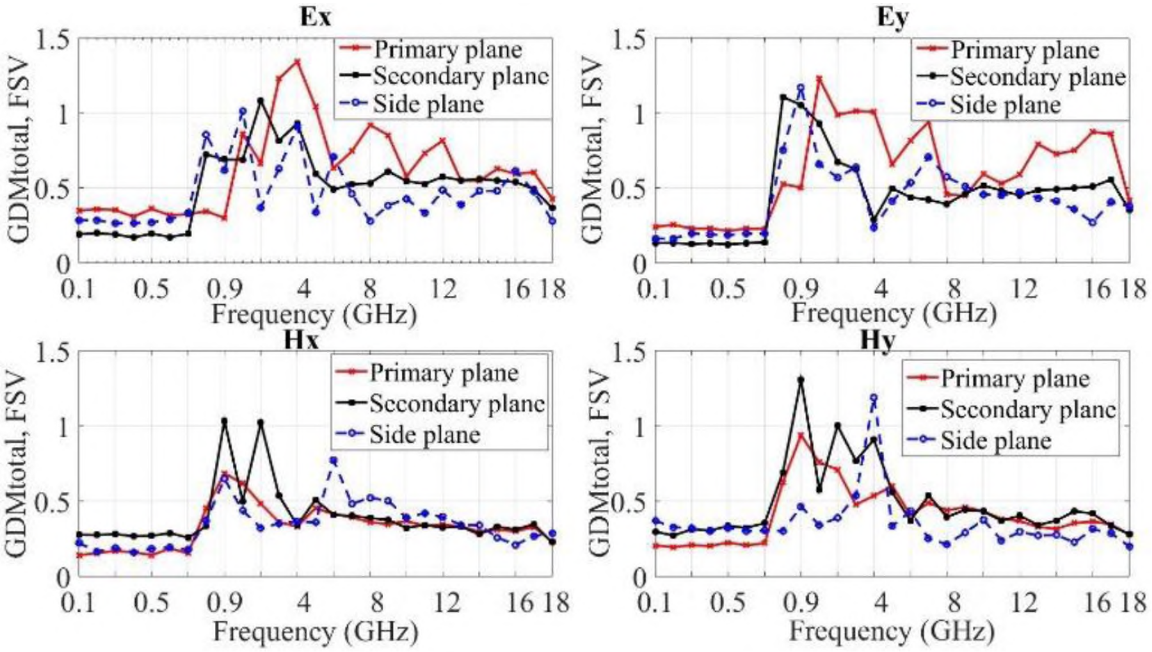

Figure 12. FSV evaluation using the best dipole combination versus frequency.

In a near-field plane where the maximum field on the edges is approximately 20 dB lower than the overall maximum field is sufficient for a proper field reconstruction since the overall scanning plane is affected by a strong noise floor [30]. Therefore, the number of scanning points can be decreased from 3721 points which was selected initially to only 500 points above the source area with the field strength about 20 dB higher than the noise floor (Figure 8).

Using 500 points, sources were reconstructed over 0.1-17 GHz. The GDM value of the predicted fields is shown in Figure 12. Therefore, the method can reconstruct the source successfully for electrically small and large DUTs using sparse scanning data. The GDM value is lower than 1.4 which is considered a successful field prediction for our EMC application.

5. VALIDATION THROUGH MEASUREMENT

Measurements of the electric and magnetic fields over a test board were used to validate the simulated results. The x- and y- components of the electric and magnetic probes were measured with a near-field scan system. The probes were calibrated for accurate phase-resolved near-field scanning [25]. A Vector Network Analyzer (VNA) was used for scanning of the field components and for a reference signal to obtain accurate phase-resolved results. Figure 13 shows the DUT and the measurement planes. The measurement setup is shown in Figure 14.

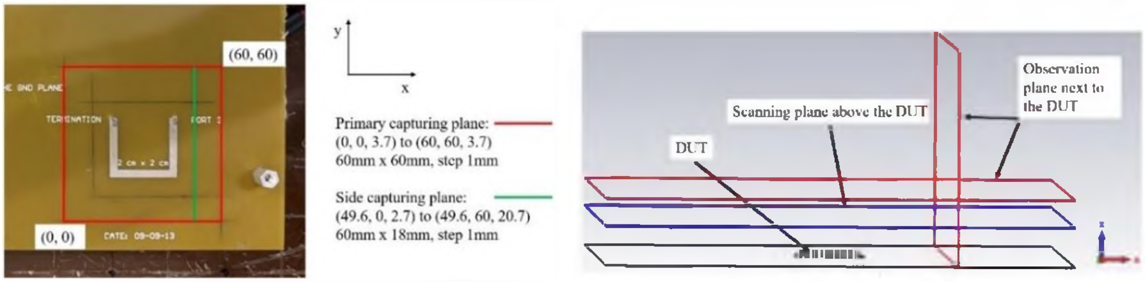

(a) (b)

Figure 13. Near-field scans were performed over the DUT: a) test board overlaid with the source surface; b) measurement and observation planes relative to the noise source.

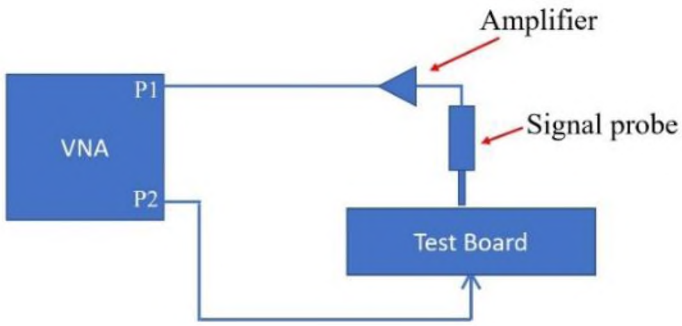

Figure 14. Block diagram of the measurement setup.

The primary scanning plane was 60 mm × 60 mm with a step size of 1.5 mm (1681 measurement points) at $Z = 3.7$ mm. The dipoles were mounted at $Z = 1$ mm, which is close to the physical height of the DUT. The secondary and side observation planes were mounted at $Z = 6.7$ mm and $X = 27$ mm (Figure 13). Using noisy captured fields above the DUT at $Z = 3.7$ mm, the prediction algorithm was repeated 40 times with 110 different dipole combinations. Each combination has different dipoles in the x- and y- directions as well as a different gap between them. However, with strong random noise added to the system, one of the combinations (combination 59 with 11 dipoles in the x- and y-directions, respectively, with a 3.5 mm gap) provides the minimum weighted coefficient (Figure 15).

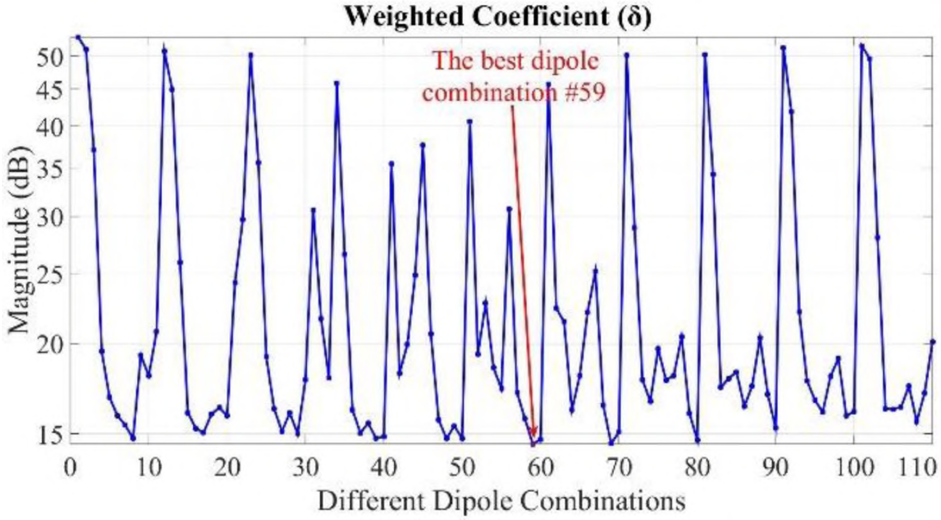

Figure 15. The weighted coefficient (δ) for different dipole combinations. The best dipole combination has the lowest δ for all 40 combinations of additive random noise.

As shown, the best dipole combination has the lowest variation in a noisy environment. The total GDM value for the DUT on three planes e.g., primary, secondary, and side plane, is shown in Figure 16 for different dipole combinations. As shown, the best dipole combination provided by the method has the lowest GDM value. Figure 17 shows the measured and predicted fields in the YZ-plane at X = 27 mm. Here, the shape of the electric fields is constructed well, and the GDM value is also lower than 1, which is considered as "Fair" for FSV evaluation.

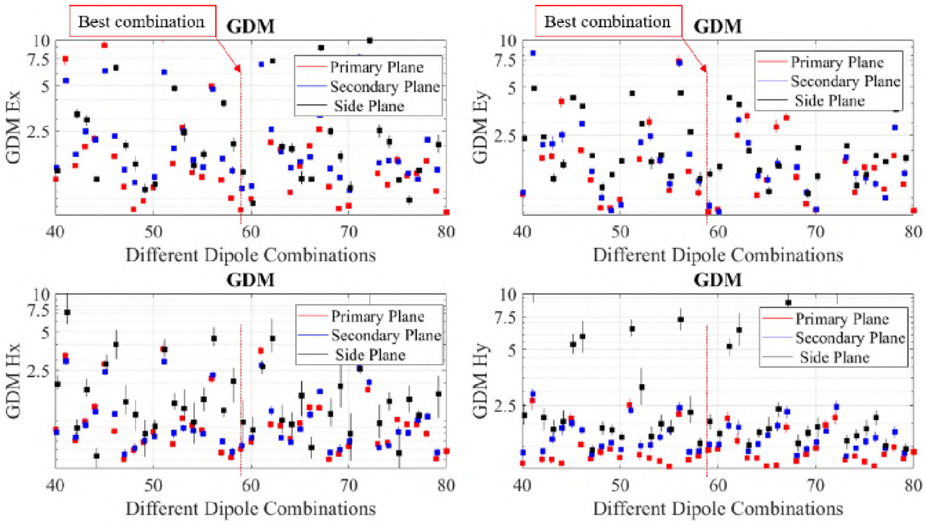

Figure 16. GDM evaluation on different planes for different dipole combinations.

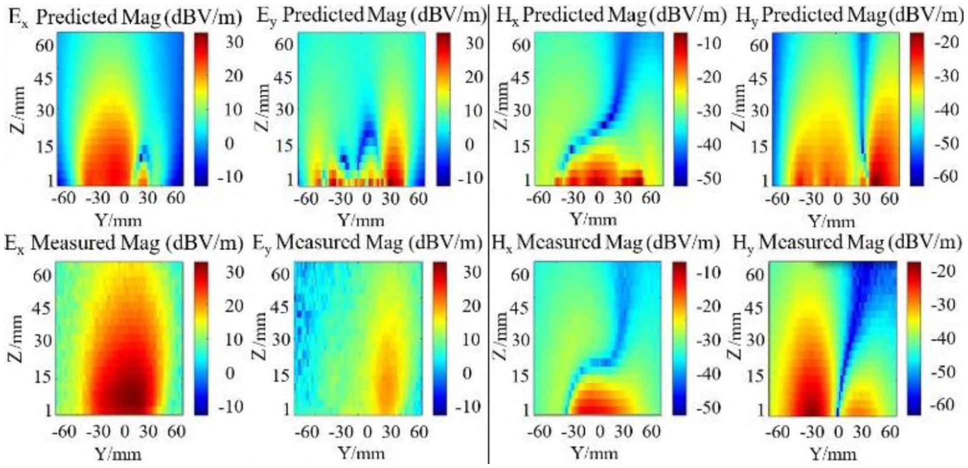

Figure 17. Measured and predicted E- and H-fields from the DUT (Figure 13) at X = 27 mm using the best dipole combination (case 59 of Figure 15).

6. DISCUSSION

Different methods have been developed to solve a source reconstruction problem and provide a possible solution for the EMI source reconstruction through the near-field scanning. However, all previous works studies one or two DUTs at a frequency with a predefined equivalent source without considering any measurement error other than white gaussian noise. Minimizing the least square error does not necessarily lead to a good representation in the presence of perturbation noise or other measurement or modeling errors [9]. Therefore, the user needs to determine if a solution, which is a combination of source type, location, number of sources, etc. is sensitive against perturbation noise or not.

This study helped the user to find the best equivalent source in the presence of typical measurement errors (e.g., random measurement noise in the scan data, errors in scan height, cross coupling between electric and magnetic field measurements) for near and far field applications over a wide frequency range for electrically large and small DUTs. It also analyzed the impact on field reconstruction to the side of the device (where most RFI problems occur) when using sparse scan data from above the DUT made with different scan step sizes.

Real measurements, however, include cross field coupling and position errors already, so the user can consider only random noise (e.g., SNR $\approx$ 15 dB) to run the proposed algorithm and find the best dipole combination. The proposed approach can also be implied to any other source reconstruction methods, e.g., inverse MoM to find the best equivalent source which is robust against perturbation noise. The only limitation of this method would be the number of initial guess e.g., initial dipole combinations as source representations, which is defined by the user. A study is needed to minimize the number of initial guess for different dipole combinations and make the algorithm mush faster. The impact of initial dipole combinations on simulation time should be investigated in the future.

7. CONCLUSION

Methods were developed to estimate an equivalent dipole representation of sources from near-field scans of the electric and magnetic fields. This dipole representation was evaluated based on its ability to estimate the fields above the scan plane, the fields next to the DUT, and the total radiated power. The scans were performed above the DUT while the magnitude and phase were biased with defined noise e.g., random error with SNR as high as 15 dB, cross field coupling with up to 30 % of the magnitude and phase of the unwanted coupled field, and up to 1.5 mm position error on the electric field locations. The proposed reconstruction method was validated with simulated and measured results of different noise sources, e.g., with electrically small and large electric or magnetic dominant noise sources over a wide frequency band. A 2D FSV method was used to evaluate the fields prediction both above and to the side of the DUT, which shows the field prediction was successful.

The presented data indicates that the method works with minimal scanning points from the top of the DUT. Furthermore, a clear decision process with examples was provided to guide the user in finding the best dipole representation since the user must be able to know which of the many solutions (dipole combinations) is the best and how representative it is.

REFERENCES

[1] H. Rezaei, J. Meiguni, M. Sørensen, R. Jobava, V. Khilkevich, J. Fan, D. G. Beetner, D. Pommerenke, "Source Reconstruction in Near Field Scanning using Inverse MoM for RFI Application," *IEEE Transaction on Electromagnetic compatibility*, pp. 1628-1636, vol. 62, no. 4, August 2020.

[2] H. Rezaei, J. Meiguni, M. Soerensen, J. Fan, D. Pommerenke, "Source Reconstruction in Near Field Scanning using Inverse MoM for RFI Application", *IEEE International Symposium on Electromagnetic Compatibility, Signal & Power Integrity (EMC+ SIPI)*, pp. 584-589, July, 2019.

[3] M. Sørensen, I. B. Bonev, O. Franek and G. F. Pedersen, "Assessment of the Huygens' Box Method with Different Sources Near Obstacles," in *IEEE Transactions on Electromagnetic Compatibility*, vol. 62, no. 2, pp. 433-442, April 2020.

[4] M. Sørensen, O. Franek, G. F. Pedersen, A. Radchenko, K. Kam, and D. Pommerenke, "Estimate on the uncertainty of predicting radiated emission from near-field scan caused by insufficient or inaccurate near-field data: Evaluation of the needed step size, phase accuracy and the need for all surfaces in the Huygens' box," *in Proc. Int. Symp. Electromag. Compat., Rome, Italy*, 2012, pp. 1–6.

[5] P. Wilson, "On Correlating TEM Cell and OATS Emission Measurements," *IEEE Transaction on Electromagnetic Compatibility*, vol. 37, no. 1, pp. 1-16, Feb. 1995.

[6] Y. F. Shu, X. C. Wei, R. Yang, and E. X. Liu, "An iterative approach for EMI source reconstruction based on phase less and single-plane near-field scanning," *IEEE Trans. Electromagn. Compat.*, vol. 60, no. 4, pp. 937–944, Aug. 2018.

[7] L. Wang, Y. Zhang, F. Han, J. Zhou, Q. Huo Liu, "A phase less Inverse Source Method (PISM) Based on Near-Field Scanning for Radiation Diagnosis and Prediction of PCBs", *IEEE Transactions on Microwave Theory and Techniques*, vol: 68, no: 10, pp: 4151 – 4160, Oct. 2020.

[8] W. Labiedh, J. Ben Hadj Slama, "Analysis and Modeling of the Magnetic Near Fields Emited by an IGBT and by a Power Diode Generic Radi ating Model for Active Components", *International Conf. on Electrical Sciences and Technologies in Maghreb (CISTEM)*, Nov. 2014.

[9] L. Li, J. Pan, C. Hwang, and J. Fan, "Radiation Noise Source Modeling and Application in Near-Field Coupling Estimation", *IEEE Trans. On Electromagnetic Compatibility*, vol. 58, no. 4, pp. 1314-1321, Aug. 2016.

[10] C. Wu, Z. Sun, Q. Huang, Y. Wang, J. Fan, J. Zhou, "A Method to Extract Physical Dipoles for Radiating Source Characterization and Near Field Coupling Estimation", *IEEE International Symposium on Electromagnetic Compatibility, Signal & Power Integrity (EMC+ SIPI)*, pp. 580-583, 2019.

[11] M. M. Hernando, A. Fernandez, M. Arias, M. Rodriguez, Y. Alvarez, and F. Las-Heras, "EMI radiated noise measurement system using the source reconstruction technique," *IEEE Trans. Ind. Electron.*, vol. 55, no. 9, pp. 3258–3265, 2008.

[12] Z. Yu, Mei Chai, Jason A. Mix, Kevin P. Slattery, and Qing Huo Liu, "Inverse Source Solver for a High Resolution Near Field Scanner in Microelectronic Applications", *IEEE Trans. On Components, Packaging and Manufacturing Technology*, vol. 4, no. 9, SEP. 2014.

[13] H. Zhao, Sihong Tao, Zhizhang Chen, and Jun Hu, "Sparse Source Model for Prediction of Radiations by Transmission Lines on a Ground Plane Using a Small Number of Near-Field Samples", *IEEE Antennas and Wireless Propagation Letters*, vol. 18, no. 1, Jan. 2019.

[14] K. Kwak1, Tae-il Bae, Kichul Hong, Hyungsoo Kim, Jingook Kim, "Accuracy investigation of equivalent dipole arrays for near-field estimation in presence of shielding or dielectric structures," *Microwave Opt. Technol Lett.*, pp. 1-9., 2019.

[15] J. Pan, H. Wang, X. Gao, C. Hwang, E. Song, H.-B. Park, and J. Fan, "Radio-Frequency Interference Estimation Using Equivalent Dipole-Moment Models and Decomposition Method Based on Reciprocity", *IEEE Trans. On Electromagnetic Compatibility*, vol. 58, no. 1, pp. 75-84, Feb. 2016.

[16] H. Zhao, X. Li, Z. Chen, and J. Hu, "Skeletonization-Scheme-Based Adaptive Near Field Sampling for Radio Frequency Source Reconstruction", *IEEE Internet of Things Journal*, vol. 6, no. 6, pp. 10219-10228, Dec. 2019.

[17] S. Lee , Y. Zhong , Q. Huang, T. Enomoto, S. Seto, K. Araki, J. Fan, and C. Hwang, "Analytical Intra-System EMI Model using Dipole Moments and Reciprocity", *IEEE International Symposium on Electromagnetic Compatibility and IEEE Asia-Pacific Symposium on Electromagnetic Compatibility (EMC/APEMC)*, May 2018.

[18] X. C. Wei, Y. F. Shu, Z. K. Hu, Y. H. Zhong, Y. W. Wang, "A Summary of Artificial Neural Networks on Electromagnetic Interference Diagnosis", *International Conf. on Microwave and Millimeter Wave Technology*, May 2019.

[19] Y. F. Shu, X. C. Wei, J. Fan, R. Yang, Y. B. Yang, "An Equivalent Dipole Model Hybrid With Artificial Neural Network for Electromagnetic Interference Prediction", *IEEE Transactions on Microwave Theory and Techniques*, pp: 1790-1797, vol.: 67, no: 5, May 2019.

[20] Z. K. Hu, Y. H. Zhong, Y. W. Wang, Y. F. Shu, X. C. Wei, “Application of Artificial Neural Network for Electromagnetic Source Reconstruction:, *IEEE International Conference on Computational Electromagnetics*, 20-22 March 2019.

[21] Z. K. Hu, Y. H. Zhong, X. C. Wei, Y. W. Wang, Y. F. Shu, “A Novel Electromagnetic Interference Source Reconstruction Method based on Artificial Neural Network”, *12th International Symposium on Antennas, Propagation and EM Theory (ISAPE)*, Dec. 2018.

[22] J. He, Q. Huang, J. Fan, “Dipole Source Reconstruction By Convolutional Neural Networks”, *IEEE International Symposium on Electromagnetic Compatibility & Signal/Power Integrity (EMCSI)*, July 2020.

[23] Q. Huang, J. Fan, “Machine Learning Based Source Reconstruction for RF Desense”, *IEEE Transactions on Electromagnetic Compatibility*, vol. 60, no. 6, pp: 1640-1647, Dec. 2018.

[24] A. P. Duffy, A. J. M. Martin, A. Orlandi, G. Antonini, T. M. Benson, and M. S. Wolfson, “Feature selective validation of computational electronics (CEM), Part I—The FSV method”, *IEEE Transaction on Electromagnetic Compatibility*, vol. 48, no. 3, pp. 449-459, Aug. 2006.

[25] S. Yang, Q. Huang, G. Li, R. Zoughi, and D. J. Pommerenke, “Differential E-Field Coupling to Shielded H-Field Probe in Near-Field Measurement and a Suppression Approach”, *IEEE Transaction on Instrumentation and Measurement*, vol. 67, no. 12, pp. 2872-2880, Dec. 2018.

[26] E. Petritoli, F. Leccese, L. Ciani, G. Schirripa Spagnolo, “Probe Position Error Compensation in Near-field to Far-field Pattern Measurements”, *IEEE 5th International Workshop on Metrology for Aerospace*, June 2019.

[27] S. F. Razavi and Y. Rahmat-Samii, “Resilience to probe-positioning errors in planar phaseless near-field measurements,” *IEEE Trans. Antennas Propagation*, vol. 58, no. 8, pp. 2632–2640, 2010.

[28] R. He, Y. Xu, S. Walunj, S. Yong, V. Khilkevich, D. Pommerenke, H. L Aichele, M. Boettcher, P. Hillenbrand, A. Klaedtke, “Modeling Strategy of EMI Filters”, *IEEE Tran. on Instrumentation and Measurement*, vol. 62, no. 4, July 2020.

[29] “CST microwave studio,” [Online]. Available: https://www.cst.com

[30] X. Tong, D. W. P. Thomas, A. Nothofer, C. Christopoulos, and P. Sewell, “Reduction of Sensitivity to Measurement Errors in the Derivation of Equivalent Models of Emission in Numerical Computation”, *ACES Journal*, vol. 26, no. 7, July 2011.

IV. ANALYZING THE INFLUENCE OF IMBALANCED TWO- OR THREE-WIRE VHF LISN ON RADIATED EMISSIONS FROM AC CABLES

Hossein Rezaei

Department of Electrical Engineering
Missouri University of Science and Technology
Rolla, Missouri 65409–0050
Tel: 573–308–9313
Email: hrr7d@mst.edu

ABSTRACT

This study analyzes a new imbalanced two- or three-wire termination for AC main cables, suggested by the VCCI standard group. This termination provides the basis for a new line impedance stabilization network (LISN) whose objective is to improve testing repeatability between different labs while also providing an imbalanced termination condition. Standard balanced LISNs do not reproduce the imbalanced terminations seen in practice. An imbalanced two- or three-wire VHF LISN was built, which can handle up to 15 A on each line.

The LISN operates from 30-200 MHz and provides an isolation on each line between input and output greater than 50 dB. This prototype provides a specified degree of conversion from differential mode to common mode current, which can increase radiated emissions. This conversion was found to be as high as 12 dB in measurements of a power line communication device.

3D full-wave simulations of two- and three-wire applications demonstrate that the radiated emissions from the prototype imbalanced termination and the ideal imbalanced

termination are nearly equal. The new LISN was further found to improve measurement reproducibility, reducing the standard compliance uncertainty from 15.5 dB in CISPR 16-4-1 to 9.5 dB.

1. INTRODUCTION

Common mode conducted emissions are typically measured using a line impedance stabilization network (LISN) [1, 9]. A LISN is a filtering device providing (a) isolation of the device-under-test (DUT) from AC power lines and related radio frequency (RF) disturbances, (b) a well-defined reference impedance at the LISN DUT port, and (c) the necessary power to the DUT. Typical LISNs use a balanced termination structure [3-9]. Round-robin results for radiated emissions using a balanced VHF LISN (Figure 1) show than the average emissions among different sites were generally within 4 dB when using the LISN [3, 4], but that deviations in measurements were as large as +18/-10 dB when the DUT was plugged directly into the building mains [3, 4]. Although a goal of the balanced VHF LISN is to reduce variations among tests [1-9], one can argue a balanced termination is unrealistic in practice.

The LISN forms an impedance between the wires of the power cable and the chamber ground, and thus can be used as a common-mode absorption device above 30 MHz. If the common mode impedance of the LISN is between 50 and 300 Ω, most of the common mode resonances of the power cable will be suppressed. Suppressing these resonances reduces the dependence of the emissions on the power cable routing, the specific impedance of the chamber's power connection, and the length of the power cord.

While reducing this dependence is attractive for minimizing chamber to chamber variations, it also hides an important effect that causes radiation. In real installations, the differential mode noise current is often larger than the common mode noise current in a power cable, and real installations will have asymmetric common-mode impedances [10, 11]. This asymmetry will convert differential mode current into common mode current, which can radiate. To mimic this effect, a defined asymmetry can be introduced into the VHF LISN.

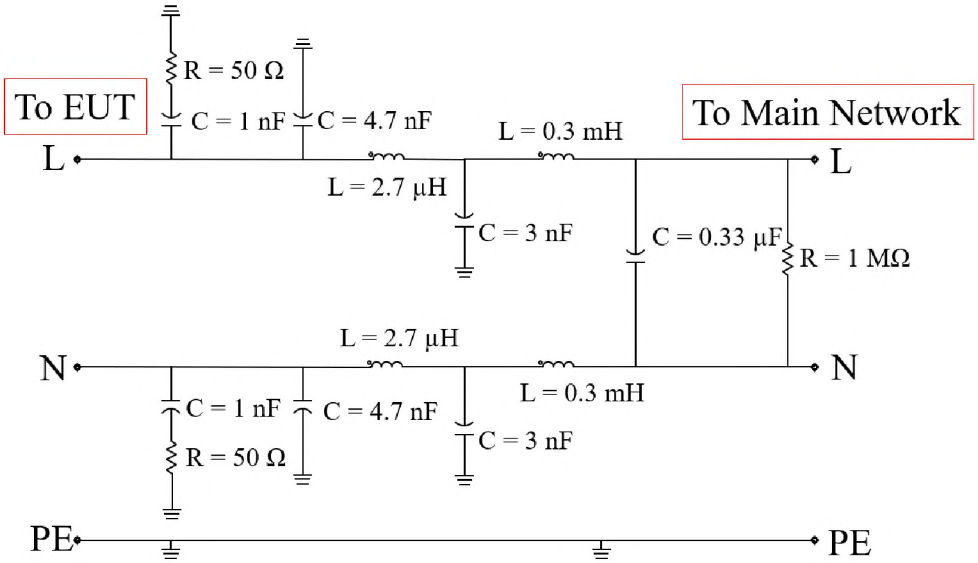

Figure 1. Circuit diagram of a typical balanced VHF LISN [4, 7, 8].

Using an imbalanced Coupler Decoupler Network for Emission – Mains (CDNE-M) will increase the common-mode emissions by about 10 to 15 dB up to 200 MHz depending on the DUT compared to using a balanced CDNE-M [11].

About 10 dB higher emission was also reported for an imbalanced two-wire LISN compare to a balanced one over 0.5-30 MHz in [11]. To address the differential- to common-mode current conversion in a VHF LISN (30-200 MHz), the termination impedance should have a controlled imbalance to provide a defined degree of conversion from differential- to common-mode current. The Japanese VCCI standards group has introduced an imbalanced termination for this purpose and suggested that such a LISN should be created for the frequency range of 30-200 MHz [10].

In this paper, an imbalanced LISN was designed, built, and analyzed to serve as the termination of the mains power during radiated EMI CISPR16/CISPR 35 testing [1]. This LISN was designed to supply power for imbalanced two- or three-wire measurements up to 15 A over a frequency range from 30-200 MHz.

A 3D full-wave simulation with both differential- and common-mode excitation was used to illustrate the effect of the VHF LISN on radiated emissions on a typical test set-up.

A study of differential- to common-mode current conversion was performed to verify the conversion ratio for an ideal imbalanced termination. In a real test setup, the differential- to common-mode current conversion is geometry dependent but not a fixed number. Measurements of a pair of power line communication devices were performed to validate the performance of the LISN in a typical test set-up and to calculate the ratio of differential- to common mode current conversion for a real word application.

2. DESIGN OF AN IMBALANCED TWO- OR THREE-WIRE LISN

This section introduces the imbalanced two-wire and three-wire terminations which suggested by VCCI group, provides evidence of the validity of the selection of the proposed impedances, shows the characteristics of the actual LISN which was built and calculates differential- to common-mode conversion ratio for a practical test setup with an imbalanced two wire termination.

2.1. IMBALANCED TWO- OR THREE- WIRE TERMINATION

An imbalanced two- and three-wire terminations which proposed by VCCI [10] is shown in Figure 2a and Figure 2b, respectively. From Figure 2, six different terminations are specified for two- and three-wire terminations as:

In two-wire applications:

- Common Mode impedance = 150 Ω ± 10 % @ 30 MHz ~ 200 MHz, which is the impedance of two wires (L shorted to N) referenced to the ground-plane.
- Differential Mode impedance = 100 Ω ± 10 % @ 30 MHz ~ 200 MHz: This is defined as the impedance of L to N while N is shorted to the ground-plane.
- The impedance of L to the ground-plane = 250 Ω ± 20 % @ 30 MHz ~ 200 MHz.

In three-wire applications:

- Common Mode impedance = 90 Ω ± 10 % @ 30 MHz ~ 200 MHz, which is defined as the impedance of (L shorted to N shorted to PE) to the ground-plane.
- Differential Mode impedance = 100 Ω ± 10 % @ 30 MHz ~ 200 MHz, which is defined as the impedance of L to (N shorted to PE shorted to the ground-plane).
- Tertiary Mode impedance = 60 Ω ± 10 % @ 30 MHz ~ 200 MHz: This is defined as the impedance of (L shorted to N) to (PE shorted to ground plane).

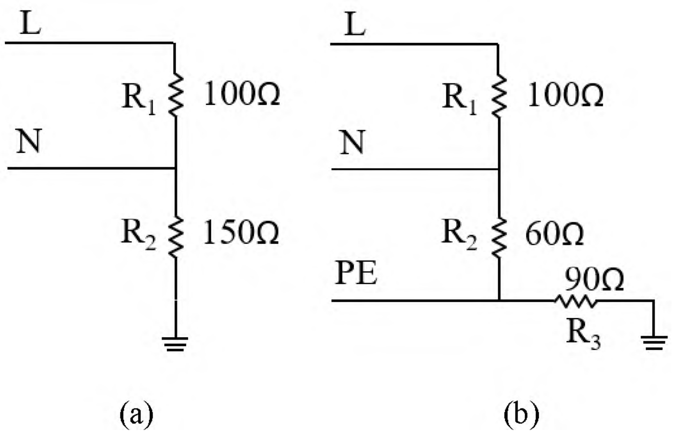

Figure 2. Schematic of the proposed imbalanced termination, a) two-wire termination, b) three-wire termination.

From Figure 2 and suggested terminations, there are three main impedances which should be verified, e.g., common-mode impedance (Z_{CM}), differential-mode impedance (Z_{DM}) and tertiary-mode impedance (Z_{TM}).

The geometry of a power cable connecting a DUT to a power outlet does not allow for easily assigning a common-mode impedance, as the wave structure deviates strongly from a TEM mode wave. However, it has been shown that termination impedances in the range of 50-200 Ω suppress standing waves well [12]. Although not exact, using a common-mode impedance of about 150 Ω (Figure 2a) will provide results similar to those observed in [12]. Thus, no common-mode resonances will occur [12-14].

Since the two wires (L and N) form a transmission line, the typical cable geometry has been given as the reason for the selection of 100 Ω as the differential impedance [10]. As the value was given by [10], this argumentation was not further investigated. In order to provide evidence of the validity of the selection of 100 Ω for the differential mode impedance, 48 different cables were measured using a TDR (Figure 3). Eleven cables were two wire cables, and 37 cables were three wire cables. The distribution of the characteristic impedances is shown in Figure 4. The distribution shows the typical value of the differential impedance is close to 100 Ω. This typical value has motivated the authors of [10] to select Z_{DM} = 100 Ω for both the two- and three-wire imbalanced terminations.

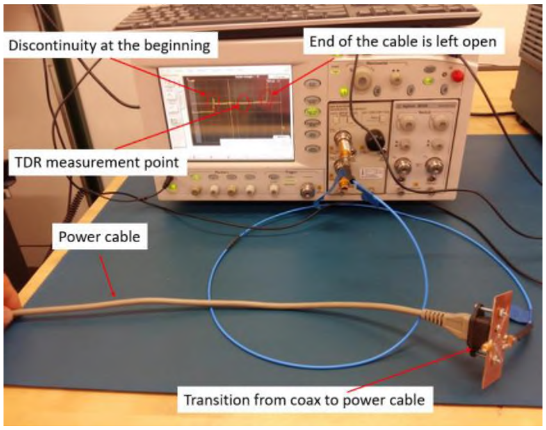

Figure 3. Measurement setup with power cord cable and TDR for DM impedance measurement.

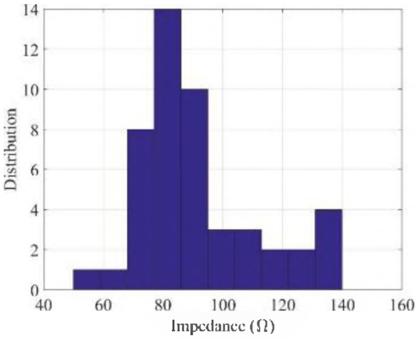

Figure 4. Distribution of differential-mode impedances for power cables.

Figure 2b shows the proposed imbalanced three-wire termination [10]. As before, the differential-mode impedance is defined between the line (L) and the neutral (N) to be

100 Ω. The common-mode impedance is between all three wires (L, N, and PE) shorted together to ground. Although the actual differences of the characteristic impedances may be much smaller, a 150 Ω common-mode termination was selected for two-wire [10], and a 90 Ω termination was selected for the slightly thicker three-wire cables [10].

An impedance value of 60 Ω was selected for when L and N are shorted together and referenced to PE [10]. This transmission line has a lower impedance than the differential-mode transmission line formed by L against N. This impedance is called tertiary mode impedance (TM) in [10].

2.2. IMBALANCED TWO- OR THREE- WIRE LISN

Table 1 summarizes the characteristic of a LISN to be built. The circuit schematic of the imbalanced two- or three-wire LISN has been designed (Figure 5) to meet the characteristics of Table 1. The inductors in Figure 5 (L1, L2 and L3) allow for an AC connection, but their impedances need to be large enough so that the termination impedances are defined by the resistors (R1, R2 and R3).

Table 1. Imbalanced two- or three- wire VHF LISN (prototype).

Parameter	Explanation
Frequency	30-200 MHz
Network impedance	Two- or three- wire defined by the standard
Maximum current	15 A RMS
Maximum AC voltage	250 VAC, 50/60 Hz
Isolation on each line	Better than 50 dB

Six different impedances of the LISN that is built needing to be measured to validate that in fact the termination fit within the guidelines provided by VCCI group since there are extra parasitic in the system (not shown in Figure 5). This includes about a 2-pF parasitic capacitance to ground due to the effect of the SMA launch structure needed for the measurement on each line of Figure 5.

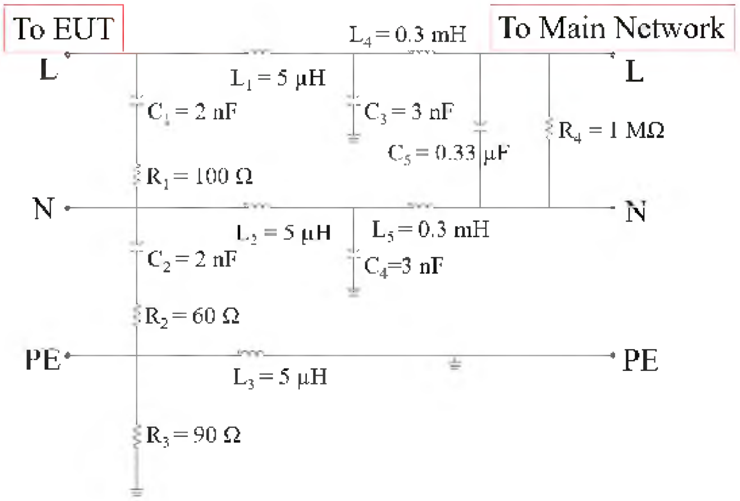

Figure 5. Circuit diagram of the proposed two- or three-wire imbalanced LISN.

However, this is a floating measurement, and the direct measurement of the impedances is not possible since every time different parasitic will change the result. Of course, it is not possible to measure all the defined impedances simultaneously, because the measurement points are changing every time. Therefore, a three port S-parameter measurement with a Vector Network Analyzer (VNA) is used which would have minimal size and capacitance to ground. A test fixture (Figure 6) has been built to connect the prototype to the vector network analyzer (VNA) for the three port S-parameter measurement.

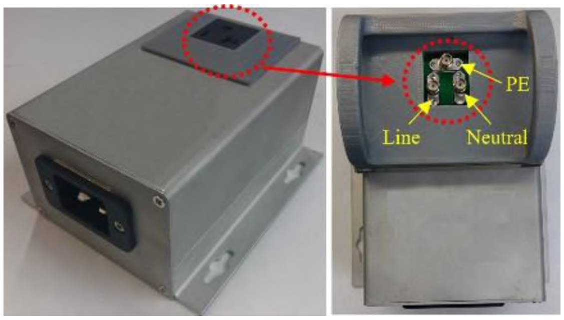

Figure 6. Prototype of imbalanced two- or three wire VHF LISN.

With the complete measured S-parameter matrix in Advance Design System (ADS) [15], all six different defined impedances have been calculated. The achieved impedances are compared to the nominal values in Figure 7 through Figure 10, showing that the deviations are within the ranges proposed by VCCI [10] which was shown in Section 2.1. As shown in Figure 7-10, the impedance of the LISN will vary with frequency around its nominal value. It is not easy to compare tolerances (expressed as percentages) of phases relative to magnitudes. It is more effective to observe each contribution, or the combined effect, to the goal, which in this case is the radiated fields.

The tolerance of 20% in magnitude and 0 to ± 20° in phase has been already reported for a balanced VHF LISN in [7, 16]. However, for the imbalanced VHF LISN, it has not yet been specified or reported. In [10], 10% change in the magnitudes of the impedances is considered, but there are no comments on the phase. Regardless, it is very difficult to have zero phase deviation. It will be shown later in this study in Section 3 that the effects of phase and magnitude variations (up to 30° variation on phase plus 10 % change in the magnitude) is less than ± 3 dB on the radiated emissions, which is acceptable in EMC applications. We believe ± 10% change in magnitude and ± 30° in phase can be considered as a limit for defining an imbalanced VHF LISN.

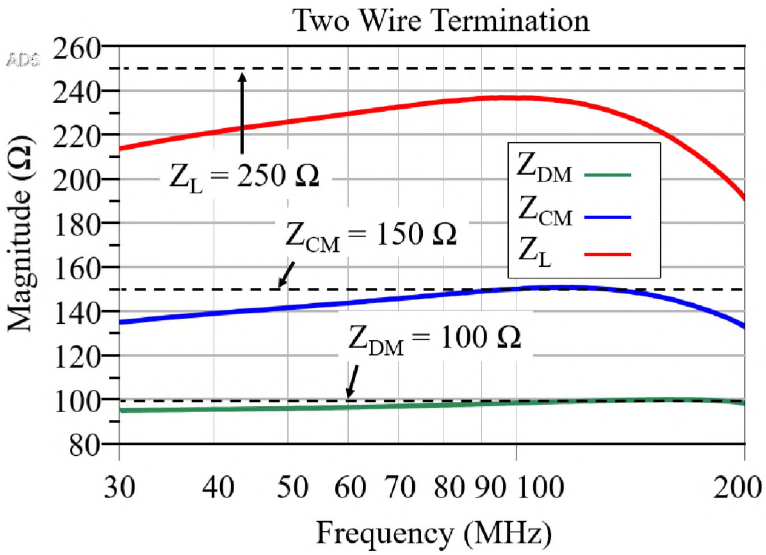

Figure 7. Magnitude of the impedance of the prototype for a two-wire application. The deviation from the nominal value is within 10% from 30-200 MHz.

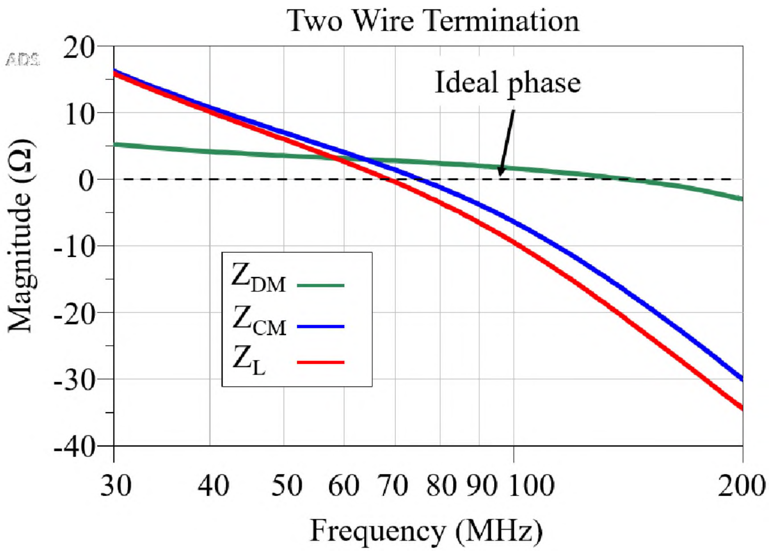

Figure 8. Phase of the impedance of the prototype for a two-wire application. The deviation from the nominal value is <35° from 30-200 MHz.

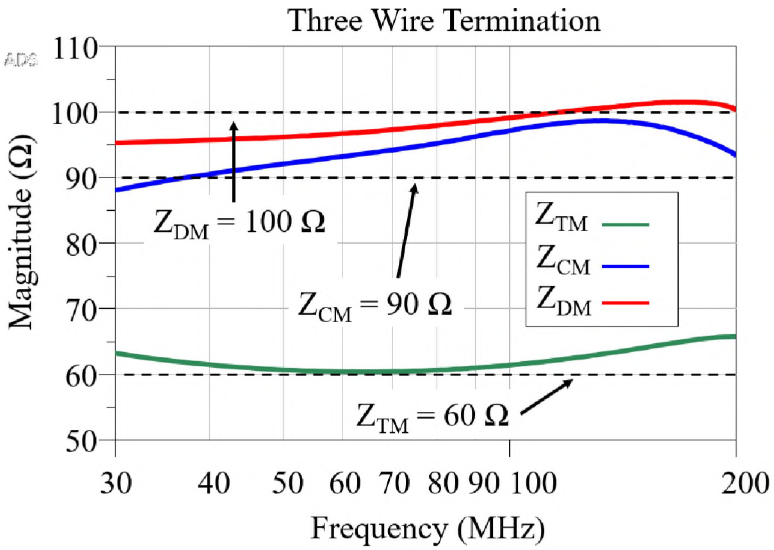

Figure 9. Magnitude of the impedance of the prototype for a three-wire application. The deviation from the nominal value is within 10% from 30-200 MHz.

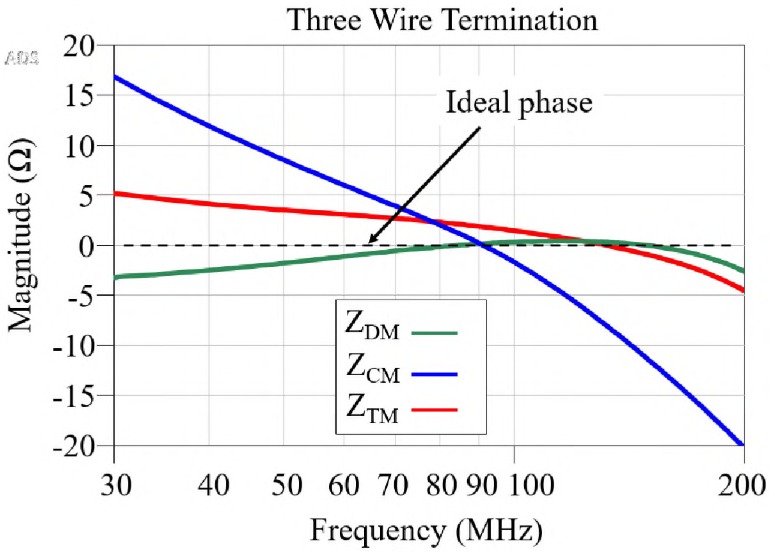

Figure 10. Phase of the impedance of the prototype in a three-wire application. The deviation from the nominal value is <30° over 30-200 MHz.

2.3. DIFFERENTIAL MODE TO COMMON MODE CONVERSION

Without imbalance termination, an important mode of emission is not tested, i.e., a potentially serious differential to common-mode conversion in the AC network, which causes strong radiation is ignored. A 3D full wave simulation model was used in this section to study the differential- to common-mode conversion ratio in the presence of a balanced or imbalanced termination for a typical test set-up. The model shown in Figure 11 illustrates a typical radiation test set-up [1].

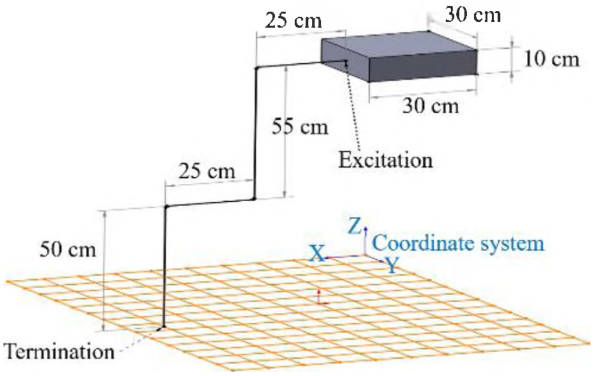

Figure 11. 3D full-wave simulation set-up for two wire.

The set-up uses a solid metal box (30 × 10 × 30 cm) located 1 m above an infinite ground plane to model the DUT. The box is connected to 1.5 m long wires for different excitations, e.g., differential-mode sources providing 1 V with a zero-output impedance. A low impedance (10 Ω) was selected to connect the wires to the DUT, because this causes similar voltage drops at an insufficient shield connection. By comparing with a 1 Ω resistance, it was verified that this selection of the connection impedance does not significantly influence the conclusions drawn from the simulation. A typical power cord geometry was used having:

1. A wire diameter of 1.62 mm,
2. A PVC insulation with 0.89 mm thickness,
3. and a PVC jacket with a diameter of 9.5 mm.

The metal-to-metal distance between the wires is 2.35 mm. This forms a transmission line of about 80 Ω between L and N. The circuit schematics of the full wave structure with balanced and imbalanced terminations are shown in Figure 12 and Figure 13, respectively, to illustrate the flow of common-mode currents.

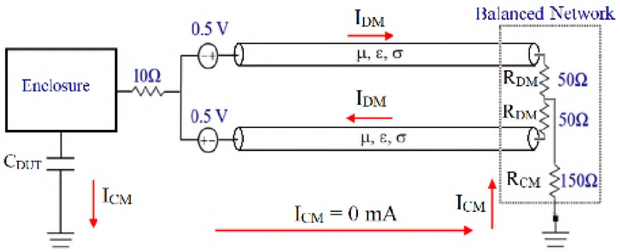

Figure 12. A balanced impedance to ground for a two-wire set-up.

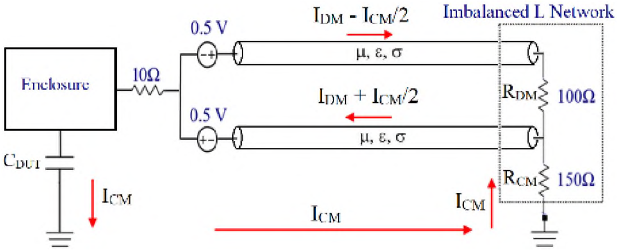

Figure 13. An imbalanced impedance to ground for two-wire set-up.

The coupling capacitance of the DUT to ground is about $C \approx 50\,\text{pF}$, which of course depends on the size of the DUT. This capacitance creates an impedance of about 100 Ω at 30 MHz. The characteristic impedance of the differential mode in the power cord is about 80 Ω. Simple models without transmission lines (TL) and an estimated value of the coupling capacitance between the DUT and ground can be found in [11]. As shown in Figure 12, there is no common-mode current due to the balanced termination, while the imbalanced termination converts differential-mode current into common-mode current (Figure 13) which increase radiated emission. According to [10, 11], real installations have imbalances, which should be reproduced by the EMC test set-up.

To calculate the differential- to common-mode conversion ratio, the full wave simulation model (Figure 11) with an imbalanced two-wire termination (Figure 13) was used for the frequency range of interest (30 - 200 MHz). The T network has two identical voltage sources of 0.5 V leading to a 1 V DM source which drives the differential-mode current (Figure 13). In addition, the imbalance in the LISN will create an additional common mode current. For the frequency range of interest (30 - 200 MHz), the impedance of C_{DUT} is comparable with RCM, and $I_{DM} \pm I_{CM}/2$ will flow (Figure 13). The full wave simulation result gives more detailed insight (Figure 14).

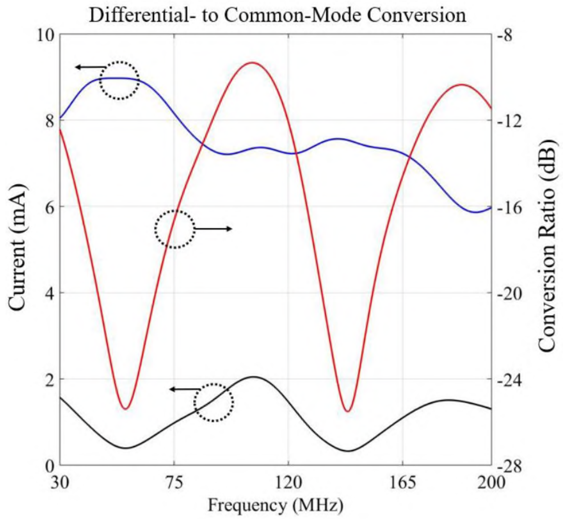

Figure 14. The current flowing in an imbalanced two-wire termination.

The differential mode current reduces with frequency as its 80 Ω transmission-line is terminated into 100 Ω. The common mode current is affected by the structural length and fluctuates around 1 mA. The differential- to common-mode conversion is defined as the ratio of the incident differential mode power that is returned along the cable towards the DUT in the common-mode. It can be calculated as:

$$\text{Conversion from DM to CM} = \frac{CM\,power}{DM\,power} = \frac{R_{CM} I_{CM}^2}{R_{DM} I_{DM}^2}. \tag{1}$$

Differential- to common-mode conversion ratio has been reported to be about -10 to -15 dB for an imbalanced CDNE-M [11]. However, the actual conversion ratio obtained through full wave simulation is somewhat geometry dependent and varies from -9 to -25 dB (Figure 14). Similarly, for a three-wire application (Figure 2b), the maximum differential- to common-mode conversion can be calculated to be about -19 dB. The conversion is smaller, because current will return not only via the ground plane and capacitively couple to the DUT, but also in the PE wire. The portion which returns in the PE wire does not contribute to the common-mode current.

3. RADIATED EMISSION USING THE IMBALANCED TWO- OR THREE-WIRE VHF LISN

As shown in the previous section, the impedance of the LISN will vary with frequency around its nominal value. The effect of these deviations on the radiation was quantified with full-wave simulation [17] using the setup shown in Figure 11. For the termination impedances on the ground plane side in Figure 11, the nominal values, the realized values, short, and open terminations have been selected. To capture the effect of the termination impedance (described by S-parameters) on the radiation, the co-simulation feature of CST was used. This combines the 3D full-wave simulation with a circuit simulation or measurement [18] by simultaneously solving for the EM fields and the circuit characteristics. Here, only linear S-parameters were included, and the simulation was performed as follows:

1. The set-up shown in Figure 11 was simulated. The termination is three lumped elements (Figure 15a). This simulation provides a reference for validation of the data.

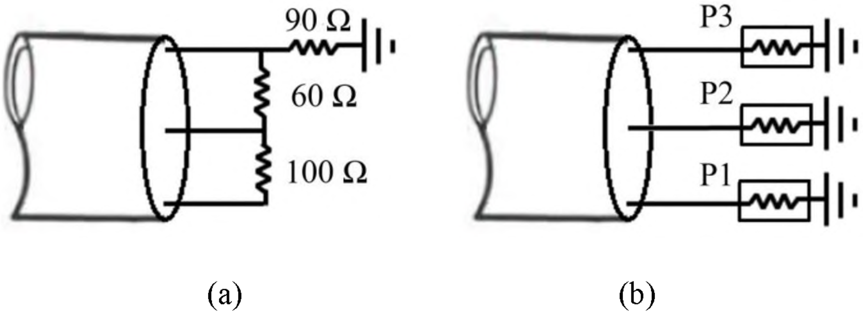

(a) (b)

Figure 15. Three wire terminations used in full wave, a) three wire imbalanced termination with lumped elements, b) three S-parameter ports.

2. Second simulation is performed with set-up (Figure 11) while the excitation is replaced with an S-parameter port. Three S-parameter ports (Figure 15b) should be mounted on the termination side. In CST design studio (with the co-simulation feature shown in Figure 16), the proper excitation was placed on the source side and an S-parameter block on the termination sides between the S-parameter -ports. The S-parameter result from an ideal termination (Figure 17a) was used to update the result, which was then verified against the reference result in step 1.
3. After successful validation in Section 2, the complete measured S-parameter matrix of the prototype in CST design studio was used to calculate the radiated emissions.

The maximum electric field in the far field region has been simulated with full wave software. Results are shown at a distance of 10 m. Table 2 summarizes all the settings used in the full wave simulation.

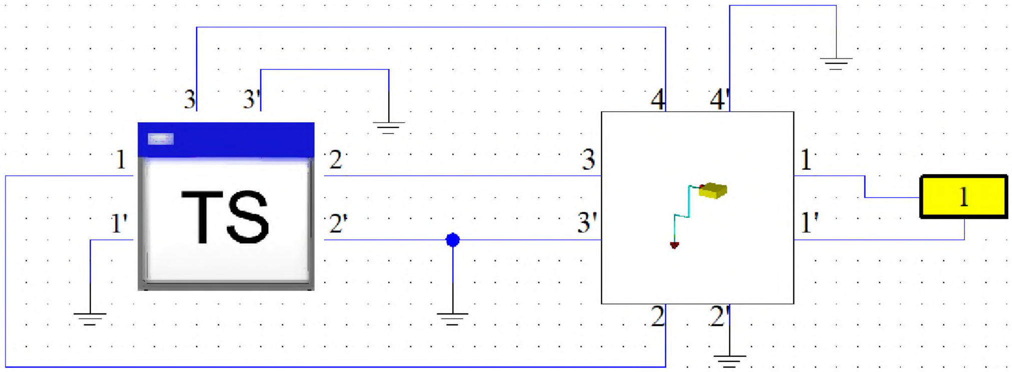

Figure 16. CST true transient EM/circuit co-simulation with S-parameter block.

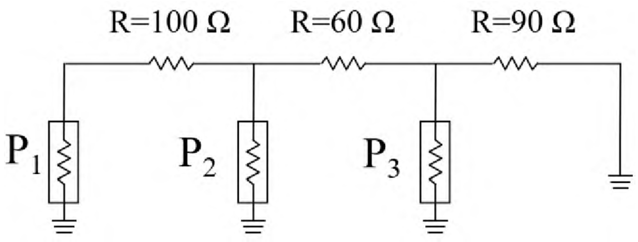

(a)

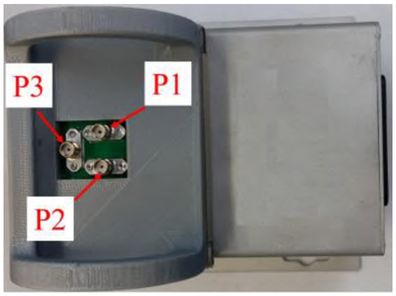

(b)

Figure 17. a) Port definition for ADS simulation of an ideal three wire imbalanced termination. b) Port definition for full S-parameter measurement of the prototype.

Table 2. CST setting for full wave simulation.

CST Setting	Explanation
Frequency	30-200 MHz
Background	Normal
Boundaries	Open in all directions except at Ymin (Et = 0)
Field Monitor	Far field / RCS, Transient Broadband
Setup Solver	Time Domain Solver
Post Processing	E-field, 3D, Max at 10 m distance

3.1. COMMON MODE EXCITATION WITH IMBALANCED VHF LISN

The schematic of the simulation set-ups with a common mode excitation and ideal imbalanced two and three-wire terminations are shown in Figure 18. The maximum far-field radiation for different three-wire terminations (Figure 18c), e.g., open, short, or ideal termination (lumped elements in 3D full-wave solver) are shown and compared to the real termination of the prototype in Figure 19. For the two-wire set-up, termination would be similar to Figure 18a and discussion would be the same as the three-wire set-up.

Strong resonances were observed for terminations with open and short conditions (Figure 19). The first peak is around 50 MHz, which is below the quarter wavelength frequency for a 1.5 m wire length, because the capacitance of the box to the surroundings is about 50 pF. At resonances, the radiation can increase by up to 15 dB. Common-mode impedance damps resonances well. Therefore, the choice of 90 Ω for the common-mode impedance in three wire application seems reasonable with respect to repeatability. These results are in agreement with the previous study on the effect of common-mode impedance on radiation [2].

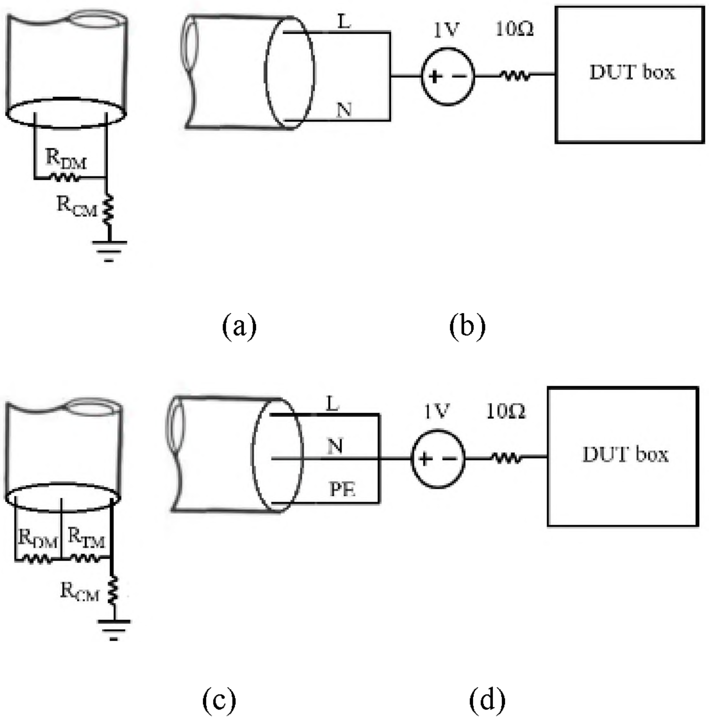

Figure 18. Schematic used in 3D full-wave simulation set-up, a) two-wire imbalanced termination, b) Common-mode excitation, c) three-wire imbalanced termination, d) Common-mode excitation.

As shown in Figure 19, the impedance termination is very important at lower frequencies, but it is not as significant at higher frequencies due to radiation from the wire. A lot of power is radiated before it reaches the common mode termination device. However, the radiation resistance will dampen some resonances. At higher frequencies, when wavelength is comparable to the length of the cable, the termination does not affect the radiation as much as it does at low frequencies. The black and blue curves in Figure 19 show the validation results from the co-simulation and the EM simulation with ideal terminations. The S-parameters from the circuit model of the prototype were exported and used in a 3D full wave simulation using the co-simulation feature to find the radiated emissions with a real imbalanced three-wire termination (the prototype termination). The green curve of Figure 19 shows radiated emissions from the prototype.

Comparing the blue and green curves of Figure 19, it is obvious that the radiated emissions for the real LISN (prototype) is nearly equal to the ideal termination case (Figure 15a). As shown in this section, the maximum radiated emissions using the prototype are similar to an ideal imbalanced termination in either a two- or three-wire application. That is, the performance of the prototype in terms of radiated emissions is close to the ideal termination with less than 2 dB error up to 200 MHz (red curve in Figure 19).

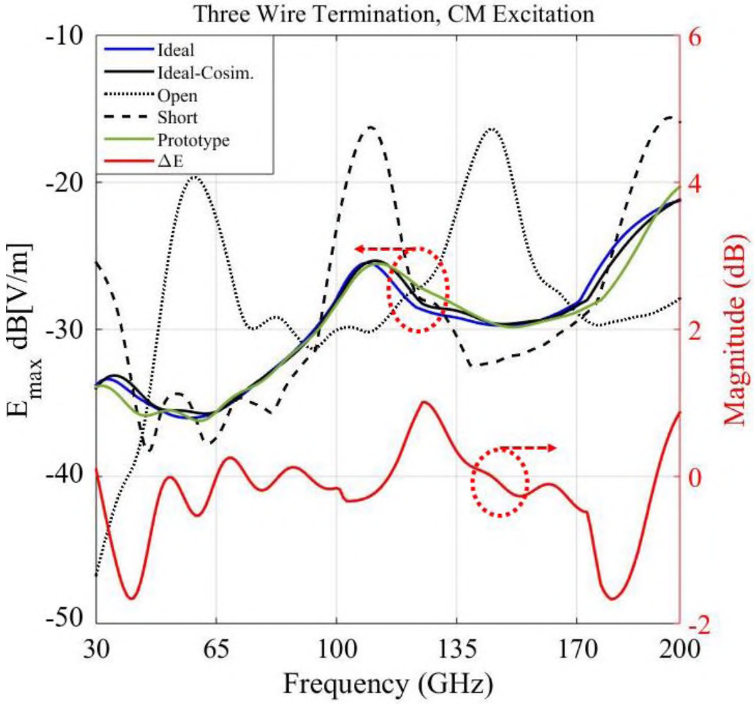

Figure 19. Simulation result showing the radiated emission for the three-wire set-up with CM excitation. The difference in radiation between the ideal and the real termination is ΔE <2 dB up to 200 MHz.

3.2. DIFFERENTIAL MODE EXCITATION WITH IMBALANCED VHF LISN

Figure 20 shows the differential-mode (DM) source excitation and the imbalanced termination in two- and three-wire set-ups. For both set-ups, the DM excitation is 1 V with zero output impedance. A low impedance (10 Ω) was selected to connect the wire to the DUT, as this causes similar voltage drops as an insufficient connection. Compared with a 1 Ω termination, it was verified that the selection of the connection impedance does not significantly influence the conclusions drawn from the simulation.

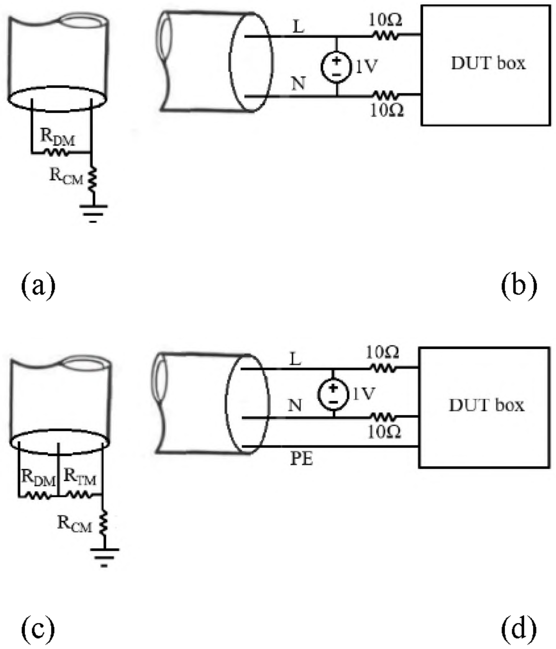

(a) (b)

(c) (d)

Figure 20. Schematic used in 3D full-wave simulation set-up, a) two-wire imbalanced termination, b) DM excitation for two-wire set-up, c) three-wire imbalanced termination, d) DM excitation for three-wire set-up.

Results of the radiated emissions for two- and three-wire setups with DM excitation are shown in Figure 21 and 22, respectively. When the ends of the wires on the termination side are open or shorted to the ground plane, the structures are symmetric. In this case, there is little current flowing in the circuit and very low radiation is observed. However, differential excitation creates a highly resonant system as shown in Figure 21 and Figure 22, because the source impedance is 0 Ω and the termination has no loss. With termination, these resonances will be dampened regardless of their source. Furthermore, there is a defined differential to common-mode conversion with either a two- or three-wire imbalanced termination, which increases the radiated emissions.

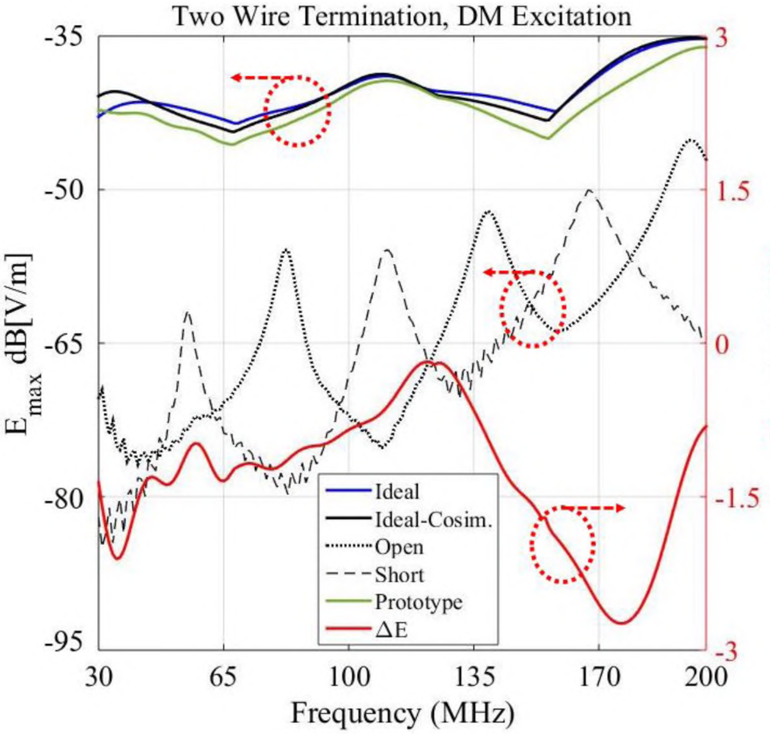

Figure 21. Simulation result showing the radiated emission for the two-wire set-up with DM excitation. The difference in radiation between using the ideal and the real termination is ΔE <2.5 dB up to 200 MHz.

As shown in Figure 21 and Figure 22, the co-simulation feature has been verified by using ideal terminations (Figure 2) for both the EM simulation and the co-simulation method. Then, the co-simulation feature is used to compare the radiated emission of an ideal termination (Figure 2) with the real termination of the prototype (Figure 7-10) in either a two- or three-wire applications. In terms of radiated emissions, the performance of the prototype was compared with the expected radiation and has less than a 3.2 dB difference up to 200 MHz (red curves in Figure 21 and Figure 22).

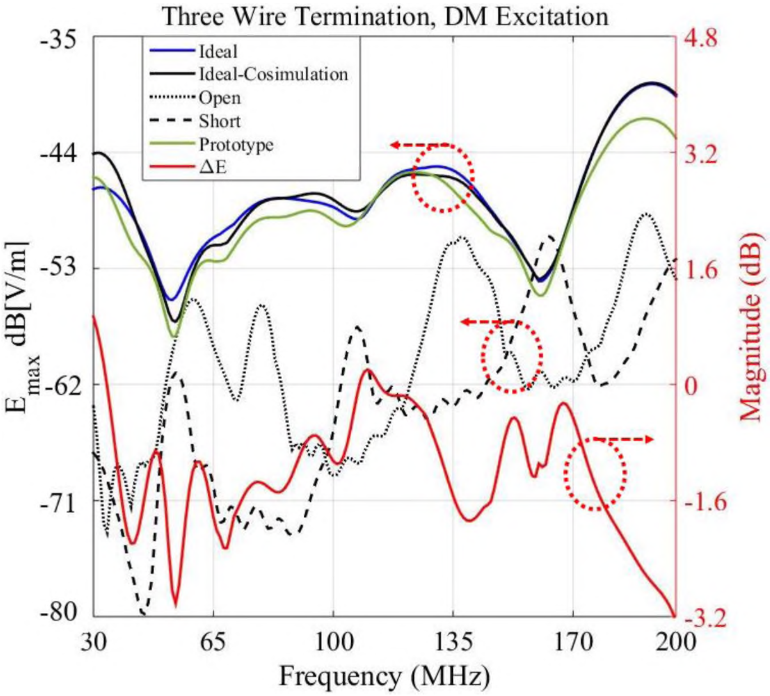

Figure 22. Simulation result showing the radiated emission for the three-wire set-up with DM excitation. The difference in radiation between using the ideal and the real termination is ΔE <3.2 dB up to 200 MHz.

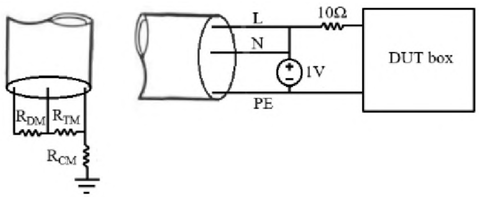

(a)

(b)

Figure 23. Schematic used in 3D full wave simulation setup, a) three-wire imbalanced termination, b) TM excitation.

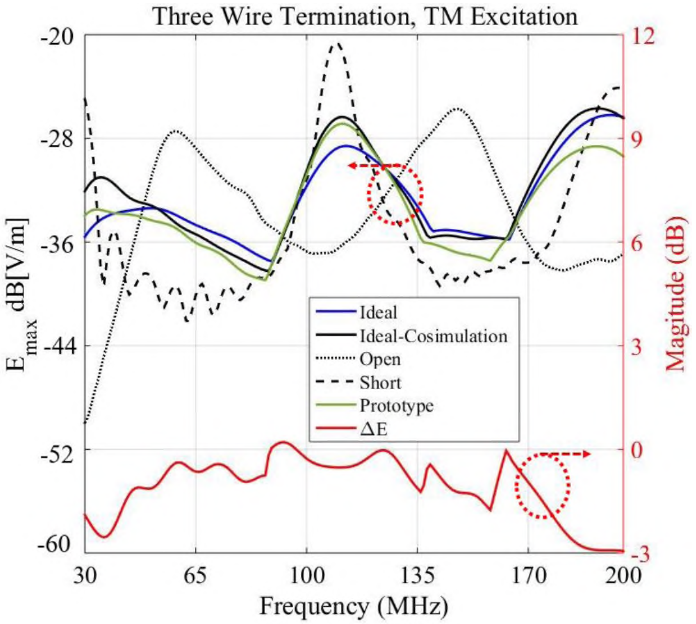

Figure 24. Simulation result showing the radiated emissions for the three-wire set-up with TM excitation. The difference in radiation between using the ideal and the real termination is ΔE <3 dB up to 200 MHz.

3.3. TERTIARY MODE EXCITATION WITH IMBALANCED VHF LISN

Figure 23 shows tertiary-mode (TM) source excitation and imbalanced termination in three-wire setups. The radiated emissions with TM excitation are shown in Figure 24. When the wires are open or short, the structure creates a highly resonant system. In the presence of terminations, these resonances will be dampened, regardless of their source. The radiation of the prototype is very close (with less than 3 dB error up to 200 MHz) to the radiation with an ideal termination (red curve in Figure 24).

3.4. IMPACT OF TERMINATION CONDITION ON MEASUREMENT UNCERTAINTY OF IMBALANCED VHF LISN

For the frequency range in which cable radiation dominates, the standard compliance uncertainty (SCU) is dependent on termination conditions [19]. Therefore, the sensitivity of the radiation behavior of the LISN due to deviations in the magnitude and phase of the terminating impedance from the ideal case should be analyzed. Uncertainty is considered in the CISPR 16-4-1 [20]. Here, the average combined standard uncertainty (Uc-scu) with the inclusion of the terminating condition of the main cable is defined to be:

$$U_{\mathrm{c-scu}} = \sqrt{U_{\mathrm{c-MIU}}^{2} + U_{\mathrm{a}}^{2} + U_{\mathrm{b}}^{2} + U_{\mathrm{c}}^{2}}, \tag{2}$$

where CISPR/TR 16-4-1 specifies [19, 20]:

- Combined Measurement Instrumentation Uncertainty (Uc-MIU) of 2.5 dB,
- uncertainty from the main cable arrangement (Ua) of 3.5 dB.
- uncertainty in the operating condition of DUT (Uc) of 1.7dB.
- and the uncertainty in termination conditions (Ub).

Having a rectangular probability distribution for the uncertainty of the cable terminating conditions, which is already considered in CISPR 16-4-1 [20], the uncertainty in the terminating condition (Ub) is defined as [19]:

$$U_{\mathrm{b}} = \frac{E_{\mathrm{max}} - E_{\mathrm{min}}}{2\sqrt{3}} = \frac{\Delta E}{2\sqrt{3}}. \tag{3}$$

Emax and Emin are the maximum and minimum electric field strengths in dBµV/m, respectively. If we consider the maximum deviation due to the termination condition of the prototype up to 200 MHz to be 3.5 dB (Figure 22 for a three-wire termination with DM excitation), the uncertainty in the terminating condition (Ub) is only 1 dB. Using (2), the average combined standard uncertainty (Uc-scu) is 4.7 dB. Therefore, the expanded standard uncertainty (USCU,VHF-LISN) is obtained:

$$U_{\mathrm{scu,\,VHF-LISN}} = 2 * U_{\mathrm{c-scu}} = 9.5 \text{ dB}. \tag{4}$$

The expanded standard uncertainty (USCU,VHF-LISN) is improved to 9.5 dB for an imbalanced two- or three-wire VHF LISN, which is about 2.5 dB better than the calculated value (USCU,VHF-LISN =12 dB) for a 50 Ω LISN in [19]. Compared to the 15.5 dB value currently defined in CISPR 16-4-1 [20], the SCU for an imbalanced two- or three-wire VHF LISN is improved about 6 dB.

4. VALIDATION THROUGH MEASUREMENT

The effect of the differential to common-mode conversion has been investigated using a power line communication device. The goal was to investigate the impact of termination conditions on emissions with a DUT which uses a strong differential-mode signal to transmit data over power lines [11].

The test uses different termination conditions e.g., a balanced LISN, imbalanced LISN, and without a LISN. A balanced LISN (Figure 1) was prototyped to compare with the imbalanced LISN. The balanced LISN has a 50 Ω impedance on each line with less than 1.5 Ω variations in magnitude and less than 5° variations in phase over the frequency range of 30 – 200 MHz.

A block diagram of the measurement setup inside the anechoic chamber is shown in Figure 25. Two DUTs are HD Power line adaptors (PLA5456), which communicate with each other through power lines. The measurement setup is shown in Figure 26. The DUTs and LISN are mounted on the floor such that the power cable produces a loop with the maximum radiated emissions toward the antenna.

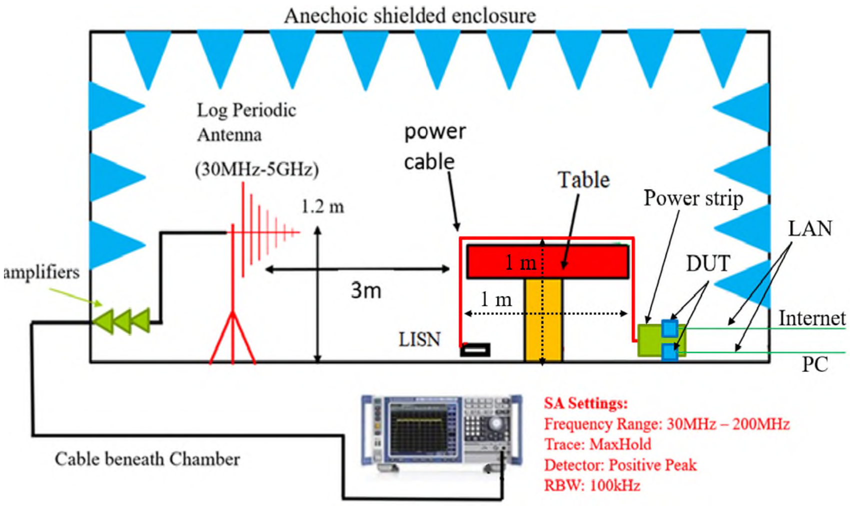

Figure 25. Block diagram of measurement setup with a power line communication device inside an anechoic chamber.

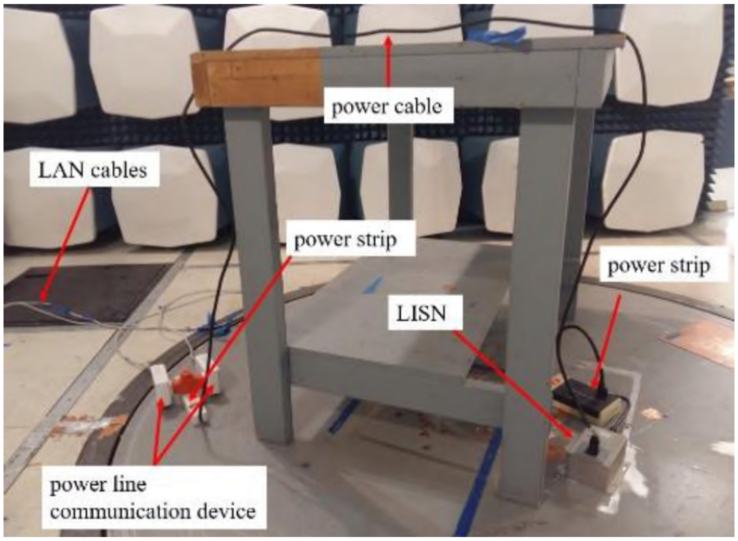

Figure 26. Measurement setup with a power line communication device inside an anechoic chamber.

A personal computer (PC) is needed to communicate with the DUT. To generate the highest differential-mode current, the DUT was operated under its maximum data rate. The measurement was performed for both horizontal and vertical polarizations and with height scanning (1 – 4 m) of the antenna. Also, the table has been partially rotated to capture the maximum radiation.

The goal is to show the differential to common-mode conversion by using an imbalanced LISN, but also to show the emissions with different power nets, with no LISN, and then compare the LISNs. This was done by changing the power net before the LISN, (because we do not have many chambers,) to understand whether the imbalanced LISN has reproducibility issues or not. Different power networks were created by adding a soldering iron, a linear DC power supply, different wires with terminations such as 2 nF, power cords, and strip lines to the outlet inside the chamber.

Changing the power net before the LISN should have no effect, as the LISN isolates well. With different termination impedances, the radiation should change if no LISN is used. However, it is expected to see a somewhat stable curve using either a balanced or an imbalanced LISN because both LISNs isolate the DUT from the power net. In addition, higher radiation is expected using an imbalanced LISN rather than by using a balanced LISN, since the imbalanced LISN converts differential-mode current into common-mode current.

Radiation results for all power networks and three different terminations e.g., balanced, imbalanced and no LISNs, are shown in Figure 27. When both power line communication devices are on, the broadband signal below 80 MHz is representative of the data transfer from the DUT (Figure 27). The DUT has no differential-mode energy above 80 MHz. Some observations are (a) without the LISN, the variation of the radiated emissions is up to 12 dB, since the termination is not controlled, (b) with a balanced or an imbalanced LISN, radiation has less than 3 dB variation, because the LISNs isolate the network and provide a well-defined termination, (c) the conversion with the imbalanced LISN is as high as 12 dB, and (d) both LISNs have no reproducibility issues.

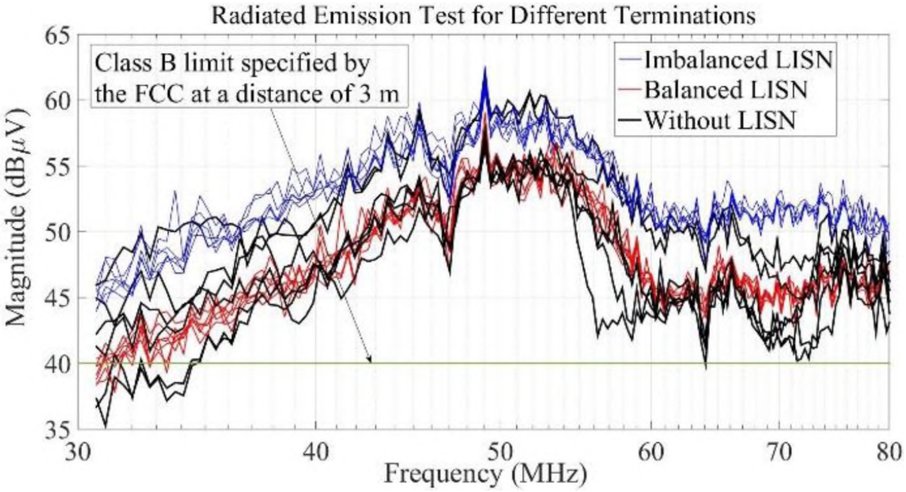

Figure 27. Measurement result of radiated emissions for power line communication devices using different terminations. The device has no DM mode energy above 80 MHz.

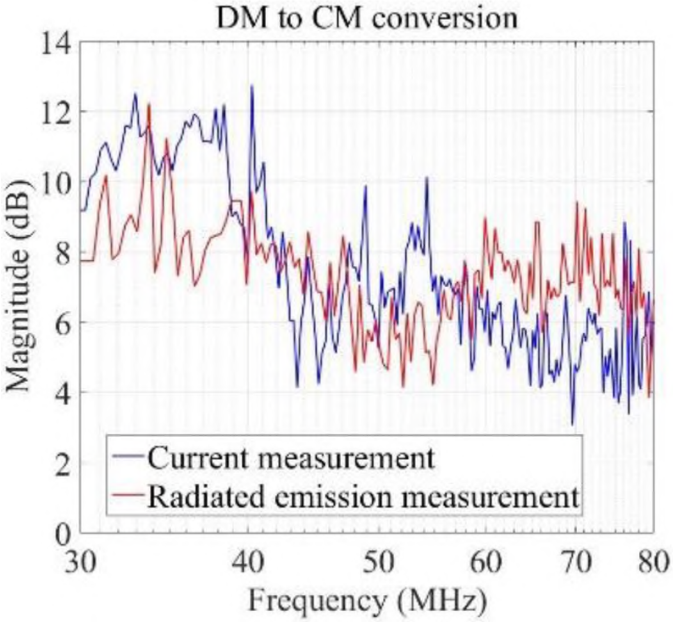

Figure 28. DM to CM conversion from current and radiated measurements. The device does not use the frequency above 80 MHz.

Neither impedance, nor conversion, has been characterized for the chamber used for measurement. Therefore, the observed variation in radiated emission is expected to be large (> 10 dB). However, both balanced and imbalanced LISNs have controlled terminations and will not cause reproducibility problems because the data has less than 3 dB variation for different power networks. In general, the data shows that for a device which has a strong differential-mode current, the imbalanced LISN brings the emissions to a more realistic level. However, the result from the balanced LISN is not realistic because it ignores the differential- to common-mode conversion and represents lower emission. The conversion of course should correlate to the currents on the wires. The common-mode and differential-mode currents have been measured with a F65 current clamp at a few points along the cables. The maximum current has been captured and the conversion was calculated as the difference between the maximum common-mode current when the cable was terminated with balanced and imbalanced LISNs. As shown in Figure 28, the conversion calculated from radiated emission and the common-mode current are quite similar. Above 80 MHz, the observed differences between the common-mode current for both balanced and imbalanced LISNs is almost zero because the DUT has no transmit energy. But for the lower frequency band, the conversion is as high as 12 dB for both radiated emission and common-mode current.

5. CONCLUSION

An analysis of an imbalanced two- or three-wire VHF LISN was conducted in terms of its mode conversion and termination impedance. It was demonstrated that an imbalanced termination impedance provides a specified degree of conversion from differential- to common-mode, which can lead to more representative radiated emission test results. For ensuring spectral emission control, an imbalanced LISN is needed. An imbalanced two or three-wire VHF LISN was prototyped. The deviation of the impedances from ideal in the imbalanced LISN was less than 10% error in magnitude and 30° in phase. A 3D full-wave simulation was performed to investigate the maximum radiation of the two- or three-wire set-ups with an imbalanced termination. It was demonstrated that the performance of the prototype leads to less than 3.5 dB error as compared to an ideal imbalanced LISN. In EMC applications, this error threshold is acceptable. Therefore, impedance variation with a limit of +/-30° in phase and +/-10% change in magnitude has been suggested to be considered for the new imbalanced VHF LISN. For the main cable termination, the standard compliance uncertainty has been considered in CISPR 16-4-1 to be 15.5 dB. This has been improved to about 9.5 dB for the proposed prototype. The differential- to common-mode conversion for an imbalanced termination was measured with two power line communication device to be as strong as 12 dB considering both current and radiated emissions. Using different power nets inside an anechoic chamber, it was demonstrated that the chamber to chamber reproducibility will be much better if an imbalanced LISN is used in every chamber.

REFERENCES

[1] K. Osabe, N. Kuwabara, S. Okuyama, “Termination Impedance for AC Mains Cable Leaving from EUT Area in Radiated Emission Measurement”, *International Symposium on Electromagnetic Compatibility*, pp. 1-6, Sep. 4-8, 2017.

[2] CISPR 35: *2016, Electromagnetic compatibility of multimedia equipment - Immunity requirements.*

[3] S. Okuyama, K. Osabe, N. Kuwabara, H. Muramatsu, "Influence of Disturbance Current Mode on Correlation between Radiation Test Sites Using VHF-LISN and CMAD," *International Symposium on Electromagnetic Compatibility*, Aug. 2018.

[4] C. Miyazaki, K. Tanakajima, M. Yamaguchi, "A Round-robin Test on Effectiveness of a VHF LISN for Radiated Emission measurements", *IEEE International Symposium on Electromagnetic Compatibility*, pp. 14-19, Aug. 2011.

[5] S. Okuyama, K. Osabe, K. Tanakajima, H. Muramatsu, "Investigation on Effectiveness of Very High Frequency Line Impedance Stabilization Network (VHF-LISN) for Measurement Reproducibility," *International Symposium on Electromagnetic Compatibility (EMC Europe 2013)*, Brugge, Belgium, Sep. 2-6, 2013.

[6] S. Okuyama, N. Kuwabara, M. Yamaguchi, K. Osabe "Improvement in the Reproducibility of Radiated Emission Measurements in a Fully Anechoic Room by Using VHF-LISN to Control the Termination Condition of the AC Mains Cable Leaving the EUT," *Asia-Pacific International Symposium on Electromagnetic Compatibility (APEMC)*, pp. 50-52, May 17-21, 2016.

[7] S. Okuyama, N. Kuwabara, K. Osabe, H. Muramatsu, "Improvement of Radiated Emission Measurement Reproducibility with VHF-LISN Obtained from Final Results of International Inter-laboratory Comparison on Termination Control of Power Line," *Asia-Pacific Symposium on Electromagnetic Compatibility* (APEMC), pp. 589-592, May 26-29, 2015.

[8] C. Miyazaki, K. Tanakajima, M. Yamaguchi, S. Satake, J. Kawano, "Improvement of Dispersion of Radiated Emission Measurement Results by VHF-LISN," *IEEE International Symposium on Electromagnetic Compatibility*, pp. 1-4, Aug. 18-22, 2008.

[9] Y. C. Tang, J. S. Chen, C. H. Lee, C. N. Chiu, "A Case Study on the Consistency Improvement in Radiated-Emission Testing by Using LISN," *International Symposium on Electromagnetic Compatibility*, Tokyo, pp. 259-262, May 12-16, 2014.

[10] CISPR/I/WG2, "Artificial Mains Networks for the boundary of the EMC test volume," *A supporting paper on CISPR/I/541/CD*, August 2017.

[11] D. M Lauder, R. C Marshall, "Measurement Uncertainty and Cable Balance-with Implications for the CDNE-M," *International Symposium on Electromagnetic Compatibility*, pp. 251-254, Sep. 2014.

[12] S. B. Worm, "On the relation between radiated and conducted RF emission tests", *International, Zurich Symposium & Technical Exhibition on EMC*, pp. 515-520, Feb. 16-18, 1999.

[13] M. Sørensen, O. Franek; S. K. Christensen; G. F. Pedersen; H. Ebert, "Assessment of the Usability of the Workbench Faraday Cage Method," *IEEE International Symposium on Electromagnetic Compatibility*, pp. 399-404, Aug. 14-19, 2011.

[14] Richard Thompson, "Comparing NPL measurements between OATS and GTEM with Worm," NPL, 25th July 2008. Informal circulation to interested parties.

[15] Available online at: https://www.keysight.com.

[16] CISPR/TR 16-1-2, Specifications for radio disturbance and immunity measuring apparatus and method.

[17] Available online at: https://www.cst.com.

[18] Available online at: https://www.cst.com/company/news/press-releases/agilent-technologies-and-cst-announce-integration-advances-for-rf-and-microwave-circuit-design.

[19] K. Osabe, N. Kuwabara, H. Muramatsu, "Impacts to Measurement Uncertainty of Radiated EMI Measurement by Setting Terminating Condition of AC Mains Cable Leaving from Test Area" *IEEE Asia-Pacific Symposium on Electromagnetic Compatibility (EMC/APEMC)*, 2018.

[20] CISPR/TR 16-4-1, Specifications for radio disturbance and immunity measuring apparatus and method- Part 4-1: Uncertainties, statistics, and limit modelling – Uncertainties in standardized EMC tests.

V. EFFECTS OF VARIABLE TERMINATION IMPEDANCE FOR RADIATED EMISSIONS

Hossein Rezaei

Department of Electrical Engineering
Missouri University of Science and Technology
Rolla, Missouri 65409–0050
Tel: 573–308–9313
Email: hrr7d@mst.edu

ABSTRACT

The common mode termination impedance seen by a cable between a DUT and a power connection in a semi-anechoic chamber will affect the radiated emissions at frequencies below 400 MHz. To simulate the radiated emissions as a function of the termination impedance, one can numerically solve each termination value in a full 3D simulation. However, this method is inefficient, because the actual geometry did not change, only the termination impedance. It is much more efficient to simulate the geometry using ports to obtain S-parameters, and then in a post processing add the termination impedance to observe the effect on the fields. Using this method, it is possible to perform the EM simulation only once and reproduce the radiated field for any termination while sweeping magnitude and phase.

For example, to investigate the design of an asymmetric very high frequency line impedance stabilization network (VHF LISN), the effects of variable complex impedance terminations on the radiated field emissions have been investigated. An asymmetric LISN reflects the impedances in a typical household better than a symmetric LISN. Using this

method, it was demonstrated that ± 30° change in phase and 10% change in magnitude of the termination impedance of an asymmetric VHF LISN does not have a significant effect (<4.7 dB) on radiated emission.

1. INTRODUCTION

Knowing that the termination of any load e.g., a line impedance stabilization network (LISN) or a versatile coupling/decoupling network of AC mains (CDNE-M) is not purely resistive over the working bandwidth and may have some magnitude and phase change [1 - 9]; one might argue that the change in phase or magnitude of complex termination might affect the radiation. Hence the radiation emission result can variate up to 15 dB from test lab to test lab [9].

It seems that the development of a new EMC standard has provided an opportunity to consider the effect of complex termination on test result. This has been done by prescribing the requirement of terminating condition and the tolerance level of termination in standard compliance uncertainty (SCU). "SCU parameter associated with the result of a compliance measurement as described in standard, that characterizes the dispersion of the values which could reasonably be attributed to the measurement." [10]. Therefore, SCU including the terminating condition of main cable is defined to be 15.5 dB in CISPR 16-4-1 [9, 10]. A three-wire VHF-LISN with impedance of 50 Ω on each line has also been used to calculate SCU including the terminating conditions [9]. To evaluate the uncertainty for cable termination of VHF-LISN, the tolerance for magnitude and the phase angle of three lines should be considered in the frequency range of 30 - 300 MHz. In [9], 729 combinations of three termination impedances with ±10 Ω variation in the magnitude and ± 25° variation in phase has been considered. This leads to enormous number of conditions for calculation. However, the number of calculations is reduced to 165 conditions due to symmetrical cable, it is still difficult to perform EM simulation even for 165 combinations of variable impedance [9]. Therefore, the tolerance of magnitude and phase angle for terminating impedance of three lines are specified in [9] only by using 99 combinations. Still, conditions were numerous, and one might argue that it takes a long time to repeat all these EM simulations. On the other hand, 99 discrete values have large "holes" in the Smith chart and, hence, missing worst case.

In this work, we use a different approach to investigate the tolerance of magnitude and phase angle for terminating impedance. In this approach, we perform EM simulation once, and reproduce radiated field for any termination, while sweeping magnitude and phase in a post processing step.

Having S-parameters matrices and transfer functions from a 3D full wave simulation, a post processing can be done to get the radiated field. The method is used to investigate the effects of variable complex terminated impedance over the ground plane on radiated field. Furthermore, this method is used to reduce the number of EM simulations and make a parametric sweep of the complex termination impedance. This allows to investigate the sensitivity of radiation behavior of test setup due to the deviation of magnitude and the phase in terminating impedance from ideal case.

The 3D full wave simulation was done with the finite integral technology solver in CST [11] and a MATLAB [12] code was written for post-processing step. Post-processing method allows to incorporate all passive complex impedances to be included in the 3D simulation as the termination in the real world are complex.

The rest of the paper is organized as follow. Post-processing method, formulation and simulation setup are constructed in Section 2. This is done with a one wire setup and two imbalanced setups with two and three wire terminations, which has been introduced recently by VCCI [13, 14]. Impact of termination condition on measurement uncertainty is discussed in Section 3. Results and discussion are provided in Section 4. A comparison between full wave simulation with ideal termination and post processing method is performed in this section to assess the accuracy of the method. Also, this section provides more analyses to study the effects of variable complex terminated impedance on radiated field. Section 5 concludes the paper.

2. CONSTRUCTION OF THE POST PROCESSING METHOD

To perform proper analyses on the effects of phase or magnitude changes on radiated emission, a simulation was done in CST. Figure 1 shows a 3D full wave simulation setup which was created to evaluate the radiated emission in accordance with the CISPR 22 standard [15]. This has been done to look at the change of radiated emission as a function of frequency for complex terminated impedance e.g., 10% change in magnitude and up to 30° phase change in termination. The simulation setup was created for one, two and three wires to perform full wave EM simulation once and make a parametric sweep of the complex termination impedance in a post processing step.

As shown in Figure 1, the setup uses a solid metal block to model the device under test (DUT) (30 x 10 x 30 cm) located 1 m above an infinite ground plane. Although this cable arrangement is not exactly similar to the suggested arrangement in CISPR 22 [15], but for the purpose of this work that does not matter.

The metal box is connected to 1.5 m long wires through different excitation e.g., common mode (CM) source with a 50 Ω port. A typical power cord geometry was used, each wire diameter is 1.62 mm. It is covered with a PVC insulation of 0.89 mm thickness. The distance between wires equals 2.35 mm. And the jacket has a diameter of 9.5 mm, also made from PVC.

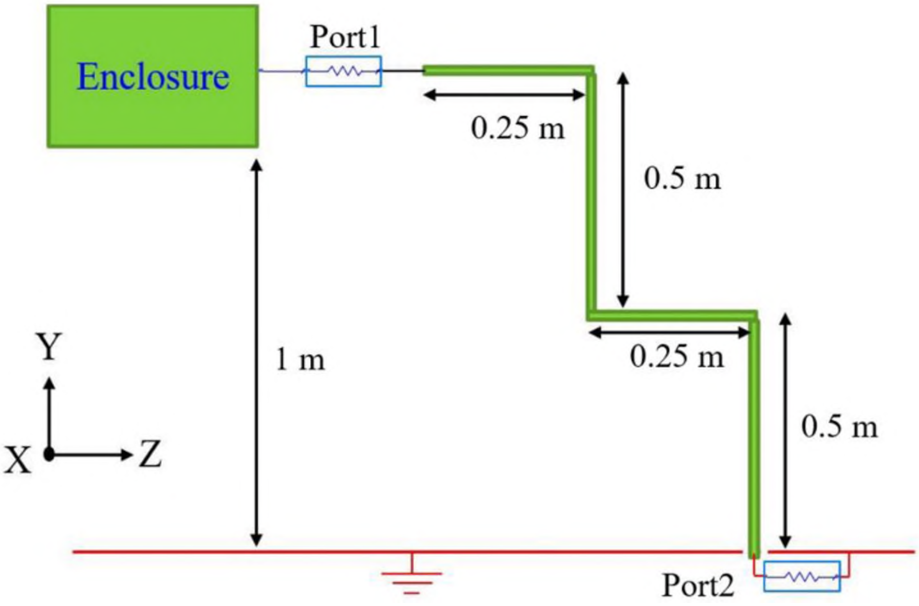

Figure 1. 3D full wave simulation setup for one wire application.

Looking at the schematic of the setup shown in Figure 1, it has two S-parameter sources to excite the structure from both sides of the wire. This structure is modeled as two ports network with the signal flow graph (SFG) shown in Figure 2. In this figure, port-one is the excitation source and port-two is the termination. The purpose of the SFG is to provide a solution algorithm by applying Mason's rule [16]. Mason's rule, also known as 'non-touching loop rule' is used to determine the ratio of a dependent (E) to an independent variable as:

$$E = T_1 + \frac{S_{21}\Gamma_L}{1 - S_{22}\Gamma_L} T_2, \tag{1}$$

The system is a 50 Ω system and hence the input reflection coefficient (Γ1) is zero in this SFG due to using S-parameter port at the input which is matched with 50 Ω.

From the termination point of view, any termination can be defined for these structures, e.g., symmetric two or three wire 50 Ω termination [1, 9]. However, in this work, the method is used to investigate the effects of variable complex impedance terminations on the radiated emissions for an imbalanced two or three wire termination (Figure 3) [13, 14].

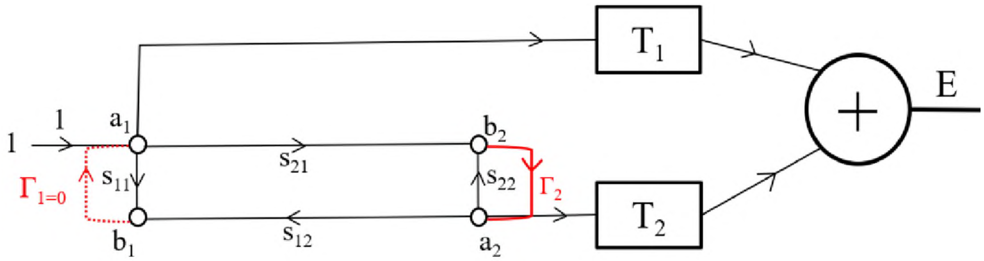

Figure 2. SFG for two port networks.

Although, the imbalanced termination has not been standardized yet, it is good to investigate the variation caused by a real termination impedance in an imbalanced termination. It has been shown that for some device e.g., power line communication model, the imbalanced design can increase radiation up to 15 dB because DM current converts into CM current [14]. For some device though e.g., LED there is no effect with an imbalanced termination [14]. Therefore, an imbalanced termination reflects the impedances in a typical household better than a symmetric one. Figure 4 shows the excitation and termination sides for two and three wire setups.

Figure 4.b and Figure 4.d show DM excitation for two and three wire setups, respectively. Some products have dominant CM on L and N in respect to PE. This is called TM excitation by VCCI (Figure 4.e).

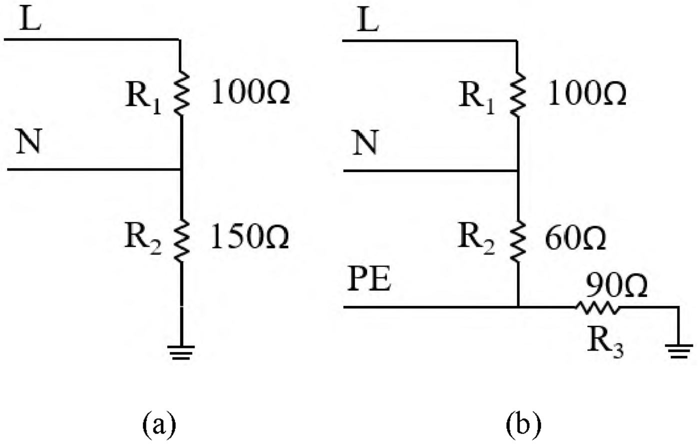

Figure 3. Schematic of an imbalanced termination, a) 2 wire termination, b) 3 wire termination.

Low connection impedance (10 Ω) is used in Figure 4. A low impedance was selected as this is similar to the voltage drop at an insufficiently connection. By comparing to a 1 Ω source it has been verified that the selection of the source impedance does not significantly influence the conclusions drawn from the simulation.

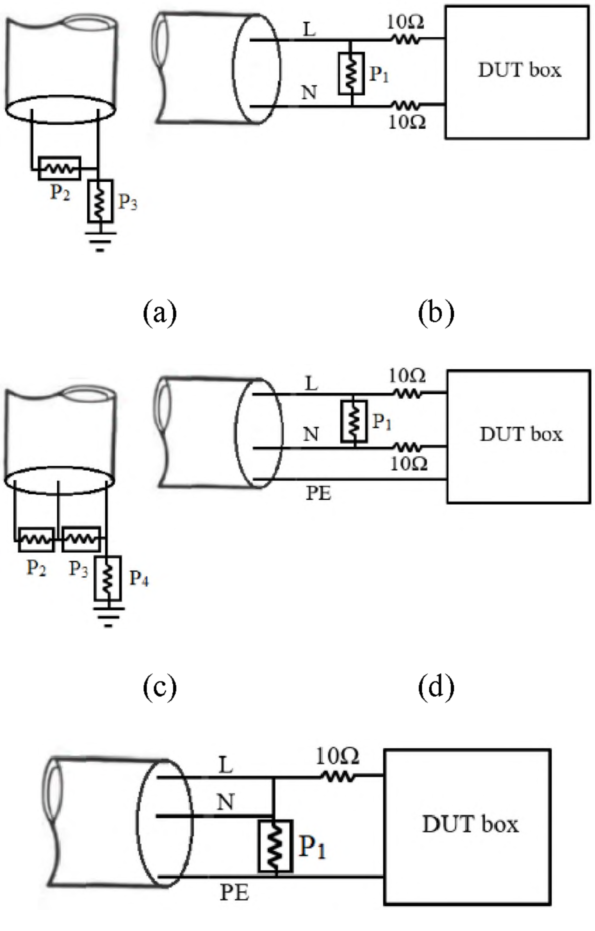

(a) (b)

(c) (d)

(e)

Figure 4. Schematic used in 3D full wave simulation setup, a) two wire imbalanced termination, b) DM excitation for two wire application, c) three wire imbalanced termination, d) DM excitation for three wire application, e) TM excitation for three wire application.

Looking at the schematic of the two and three wire setups shown in Figure 4, they have three and four S-parameter sources, respectively. All ports excite the structure from both sides of the wire to get the transfer functions (T). The transfer function is the maximum radiated emission in 3 m distance for each S-parameter excitation. The first structure (three ports in Figure 4.a and Figure 4.b) is modeled as three ports network with the SFG shown in Figure 5. The second structure (four ports in Figure 4.c, with either

Figure 4.d or Figure 4.e) is modeled as four port networks with the SFG shown in Figure 6. It is obvious that port-one is replaced with voltage source (a port with 50 Ω) in both networks. Thus, the input reflection coefficient (Γ1) is zero due to using 50 Ω S-parameter port at the input which is matched with 50 Ω. The rest of the ports in Figure 5 and Figure 6 are replaced with two or three wire imbalanced terminations (Figure 3) and the reflection coefficients will be calculated for each impedance.

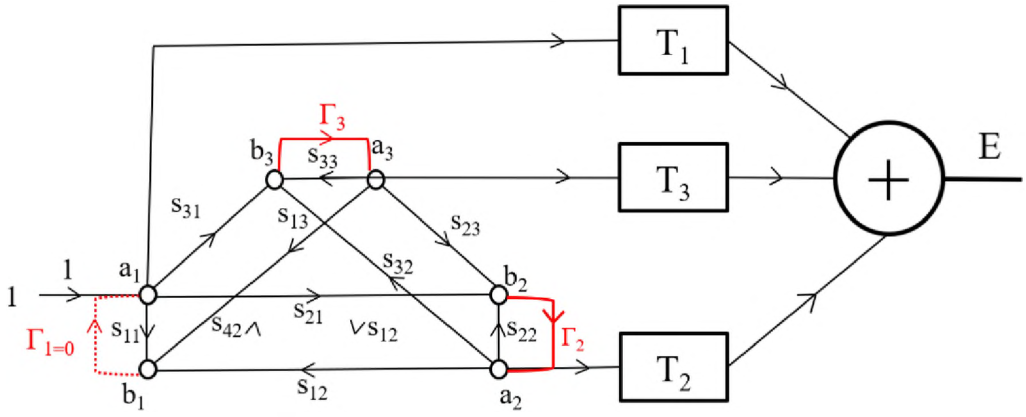

Figure 5. SFG for three port networks.

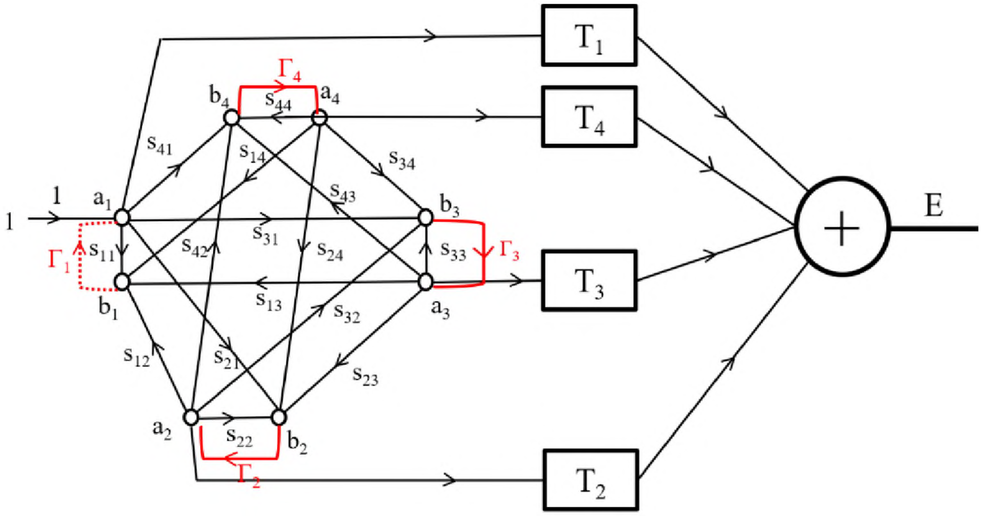

Figure 6. SFG for four port networks.

To find relations and provide a solution algorithm, Mason's rule is applied in Figure 5 and the ratio of a dependent (E) to an independent variable calculated as:

$$\begin{aligned} E &= T_1 + \\ &+ \frac{(1 - S_{33}\Gamma_3)S_{21}\Gamma_2 + S_{31}S_{23}\Gamma_2\Gamma_3}{1 - S_{22}\Gamma_2 - S_{33}\Gamma_3 - S_{23}S_{32}\Gamma_2\Gamma_3 + S_{22}S_{33}\Gamma_2\Gamma_3}T_2 \\ &+ \frac{(1 - S_{22}\Gamma_2)S_{31}\Gamma_3 + S_{21}S_{32}\Gamma_2\Gamma_3}{1 - S_{22}\Gamma_2 - S_{33}\Gamma_3 - S_{23}S_{32}\Gamma_2\Gamma_3 + S_{22}S_{33}\Gamma_2\Gamma_3}T_3, \end{aligned} \tag{2}$$

where E is the maximum radiated field in 3 m distance, $\Gamma2$ and $\Gamma3$ are reflection coefficient related to R1 and R2 in Figure 3.a, respectively. And T1, T2 and T3 are the maximum radiated emission correspond to three individual S-parameter port excitations in full wave solver. Similarly, by applying Mason's rule in three-wire setup (Figure 6), the ratio of a dependent (E) to an independent variable can be shown as:

$$E = T_1 + \frac{F_2}{D}T_2 + \frac{F_3}{D}T_3 + \frac{F_4}{D}T_4, \tag{3}$$

where $D = 1 - (S22\Gamma2 + S33\Gamma3 + S44\Gamma4 + S23S32\Gamma2\Gamma3 + S24S42\Gamma2\Gamma4 + S34S43\Gamma3\Gamma4 + S23S34S42\Gamma2\Gamma3\Gamma4 + S32S43S24\Gamma2\Gamma3\Gamma4) + S22S33\Gamma2\Gamma3 + S22S44\Gamma2\Gamma4 + S33S44\Gamma3\Gamma4 + S43S34S22\Gamma2\Gamma3\Gamma4 + S42S24S33\Gamma2\Gamma3\Gamma4 + S32S23S44\Gamma2\Gamma3\Gamma4 - \Gamma2\Gamma3\Gamma4S22S33S44$,

$F2 = (1 - S33\Gamma3 - S44\Gamma4 - S34S43\Gamma3\Gamma4 + S33S44\Gamma3\Gamma4)S21\Gamma2 + S31S23\Gamma2\Gamma3(1-S44\Gamma4) + S41S24\Gamma2\Gamma4 (1-S33\Gamma3) + S41S34S23\Gamma2\Gamma3\Gamma4 + S31S43S24\Gamma2\Gamma3\Gamma4$,

$F3 = (1 - S22\Gamma2 - S44\Gamma4 - S24S42\Gamma2\Gamma4 + S22S44\Gamma2\Gamma4)S31\Gamma3 + S21S32\Gamma2\Gamma3(1-S44\Gamma4) + S41S34\Gamma3\Gamma4(1-S22\Gamma2) + S41S24S32\Gamma2\Gamma3\Gamma4 + S21S42S34\Gamma2\Gamma3\Gamma4$,

$F4 = (1 - S22\Gamma2 - S33\Gamma3 - S23S32\Gamma2\Gamma3 + S22S33\Gamma2\Gamma3)S41\Gamma4 + S21S42\Gamma2\Gamma4(1-S33\Gamma3) + S31S43\Gamma3\Gamma4(1-S22\Gamma2) + S21S43S32\Gamma2\Gamma3\Gamma4 + S31S23S42\Gamma2\Gamma3\Gamma4$.

where E is the maximum radiated field in 3 m distance, Γ2, Γ3 and Γ4 are reflection coefficient related to R1, R2 and R3 in Figure 3.b, respectively. And T1, T2, T3 and T4 are the maximum radiated emission correspond to four individual S-parameter port excitations in full wave simulation.

3. IMPACT OF TERMINATION CONDITION ON MEASUREMENT UNCERTAINTY

The sensitivity of radiation behavior of test setup due to the deviation of magnitude and the phase in terminating impedance from ideal case is considered in CISPR 16-4-1 standard [10]. The average combined standard uncertainty (Uc-scu) is defined (including the terminating condition of main cable) as [9]:

$$U_{c-scu} = \sqrt{U_{c-MIU}^2 + U_a^2 + U_b^2 + U_c^2} \tag{4}$$

where CISPR/TR 16-4-1 specifies [9, 10]:

- Combined Measurement Instrumentation Uncertainty (Uc-MIU) of 2.5 dB,
- uncertainty by main cable arrangement (Ua) of 3.5 dB,
- uncertainty in operating condition of EUT (Uc) of 1.7 dB.
- and the uncertainty in terminating condition (U_b).

Having a rectangular probability distribution for the uncertainty of cable terminating condition which is already considered in CISPR 16-4-1 [10], the uncertainty in terminating condition (U_b) is defined as [9]:

$$U_b = \frac{E_{max} - E_{min}}{2\sqrt{3}} = \frac{\Delta E}{2\sqrt{3}} \tag{5}$$

where Emax and Emin are the maximum and minimum electric field strength in dBµV/m, respectively. From CISPR 16-4-1 [9], the expanded standard uncertainty (USCU,VHF-LISN) is obtained :

$$U_{scu,\,VHF-LISN} = 2U_{c-scu} \tag{6}$$

4. RESULTS AND DISCUSSION

To verify the method, two simulations were performed in a full wave solver for each setup namely one, two and three wire setups. First, all three setups were simulated with pure resistive lumped element in termination sides. Field monitors were used to get the radiated emission at different frequencies in full wave simulation (CST design studio). Using these results, the maximum radiation is calculated in a post processing step; however, it is also possible to let CST calculates the maximum radiation with post processing option. This result will be used as references to evaluate the post processing method. Second, all S-parameter ports have been excited in full wave solver to get the transfer functions i.e., T1 – T4 (Figure 2. Figure 5 and Figure 6). Considering SFG shown in Figure 2, 5, and 6, reflection coefficient for each port can be calculated with equivalent terminations as used in step one. As an example, the reflection coefficient and electric field for ideal termination in one-wire setup can be calculated with (7) and (8), respectively:

$$\Gamma_L = \frac{Z_L - 50}{Z_L + 50}_{Z_L=150\,\Omega} = 0.5 \tag{7}$$

$$E = T_1 + \frac{0.5 * S_{21}}{1 - 0.5 * S_{22}} T_2, \tag{8}$$

The equivalent reflection coefficient can be calculated in a same way with each termination mentioned in two or three- wire setup (Figure 5 and Figure 6). The maximum radiation then is calculated in a post processing step using (1), (2) and (3) for three different setups.

After verifying the method, it is used to determine the effects of change in the phase and magnitude of termination on radiation. This can be performed easily by updating the reflection coefficients for any arbitrary termination.

It is worth mentioning that from this point onwards, no full wave simulations are required for the analyses on different setups. It is possible to reproduce radiated field for any arbitrary termination, while sweeping magnitude and phase of termination without performing new full wave simulation. This will be done just by defining different reflection coefficient for different ports.

4.1. ONE WIRE SETUP

The analysis for one wire setup is performed with the setup shown in Figure 1 which is terminated to ground plane with a series RLC combination (R = 135 Ω, L = 10 nH, and C = 70 pF). The comparison between the results of full wave simulation and post processing method has less than 0.6 dB difference in 0-1000 MHz (Figure 7). This comparison shows a good agreement between two methods and verifies that the postprocessing step reproduce the result from 3D full wave simulation very well. After the initial verification of the method, it will be used to quantify the effects of termination sweep on radiated emission.

Although allowable deviation for common mode impedance termination of 150 Ω is reported [1, 17] and is qualitatively known; it is important to quantify the effect of the real termination with non-zero phase (+/-10% change in magnitude and +/-30° phase change). The effects of allowable deviation on radiated emission can be used to illustrate the usefulness of the proposed variation.

To sweep the termination impedance, a random function is used since both emission (8) and reflection coefficient (7) are non-linearly related to the parameters of the terminations. To perform a random sweep of impedance, the magnitude of the termination impedance is defined as random variables as:

$$X_i = X_i^{min} + \left(X_i^{max} - X_i^{min}\right) \times rand(1, N) \tag{9}$$

where the parameter X_i=unif(X_i^{min}, X_i^{max}) is the uniformly distributed random number on the interval (X_i^{min}, X_i^{max}). Therefore, 10% change in magnitude is the limit specified for the terminated impedance. Total combinations of 2000 terminations with random distribution has been selected. Similarly, the phase of the termination impedance is defined as random variables as:

$$Y_i = Y_i^{min} + \left(Y_i^{max} - Y_i^{min}\right) \times rand(1, N) \tag{10}$$

where the parameter Y_i=unif(Y_i^{min}, Y_i^{max}) is the uniformly distributed random number on the interval (Y_i^{min}, Y_i^{max}). Thus, ±30° in phase are the limit specified for the terminated impedance. Total combinations of 2000 terminations with random distribution has been selected. Therefore, the impedance is calculated as:

$$Z_i = X_i e^{j\frac{\pi}{180}Y_i} \tag{11}$$

Reflection coefficient of each sample has been calculated with (7). The results are plotted in Figure 8 as red stars represent the reflection coefficients.

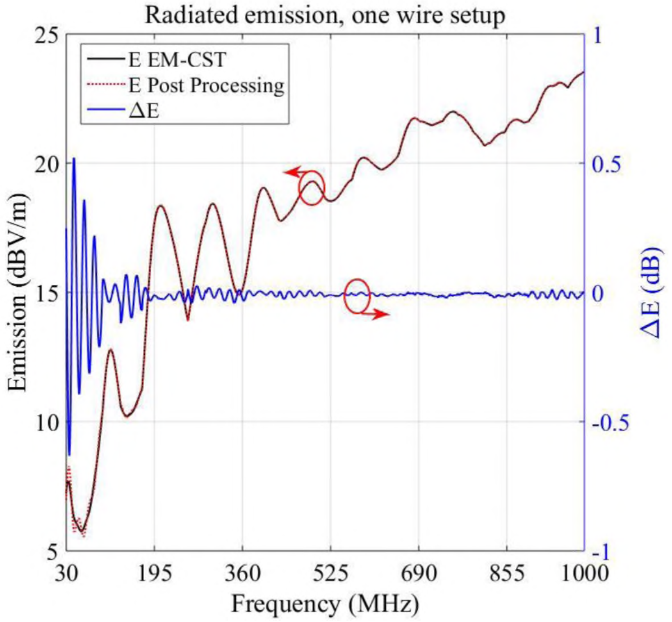

Figure 7. Radiated emission (E field) with ideal termination (1-wire setup).

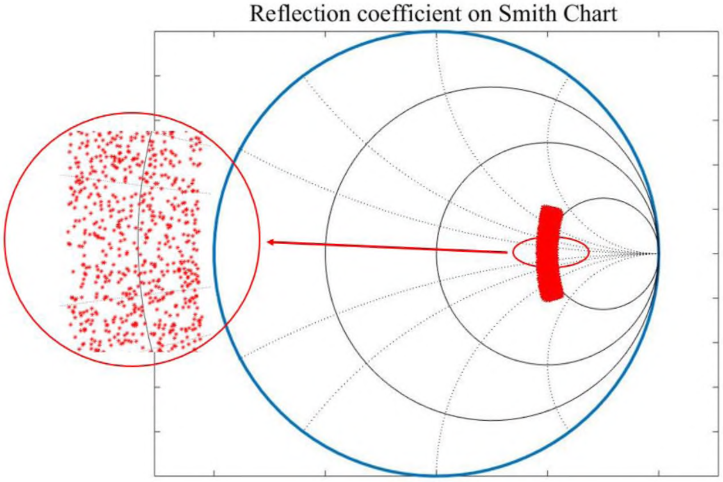

Figure 8. Reflection coefficient on smith chart (1-wire setup).

After calculating transfer function from a full wave simulation, the post processing is performed for 2000 test cases to calculated radiated emission for each case. This calculation last only about 40 minutes in MATLAB.

Considering the fact that one full wave simulation cannot be faster than 3 hours for one wire setup, post processing method is much faster than full wave simulation. Radiated emission for all combinations is shown in Figure 9 and are compared with the radiation from ideal termination. Figure 10 shows the deviation of radiated emission from ideal (RCM = 150 Ω). Because, the main source of the radiation is main cable, the field is affected by the cable length. It resonates and drops, periodically. The calculated value uniformly distributed for different terminations between the maximum and minimum value of each frequency.

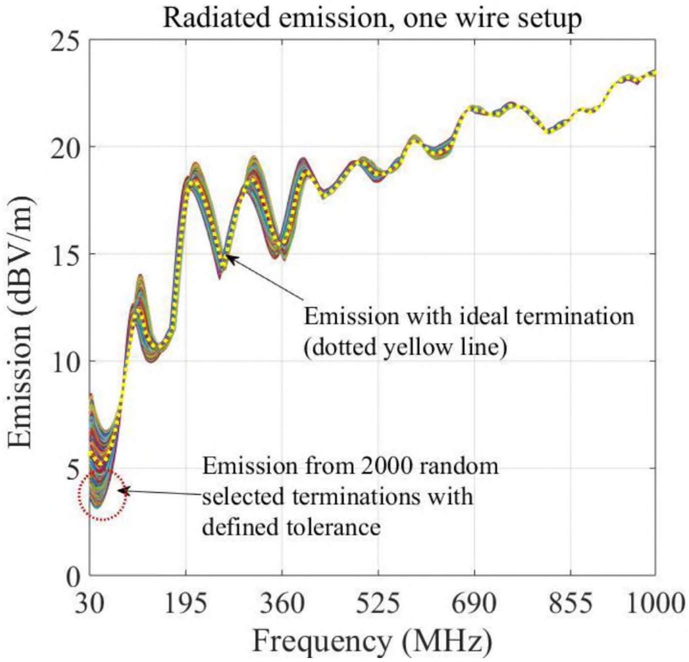

Figure 9. Radiated emission with different terminations (1-wire setup).

It can be seen that the maximum radiated fields for all random selected terminations at f = 35 and 200 MHz, is about 2.5 and 2 dB, respectively. However, at 400 MHz, the difference is only 1.5 dB. These results indicate that the termination has largest effect at lower frequencies (below 400 MHz). For the frequencies above 400 MHz, however, the wavelength is comparable with the length of the cable. The radiation is dominant at the source region and it does not depend on the termination, anymore. As can be seen in Figure 10, the maximum radiation with the tolerance specified in one wire setup is only 2.8 dB occurs around 35 MHz. This of course validate the proposed variation because the tolerance specification has negligible effects (< 3 dB) on emission.

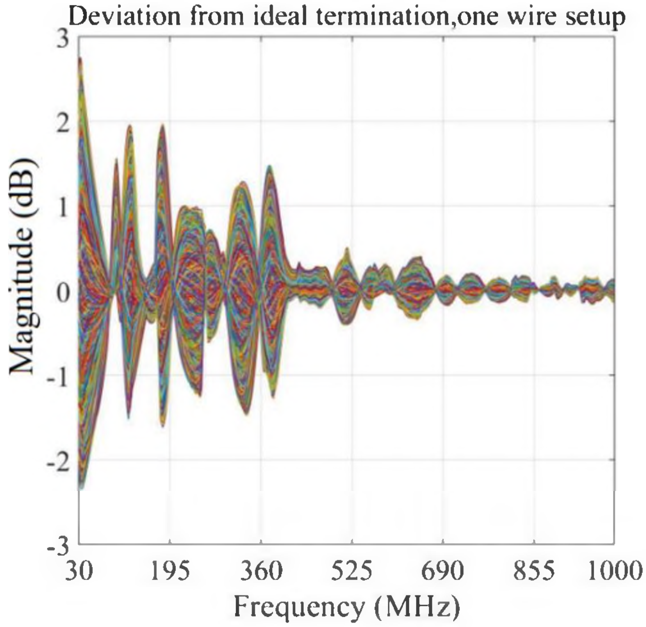

Figure 10. Maximum change in radiated emission due to different terminations (1-wire setup).

Figure 11 shows the normalized radiation for different frequencies on smith chart. The radiated field has been calculated for all possible terminations on different frequencies, e.g., 30, 100, 200 and 400 MHz on smith chart. The difference between the maxima and minima of radiated field for all possible termination on smith chart is about 35 and 11 dB, at the frequencies 45 and 200 MHz, respectively. However, at 400 MHz, the difference is only 4 dB. As the frequency increases, the radiation has less variation. The maximum radiation is found with Re(Z) = 0 Ω or Re(Z) = inf where $|\Gamma| = 1$; however, at different angles, it depends on the frequency. Because of resonance in the associated main cable, the radiated emission is varying with frequency.

As the test condition defines this resonance, it is not representative of real-life installation. An average common mode impedance of a long cable has been justified to be 150 Ω to minimize the effects of resonance upon measurement reproducibility [18, 19]. Figure 9 shows no strong resonances around Z = 150 Ω ± 15 Ω with ± 30 ° phase for a long cable. Therefore, post processing method can easily prove justification of 150 Ω as average common mode impedance which arises from empirical data [20].

4.2. TWO-WIRE SETUP

The analysis for two-wire setup is performed with imbalanced two wire termination (Figure 4.a). To verify the method with a realistic termination, a series RLC combination has been used which provides up to 10 % change in magnitude and up to 40° phase change, e.g., $R_{DM} = 90\ \Omega$, L = 10 nH, C = 70 pF and $R_{CM} = 135\ \Omega$, L = 10 nH, C = 70 pF.

The comparison between the results of full wave simulation and post processing method has less than 0.7 dB difference in 30-300 MHz (Figure 11). Good agreement between two methods verifies that the postprocessing step reproduce the result from 3D full wave simulation very well. After the initial verification of the post processing method, it will be used to quantify the effects of termination sweep on radiated emission in imbalanced two wire setup.

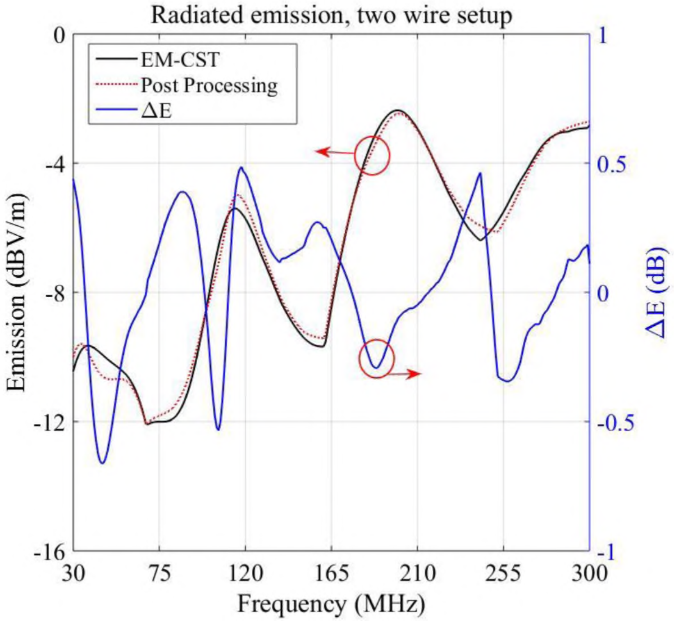

Figure 11. Radiated emission (E field) with ideal termination (2-wire setup).

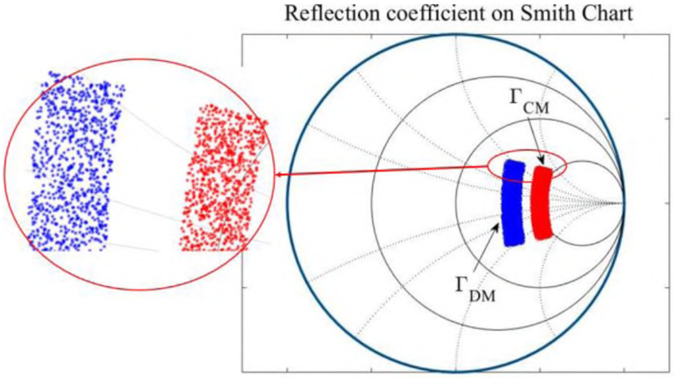

Figure 12. Reflection coefficient on smith chart (two-wire setup).

An independent random sweep of two impedances is performed. Having the tolerance specified with 10% deviation in magnitude and +/-30° in phase of two termination impedances namely, CM and DM impedances, the 2000 combinations of random selected impedances is shown on smith chart (Figure 12).

Calculating transfer function from a full wave simulation, the post processing is performed for 2000 test cases. The process lasts only about 50 minutes which is quite fast compare to 4 hours performing only one full wave simulation.

Radiated emissions for all combinations is compared with emission from ideal termination (Figure 13).

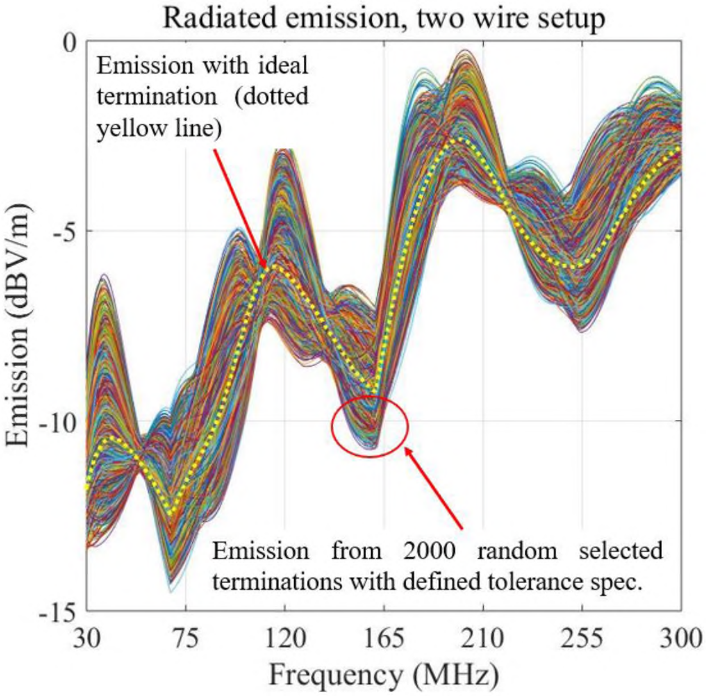

Figure 13. Radiated emission (E field) with different terminations (two-wire setup with DM excitation).

The maximum error with the tolerance specified in two-wire setup is about 4 dB. The maximum deviation occurs around 40 MHz. This is expected because the termination is more important at lower frequencies.

4.3. THREE-WIRE SETUP

The analysis for three-wire setup is performed with imbalanced three wire termination (Figure 4.c). This has been done with DM excitation (Figure 4.d) and TM excitation (Figure 4.e).

To verify the method, a series RLC combination has been used to provide a realistic termination with up to 10 % change in magnitude and up to 40° phase change: R_{DM} = 90 Ω, L = 10nH, C = 90 pF, RTM = 50 Ω, L = 10nH, C = 117 pF and R_{CM} = 80 Ω, L = 10nH, C = 90 pF.

Comparing the results of full wave simulation and post processing method, the error is less than 0.7 dB and 1.9 dB for DM (Figure 14) and TM excitation (Figure 15), respectively.

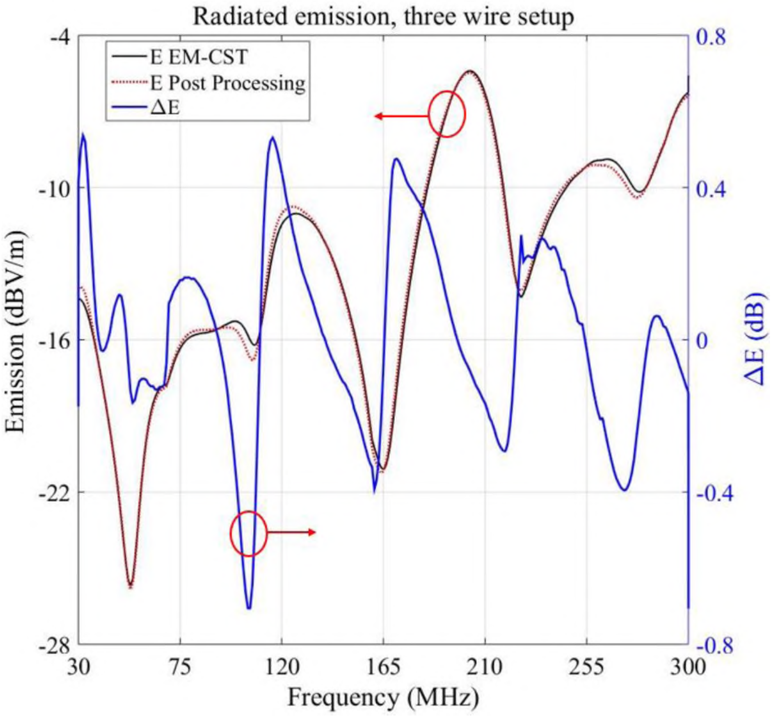

Figure 14. Radiated emission for three-wire setup with DM excitation.

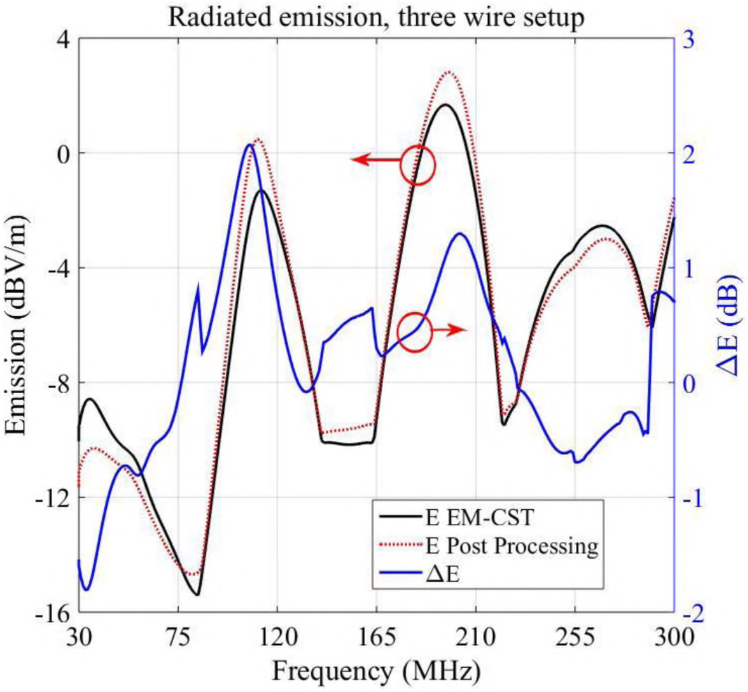

Figure 15. Radiated emission for three-wire setup with TM excitation.

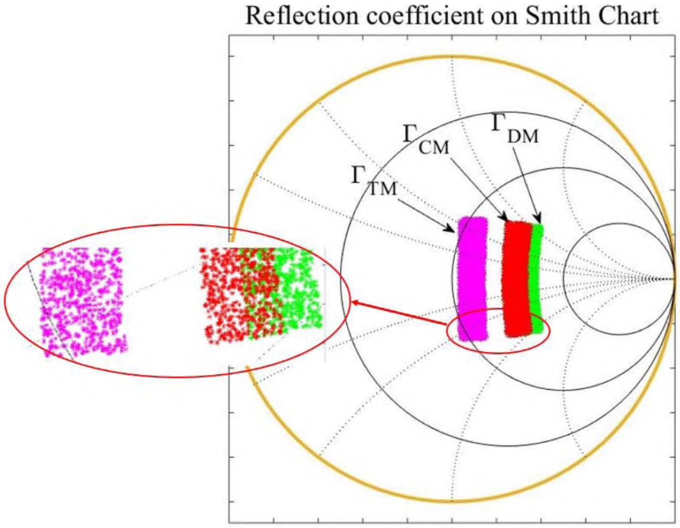

Figure 16. Reflection coefficient on smith chart (three-wire setup).

To quantify the effects of termination-sweep on radiated emission in three-wire setup, a random distribution of three impedances is used. Similarly, the tolerance in random distribution is defined as to be 10% in magnitude and +/-30° in phase of each individual impedance. Furthermore, 2000 combinations of reflection coefficient of independently random selected impedances with defined tolerance e.g., DM, CM and TM impedances are used (Figure 16). After calculating transfer function from a full wave simulation, the post processing method is performed for 2000 test cases.

This last only about 2.5 hours which is much faster compare to 5 hours to do only one full wave simulation. Figure 17 shows the radiated emissions of all combinations with DM excitation. Difference between the maximum radiation and the ideal case (dotted yellow line) is less than 4.7 dB. Emission with TM excitation is shown in Figure 18. The radiated emission from all combinations undulates around the reference emission with maximum 3 dB difference.

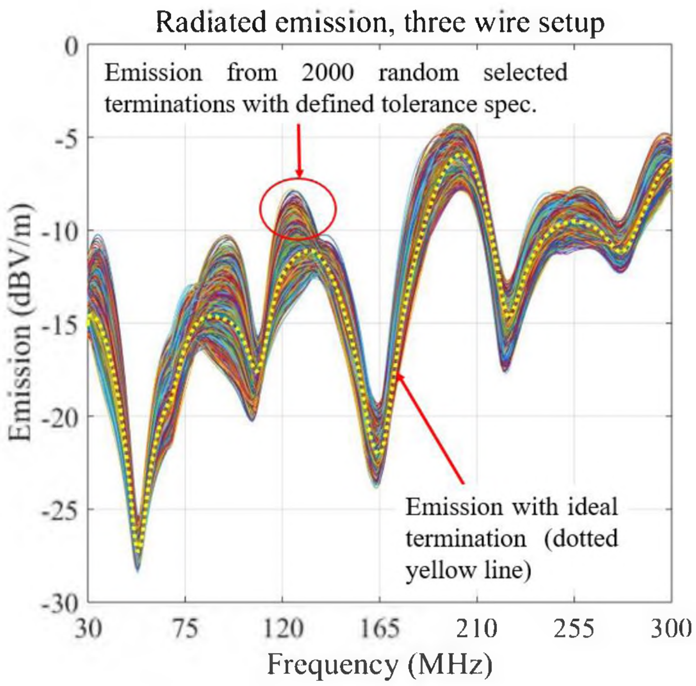

Figure 17. Radiated emission (E field) with different terminations (three-wire setup with DM excitation).

4.4. IMPACT OF TERMINATION CONDITION ON MEASUREMENT UNCERTAINTY

Figure 19 shows the maximum deviation of radiated emissions with DM and TM excitations among all combinations of terminated impedance in two and three wire setups. The maximum change in emission among all test cases with defined tolerance is less than 5 dB. The maximum deviation occurs around 177 MHz in three-wire setup with DM excitation. This is about 8 dB lower than previously reported for a balanced three-wire termination [9]. The PE is connected to the enclosure in a balanced termination; thus, the common mode impedance is low for all currents. The imbalanced three-wire termination is different, though. So, it may suppress resonances stronger, as PE is not grounded. Because the maximum deviation due to termination condition of the imbalanced two and three-wire setups from 30 up to 300 MHz is about 5 dB, the maximum uncertainty in terminating condition (Ub) in (5) is only about 1.6 dB. Using (4), the average combined standard uncertainty (Uc-scu) for two and three wires would be about 5 dB. The expanded standard uncertainty (USCU,VHF-LISN) in (6) is improved to 10 dB for imbalanced two or three-wire termination. This has been reported to be USCU,VHF-LISN =12 dB for 50 Ω LISN in [9]. Comparing with 15.5 dB currently defined in CISPR 16-4-1 [10], SCU for imbalanced two or three-wire VHF LISN is improved about 5.5 dB.

5. DISCUSSION

A post processing method was implemented to investigate the effects of complex termination on radiated emission. This method was used to reduce the number of full wave simulations and make a parametric sweep of the complex termination impedance.

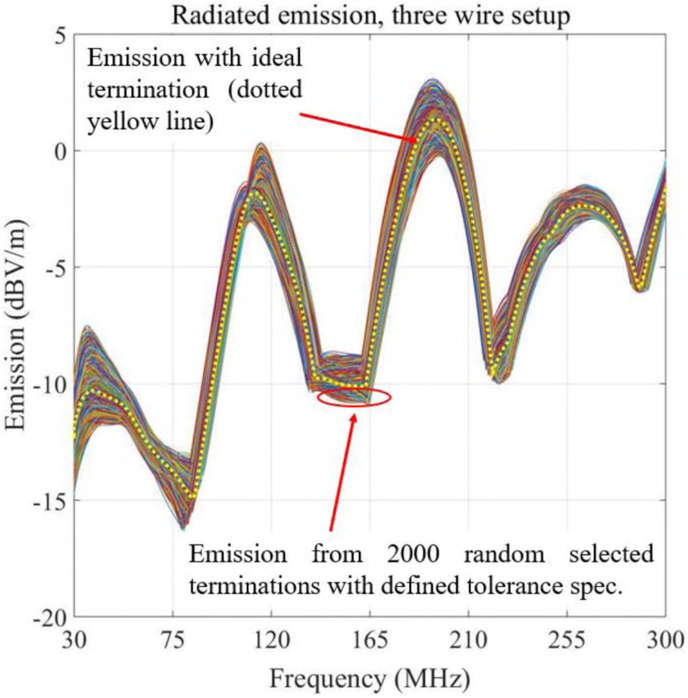

Figure 18. Radiated emission (E field) with different terminations (three-wire setup with TM excitation).

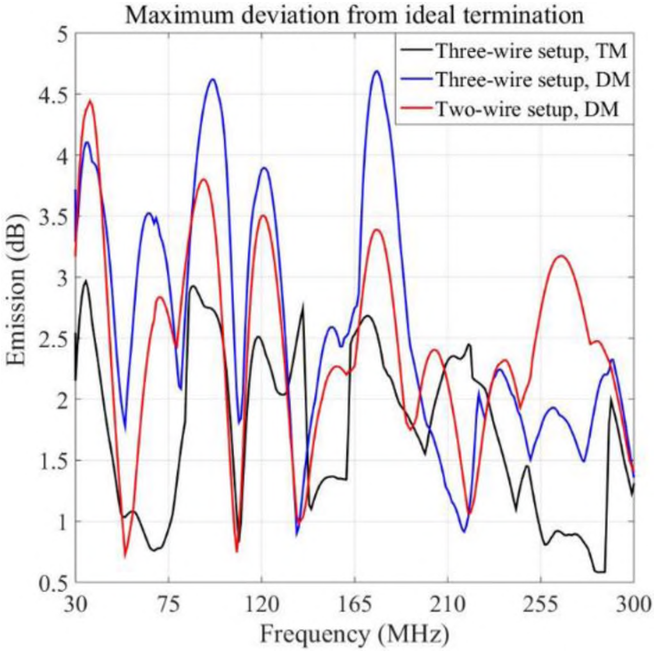

Figure 19. Maximum change in radiated emission (E field) due to different terminations (two and three-wire setup).

The method implemented under assumption that the maximum radiated emission is a function of S-parameters and reflection coefficients. However, the standing wave on the wire might be changed with termination and probably cause a different radiation pattern. For the purpose of this work, the radiation pattern is considered to be independent of reflections, i.e., the position of nodes and anti-nodes.

Therefore, it is possible to perform full wave simulation once to calculate the transfer functions and reproduce radiated field for any complex termination. Post processing part performed with a simple code in MATLAB. The method provides an opportunity to consider the effect of complex termination on test result without needing to repeat full wave simulation or measurement. It seems that this method prepares an easy approach to consider the effect of complex termination on test result.

Three different setups e.g., one wire, imbalanced two or three-wire setups, were used to investigate the effect of allowable deviation from standard terminations on radiation emissions.

The results from post processing method were verified with full wave simulation for all three different setups, first. It was shown that the computational error with post processing method is less than 1 dB. Then, it was shown that:

Radiated emission of 2000 independently random selected terminations with allowable deviation took only about 40, 50 and 160 minutes for one, two and three wire setups, respectively. This of course is much faster comparing to required 2000 times full wave simulations because each one, two and three wire full wave simulation may last about 3, 4 and 5 hours, respectively.

Termination has largest impact at lower frequencies (below 400 MHz) and the termination is less important above 400 MHz as the wavelength becomes comparable with the length of the cable. Thus, the radiation is dominant at the source region and it does not depend on the termination.

With 10% change in the magnitude of terminated impedance and ±30° change in its phase, no significant (less than 5 dB) effect on radiation was observed.

The calculated radiated emission uniformly distributed for different terminations between the maximum and minimum value of each frequency.

6. CONCLUSION

A post processing method was implemented to investigate the effects of complex termination on radiated emission. Post processing part performed with a simple code in MATLAB. The method provides an opportunity to consider the effect of complex termination on test result without needing to repeat full wave simulation or measurement.

The results from post processing method were verified with full wave simulation for three different setups e.g., one wire, imbalanced two or three-wire setups, first. It was shown that the computational error with post processing method is less than 1 dB.

Using this method, the uncertainty based on the tolerance of terminating impedance is calculated to be about 5 dB for two or three-wire setup. Including termination condition for two or three-wire setup, the SCU was calculated to be about 10 dB. This is about 5.5 dB lower than 15.5 dB which is currently defined in CISPR 16-4-1.

REFERENCES

[1] S. Okuyama, N. Kuwabara, K. Osabe, H. Muramatsu, “Improvement of Radiated Emission Measurement Reproducibility with VHF-LISN Obtained from Final Results of International Inter-laboratory Comparison on Termination Control of Power Line,” *Asia-Pacific Symposium on Electromagnetic Compatibility (APEMC)*, pp. 589-592, May 26-29, 2015.

[2] C. Miyazaki, K. Tanakajima, M. Yamaguchi, S. Satake, J. Kawano, “Improvement of Dispersion of Radiated Emission Measurement Results by VHF-LISN,” *IEEE International Symposium on Electromagnetic Compatibility*, pp. 1-4, Aug. 18-22, 2008.

[3] S. Okuyama, K. Osabe, N. Kuwabara, H. Muramatsu, “Influence of Disturbance Current Mode on Correlation between Radiation Test Sites Using VHF-LISN and CMAD,” *International Symposium on Electromagnetic Compatibility (EMC Europe 2018)*, Amsterdam, The Netherlands, Aug. 27-30, 2018.

[4] C. Miyazaki, K. Tanakajima, M. Yamaguchi, “A Round-robin Test on Effectiveness of a VHF LISN for Radiated Emission measurements”, *IEEE International Symposium on Electromagnetic Compatibility*, pp. 14-19, Aug. 2011.

[5] S. Okuyama, K. Osabe, K. Tanakajima, H. Muramatsu, “Investigation on Effectiveness of Very High Frequency Line Impedance Stabilization Network (VHF-LISN) for Measurement Reproducibility,” *International Symposium on Electromagnetic Compatibility (EMC Europe 2013)*, Brugge, Belgium, Sep. 2-6, 2013.

[6] S. Okuyama, N. Kuwabara, M. Yamaguchi, K. Osabe “Improvement in the Reproducibility of Radiated Emission Measurements in a Fully Anechoic Room by Using VHF-LISN to Control the Termination Condition of the AC Mains Cable Leaving the EUT,” *Asia-Pacific International Symposium on Electromagnetic Compatibility (APEMC)*, pp. 50-52, May 17-21, 2016.

[7] Y. C. Tang, J. S. Chen, C. H. Lee, C. N. Chiu, “A Case Study on the Consistency Improvement in Radiated-Emission Testing by Using LISN,” *International Symposium on Electromagnetic Compatibility*, pp. 259-262, May 12-16, 2014.

[8] K. Osabe, N. Kuwabara, S. Okuyama, “Termination Impedance for AC Mains Cable Leaving from EUT Area in Radiated Emission Measurement,” International *Symposium on Electromagnetic Compatibility - EMC EUROPE*, Angers, France, pp. 1-6, Sep. 4-8, 2017.

[9] K. Osabe, N. Kuwabara, H. Muramatsu, “Impacts to Measurement Uncertainty of Radiated EMI Measurement by Setting Terminating Condition of AC Mains Cable Leaving from Test Area” *IEEE International Symposium on Electromagnetic Compatibility*, pp. 52-56, May 14-18, 2018.

[10] CISPR/TR 16-4-1, Edition 2.0, Specifications for radio disturbance and immunity measuring apparatus and method- Part 4-1: Uncertainties, statistics, and limit modelling – Uncertainties in standardized EMC tests.

[11] Available online at: https://www.cst.com.

[12] Available online at: https://www.matlab.com.

[13] CISPR/I/WG2, “Artificial Mains Networks for the boundary of the EMC test volume,” *A supporting paper on CISPR/I/541/CD*, August 2017.

[14] D. M Lauder, R. C Marshall, “Measurement Uncertainty and Cable Balance-with Implications for the CDNE-M and CMAD,” *International Symposium on Electromagnetic Compatibility*, pp. 801-806, Sep. 2014.

[15] “CISPR 22”, Information technology equipment -Radio disturbance characteristics- Limits and methods of measurement, Edition 5.2, 2006-03.

[16] S.J. Mason, Feedback theory – Some properties of signal flow graphs, Proc. IRE 41 (1953) 1144–1156.

[17] CISPR 16-1-2 Edition 1.2, Table 7.2 “Characteristics of the asymmetric artificial network”.

[18] S. B. Worm, “On the relation between radiated and conducted RF emission tests”, *13th International, Zurich Symposium & Technical Exhibition on EMC*, pp. 515-520, Feb. 16-18, 1999.

[19] M. Sørensen, O. Franek; S. K. Christensen; G. F. Pedersen; H. Ebert, “Assessment of the Usability of the Workbench Faraday Cage Method,” *IEEE International Symposium on Electromagnetic Compatibility*, pp. 399-404, Aug. 14-19, 2011.

[20] M.J. Coenen, "Common Mode Impedance Measurements on Cables in the Frequency Range 30 MHz–1 GHz," EIE 92004, Philips Semiconductors 1992.

SECTION

2. CONCLUSIONS AND RECOMMENDATIONS

In the first paper of this dissertation, analysis of the rotating permanent magnet in terms of its efficiency was conducted. It was demonstrated that the rotating magnet source outperforms a conventional coil source by a large margin (23 dB of field strength for the same volume and dissipated power), which might be a considerable advantage for low size, weight, and power applications. A method to produce ASK signals using a modulation coil was proposed and analyzed.

In the second paper of this dissertation, methods were developed to estimate an equivalent representation of sources from near-field scans of the electric fields. This representation was evaluated based on its ability to estimate fields both above the scan plane and next to the DUT when the scans were noisy and only performed in a plane above the DUT. The proposed reconstruction method was validated with measurements of a test board containing a buffer IC. The representation was shown to accurately predict fields at locations both above and to the side of the DUT with less than a 3.5 dB average error for this test case.

In the third paper of this dissertation, methods were developed to estimate an equivalent dipole representation of sources from near-field scans of the electric and magnetic fields. This dipole representation was evaluated based on its ability to estimate the fields above the scan plane, the fields next to the DUT, and the total radiated power. The impact of three major sources of error in near field scans: random measurement noise, cross field coupling, and position error, was investigated on field prediction. A clear decision-making process with examples is provided to guide the user toward selection of the "best" representation.

In the fourth paper, an analysis of an imbalanced two- or three-wire VHF LISN was conducted in terms of its mode conversion and termination impedance. It was demonstrated that an imbalanced termination impedance provides a specified degree of conversion from differential- to common-mode, which can lead to more representative radiated emission test results. For ensuring spectral emission control, an imbalanced LISN is needed. An imbalanced two or three-wire VHF LISN was prototyped.

In the fifth paper, a post processing method was implemented to investigate the effects of complex termination on radiated emission. Post processing part performed with a simple code in MATLAB. The method provides an opportunity to consider the effect of complex termination on test result without needing to repeat full wave simulation or measurement. Using this method, the uncertainty based on the tolerance of terminating impedance is calculated to be about 5 dB for two or three-wire setup. Including termination condition for two or three-wire setup, the SCU was calculated to be about 10 dB. This is about 5.5 dB lower than 15.5 dB which is currently defined in CISPR 16-4-1.

BIBLIOGRAPHY

[1] M. C. Domingo, "Magnetic Induction for Underwater Wireless Communication Networks," *IEEE Trans. on Antennas and Propagation*, vol. 60, no. 6, June 2012.

[2] V. R Challal, J. Oscar, M. Miranda and D. P Arnold, "Wireless power transmission to an electromechanical receiver using low-frequency magnetic fields," *Smart Materials and Structures*, vol. 21, pp. 1-11, 2012.

[3] A. Kurs, A. Karalis, R. Moffatt, J. D. Joannopoulos, P. Fisher and M. Soljavcic, "Wireless power transfer via strongly coupled magnetic resonances," *Science*, vol. 317, pp. 83–86, Jul. 6, 2007.

[4] F. C. Flack, E. D. James, and D. M. Schlapp, "Mutual inductance of air-cored coils - effect on design of radio-frequency coupled implants," *Med. Biol. Eng. Computer*, pp. 79–85, Jan. 1971.

[5] R. Bansal, "Near-field magnetic communication," *IEEE Antennas and Propagation Magazine*, vol 46, no. 2, April 2004.

[6] C. Bunszel, "Magnetic induction: a low-power wireless alternative," *RF Design*, vol. 24, no. 11, pp. 78-80, November 2001.

[7] M. P. Theodoridis and S. V. Mollov, "Distant Energy Transfer for Artificial Human Implants," *IEEE Trans. On Biomedical Engineering*, vol. 52, no. 11, pp. 1931-1938, Nov. 2005.

[8] G.Wang, W. Liu, M. Sivaprakasam, and G. Kendir, "Design and analysis of an adaptive transcutaneous power telemetry for biomedical implants," *IEEE Trans. Circuits Syst. I*, Reg. Papers, vol. 52, no. 10, pp. 2109–2117, Oct. 2005.

[9] Zhi Sun and Ian F. Akyildiz, "Underground Wireless Communication using Magnetic Induction," *ICC'09 Proceedings of the 2009 IEEE international conference on Communications*, pp. 4234-4238, June 2009.

[10] N. D. N. Donaldson and T. A. Perkins, "Analysis of resonant coupled coils in the design of radio frequency transcutaneous links," *Med. Biol. Eng. Comput*er, vol. 21, no. 5, pp. 612–627, Sep. 1983.

[11] H. Jiang, J. Zhang, D. Lan, K. K. Chao, S. Liou, H. Shahnasser, R. Fechter, S. Hirose, M. Harrison, and S. Roy, "A Low-Frequency Versatile Wireless Power Transfer Technology for Biomedical Implants," *IEEE Trans. on biomedical circuits and systems*, vol. 7, no. 4, August 2013.

[12] O. C. Fawole, and M. Tabib-Azar, “An Electromechanically Modulated Permanent Magnet Antenna for Wireless Communication in Harsh Electromagnetic Environments,” *IEEE Trans. on Antennas and Propagation*, vol. 65, no. 12, pp. 6927-6936, Dec. 2017.

[13] Andrew J. Petruska and Jake J. Abbott, “Optimal Permanent-Magnet Geometries for Dipole Field Approximation,” *IEEE Trans. on Magnetics*, vol. 49, no. 2, Feb. 2013.

[14] K&J Magnetics, Inc. [Online]. Available: https://www.kjmagnetics.com/proddetail.asp?prod=R6036DIA

[15] NdFeB HM Motor Large torque 615 Hollow cup motor 3.4-3.7V 52000-56000 RPM Hot, “https://www.ebay.com/i/322427122000?chn=ps”.

[16] R. DeVore and P. Bohley, “The electrically small magnetically loaded multiturn loop antenna,” *IEEE Trans. On Antennas and Propagation*, vol. AP-25, no. 4, pp. 496–505, Jul. 1977.

[17] B. E. Huey and A. L. Anderson, “Active Field Cancellation to Prevent Saturation in Ferromagnetic-Core Loop Antennas,” *IEEE Trans. On Electromagnetic Compatibility*, vol. 60, no. 6, pp. 1686–1699, Dec. 2018.

[18] Y. Cho, S. Lee, D. H. Kim, H. Kim, C. Song, S. Kong, J. Park, C. Seo, and J. Kim, “Thin Hybrid Metamaterial Slab with Negative and Zero Permeability for High Efficiency and Low Electromagnetic Field in Wireless Power Transfer Systems,” *IEEE Trans. on Electromagnetic Compatibility*, vol. 60, no. 4, pp. 1001-1009, August 2018.

[19] H. GUO, Z. SUN, J. Sun, AND N. M. Litchinitser, “M2I: Channel Modeling for Metamaterial-Enhanced Magnetic Induction Communications,” *IEEE Trans. On Antennas and Propagation*, vol. 63, no. 11, pp. 5072-5087, Nov. 2015.

[20] V. P. Pathak, V. Kumar, and R. K. Barik, “Magnetic Induction Communication based Transceiver Coil and Waveguide Structure Modeling for Non-Conventional WSNs,” *International Conference on Computing, Communication and Network Technologies (ICCCNT)*, vol. 60, no. 6, pp. 1–7, July 2018.

[21] H. Guo and Z. Sun, “Full-duplex Metamaterial-enabled Magnetic Induction Networks in Extreme Environments,” *IEEE Conference on Computer Communications (IEEE INFOCOM)*, pp. 558-566, April 2018.

[22] H.-J. Kim, J. Park, K.-S. Oh, J. P. Choi, J. E. Jang, and J.-W. Choi, “Near-Field Magnetic Induction MIMO Communication Using Heterogeneous Multipole Loop Antenna Array for Higher Data Rate Transmission,” *IEEE Trans. on Antennas and Propagation*, vol. 64, no. 5, pp. 1952-1962, May 2016.

[23] F. Fiorillo, “Measurement and Characterization of Magnetic Materials,” Amsterdam: Elsevier, 1st edition, 2004, pp. 106-108.

[24] Magneto-static solver in CST [Online]. Available: https://www.cst.com/products/cstems/solvers/solvermagnetostatics.

[25] P. Wilson, “On Correlating TEM Cell and OATS Emission Measurements,” *IEEE Transaction on Electromagnetic Compatibility*, vol. 37, no. 1, pp. 1-16, Feb. 1995.

[26] Z. Yu, J. A. Mix, S. Sajuyigbe, K. P. Slattery and J. Fan, “An improved dipole-moment model based on near-field scanning for characterizing near-field coupling and far-field radiation from an IC,” *IEEE Transaction on Electromagnetic Compatibility*, vol. 55, no. 1, pp. 97-108, Feb. 2013.

[27] M. Sørensen, I. B. Bonev, O. Franek and G. F. Pedersen, "Assessment of the Huygens’ Box Method with Different Sources Near Obstacles," in *IEEE Transactions on Electromagnetic Compatibility*, vol. 62, no. 2, pp. 433-442, April 2020.

[28] L. Li, J. Pan, C. Hwang, G. Cho, H. Park, Y. Zhang, J. Fan, “Near-field Coupling Estimation by Source Reconstruction and Huygens's Equivalence Principle”, *IEEE Symposium on Electromagnetic Compatibility and Signal Integrity, pp. 324-329, March, 2015.*

[29] R. Rafiee Alavi, A. Kiaee, R. Mirzavand, P. Mousavi, “Locally Corrected Nyström Technique and Its Relationship with RWG Method of Moment for Current Reconstruction Using Very-Near-Field Measurements”, *11th European Conference on Antennas and Propagation (EUCAP)*, pp. 319-323, March 2017.

[30] Y. Álvarez, F. Las-Heras, M. Rodríguez Pino, “Reconstruction of Equivalent Currents Distribution Over Arbitrary Three-Dimensional Surfaces Based on Integral Equation Algorithms,” *IEEE Transaction on Antennas and Propagation*, vol. 55, no. 12, Dec. 2007.

[31] Q. Huang, L. Li, X. Yan, B. Bae, H. Park, C. Hwang, J. Fan, “MoM-Based Ground Current Reconstruction in RFI Application,” *IEEE Transaction on Electromagnetic compatibility*, vol. 60, no. 4, August 2018.

[32] Q. Huang, T. Enomoto, S. Seto, K. Araki, J. Fan, C. Hwang, “A Transfer Function Based Calculation Method for Radio Frequency Interference,” *IEEE Transaction on Electromagnetic compatibility*, vol. 61, no. 4, August 2019.

[33] S. M. Rao, D. R. Wilton, A. W. Glisson, “Electromagnetic Scattering Surface of Arbitrary Shape,” *IEEE Transaction on Antennas and Propagation*, vol. AP-30, no. 3, May 1982.

[34] J. Meiguni, M. Kamyab, and A. Hosseinbeig, "Theory and experiment of spherical aperture coupled antennas," *IEEE Tran. Antennas Propagation,* vol. 61, 2013.

[35] Walton C. Gibson, "The method of Moment in Electromagnetics", Chapman and Hall/CRC, Taylor and Francis Group, 2014.

[36] Z. Yu, J. A. Mix, S. Sajuyigbe, K. P. Slattery, and J. Fan, "An Improved Dipole-Moment Model Based on Near-Field Scanning for Characterizing Near-Field Coupling and Far-Field Radiation From an IC", *Transaction on Electromagnetic Compatibility*, Vol. 55, No. 1, pp. 97-108, Feb. 2013.

[37] R. Kress, Numerical Analysis. New York: Springer-Verlag, 1998.

[38] H. Rezaei, J. Meiguni, M. Soerensen, J. Fan, D. Pommerenke, "Source Reconstruction in Near Field Scanning using Inverse MoM for RFI Application", *IEEE International Symposium on Electromagnetic Compatibility, Signal & Power Integrity (EMC+ SIPI)*, pp. 584-589, July, 2019.

[39] L. Zhang, D. Pommerenke, and J. Fan, "Determining Equivalent Dipoles Using a Hybrid Source-Reconstruction Method for Characterizing Emissions from Integrated Circuits", *IEEE Tran. on Elec. Comp.*, vol. 59, no. 2, April 2017.

[40] "CST microwave studio," [Online]. Available: https://www.cst.com

[41] M. Sorensen, O. Franek, G. Frolund Pedersen, A. Radchenko, K. Kam, and D. Pommerenke, "Estimate on the uncertainty of predicting radiated emission from near-field scan caused by insufficient or inaccurate near-field data", *International Symposium on Electromagnetic Compatibility - EMC EUROPE*, Sep. 2012.

[42] J. Ming Jin, "Theory and Computation of Electromagnetic Fields," in Magnetism, *Second Edition. Wiley*, 2015, pp. 94–101.

[43] J. Zhang, K. Keong, M. Jin, V. Khilkevich, D. Pommerenke, and J. Fan, "An effective method of probe calibration in phase-resolved near-field scanning for EMI application," *IEEE Transaction on Instrumentation and Measurement*, vol. 62, no. 3, pp. 648–658, Mar. 2013.

[44] A high-performance differential 1:4 CML fanout buffer with a selectable Equalizer receiver [online]. Available: "https://www.onsemi.com/pub/Collateral/NB7HQ14M-D.PDF"

[45] H. Rezaei, J. Meiguni, M. Sørensen, R. Jobava, V. Khilkevich, J. Fan, D. G. Beetner, D. Pommerenke, "Source Reconstruction in Near Field Scanning using Inverse MoM for RFI Application," IEEE Transaction on Electromagnetic compatibility, pp. 1628-1636, vol. 62, no. 4, August 2020.

[46] Y. F. Shu, X. C. Wei, R. Yang, and E. X. Liu, "An iterative approach for EMI source reconstruction based on phase less and single-plane near-field scanning," *IEEE Trans. Electromagnetic Compat.*, vol. 60, no. 4, pp. 937–944, Aug. 2018.

[47] L. Wang, Y. Zhang, F. Han, J. Zhou, Q. Huo Liu, "A phase less Inverse Source Method (PISM) Based on Near-Field Scanning for Radiation Diagnosis and Prediction of PCBs", *IEEE Transactions on Microwave Theory and Techniques*, vol: 68, no. 10, pp: 4151 – 4160, Oct. 2020.

[48] W. Labiedh, J. Ben Hadj Slama, "Analysis and Modeling of the Magnetic Near Fields Emited by an IGBT and by a Power Diode Generic Radi ating Model for Active Components", *International Conf. on Electrical Sciences and Technologies in Maghreb (CISTEM)*, Nov. 2014.

[49] L. Li, J. Pan, C. Hwang, and J. Fan, "Radiation Noise Source Modeling and Application in Near-Field Coupling Estimation", *IEEE Trans. On Electromagnetic Compatibility*, vol. 58, no. 4, pp. 1314-1321, Aug. 2016.

[50] C. Wu, Z. Sun, Q. Huang, Y. Wang, J. Fan, J. Zhou, "A Method to Extract Physical Dipoles for Radiating Source Characterization and Near Field Coupling Estimation", *IEEE International Symposium on Electromagnetic Compatibility, Signal & Power Integrity (EMC+ SIPI)*, pp. 580-583, 2019.

[51] M. M. Hernando, A. Fernandez, M. Arias, M. Rodriguez, Y. Alvarez, and F. Las-Heras, "EMI radiated noise measurement system using the source reconstruction technique", *IEEE Trans. Ind. Electron.*, vol. 55, no. 9, pp. 3258–3265, 2008.

[52] Z. Yu, Mei Chai, Jason A. Mix, Kevin P. Slattery, and Qing Huo Liu, "Inverse Source Solver for a High Resolution Near Field Scanner in Microelectronic Applications", *IEEE Trans. On Components, Packaging and Manufacturing Technology*, vol. 4, no. 9, SEP. 2014.

[53] H. Zhao, Sihong Tao, Zhizhang Chen, and Jun Hu, "Sparse Source Model for Prediction of Radiations by Transmission Lines on a Ground Plane Using a Small Number of Near-Field Samples", *IEEE Antennas and Wireless Propagation Letters*, vol. 18, no. 1, Jan. 2019.

[54] K. Kwak1, Tae-il Bae, Kichul Hong, Hyungsoo Kim, Jingook Kim, "Accuracy investigation of equivalent dipole arrays for near-field estimation in presence of shielding or dielectric structures," *Microw Opt Technol Lett.*, pp. 1-9., 2019.

[55] J. Pan, H. Wang, X. Gao, C. Hwang, E. Song, H.-B. Park, and J. Fan, "Radio-Frequency Interference Estimation Using Equivalent Dipole-Moment Models and Decomposition Method Based on Reciprocity", *IEEE Trans. On Electromagnetic Compatibility*, vol. 58, no. 1, pp. 75-84, Feb. 2016.

[56] H. Zhao, X. Li, Z. Chen, and J. Hu, "Skeletonization-Scheme-Based Adaptive Near Field Sampling for Radio Frequency Source Reconstruction", *IEEE Internet of Things Journal*, vol. 6, no. 6, pp. 10219-10228, Dec. 2019.

[57] S. Lee , Y. Zhong , Q. Huang, T. Enomoto, S. Seto, K. Araki, J. Fan, and C. Hwang, "Analytical Intra-System EMI Model using Dipole Moments and Reciprocity", *IEEE Asia-Pacific Symposium on Electromagnetic Compatibility (EMC/APEMC)*, May 2018.

[58] X. C. Wei, Y. F. Shu, Z. K. Hu, Y. H. Zhong, Y. W. Wang, "A Summary of Artificial Neural Networks on Electromagnetic Interference Diagnosis", *International Conference on Microwave and Millimeter Wave Technology (ICMMT)*, 19-22 May 2019.

[59] Y. F. Shu, X. C. Wei, J. Fan, R. Yang, Y. B. Yang, "An Equivalent Dipole Model Hybrid With Artificial Neural Network for Electromagnetic Interference Prediction", *IEEE Transactions on Microwave Theory and Techniques*, pp: 1790-1797, vol.: 67, no: 5, May 2019.

[60] Z. K. Hu, Y. H. Zhong, Y. W. Wang, Y. F. Shu, X. C. Wei, "Application of Artificial Neural Network for Electromagnetic Source Reconstruction:, *IEEE International Conference on Computational Electromagnetics*, 20-22 March 2019.

[61] Z. K. Hu, Y. H. Zhong, X. C. Wei, Y. W. Wang, Y. F. Shu, "A Novel Electromagnetic Interference Source Reconstruction Method based on Artificial Neural Network", *12th International Symposium on Antennas, Propagation and EM Theory (ISAPE)*, Dec. 2018.

[62] J. He, Q. Huang, J. Fan, "Dipole Source Reconstruction By Convolutional Neural Networks", *IEEE International Symposium on Electromagnetic Compatibility & Signal/Power Integrity (EMCSI)*, July 2020.

[63] Q. Huang, J. Fan, "Machine Learning Based Source Reconstruction for RF Desense", *IEEE Transactions on Electromagnetic Compatibility*, vol. 60, no. 6, pp: 1640-1647, Dec. 2018.

[64] A. P. Duffy, A. J. M. Martin, A. Orlandi, G. Antonini, T. M. Benson, and M. S. Wolfson, "Feature selective validation of computational electronics (CEM), Part I—The FSV method", *IEEE Transaction on Electromagnetic Compatibility*, vol. 48, no. 3, pp. 449-459, Aug. 2006.

[65] S. Yang, Q. Huang, G. Li, R. Zoughi, and D. J. Pommerenke, "Differential E-Field Coupling to Shielded H-Field Probe in Near-Field Measurement and a Suppression Approach", *IEEE Transaction on Instrumentation and Measurement*, vol. 67, no. 12, pp. 2872-2880, Dec. 2018.

[66] E. Petritoli, F. Leccese, L. Ciani, G. Schirripa Spagnolo, "Probe Position Error Compensation in Near-field to Far-field Pattern Measurements", *IEEE 5th International Workshop on Metrology for Aerospace*, June 2019.

[67] S. F. Razavi and Y. Rahmat-Samii, "Resilience to probe-positioning errors in planar phase less near-field measurements," *IEEE Trans. Antennas Propagation*, vol. 58, no. 8, pp. 2632–2640, 2010.

[68] R. He, Y. Xu, S. Walunj, S. Yong, V. Khilkevich, D. Pommerenke, H. L Aichele, M. Boettcher, P. Hillenbrand, A. Klaedtke, "Modeling Strategy of EMI Filters", *IEEE Transaction on Instrumentation and Measurement*, vol. 62, no. 4, July 2020.

[69] "CST microwave studio," [Online]. Available: https://www.cst.com

[70] X. Tong, D. W. P. Thomas, A. Nothofer, C. Christopoulos, and P. Sewell, "Reduction of Sensitivity to Measurement Errors in the Derivation of Equivalent Models of Emission in Numerical Computation", *ACES Journal*, pp.: 603-610, vol. 26, no. 7, July 2011.

[71] CISPR 35: *2016, Electromagnetic compatibility of multimedia equipment - Immunity requirements.*

[72] K. Osabe, N. Kuwabara, S. Okuyama, "Termination Impedance for AC Mains Cable Leaving from EUT Area in Radiated Emission Measurement", *International Symposium on Electromagnetic Compatibility - EMC EUROPE*, Angers, France, pp. 1-6, Sep. 4-8, 2017.

[73] S. Okuyama, K. Osabe, N. Kuwabara, H. Muramatsu, "Influence of Disturbance Current Mode on Correlation between Radiation Test Sites Using VHF-LISN and CMAD," *International Symposium on Electromagnetic Compatibility (EMC Europe)*, Amsterdam, The Netherlands, Aug. 27-30, 2018.

[74] C. Miyazaki, K. Tanakajima, M. Yamaguchi, "A Round-robin Test on Effectiveness of a VHF LISN for Radiated Emission measurements", *IEEE International Symposium on Electromagnetic Compatibility*, pp. 14-19, Aug. 2011.

[75] S. Okuyama, K. Osabe, K. Tanakajima, H. Muramatsu, "Investigation on Effectiveness of Very High Frequency Line Impedance Stabilization Network (VHF-LISN) for Measurement Reproducibility," *International Symposium on Electromagnetic Compatibility, Brugge*, Belgium, Sep. 2-6, 2013.

[76] S. Okuyama, N. Kuwabara, M. Yamaguchi, K. Osabe "Improvement in the Reproducibility of Radiated Emission Measurements in a Fully Anechoic Room by Using VHF-LISN to Control the Termination Condition of the AC Mains Cable Leaving the EUT," *Asia-Pacific International Symposium on Electromagnetic Compatibility (APEMC)*, pp. 50-52, May 17-21, 2016.

[77] S. Okuyama, N. Kuwabara, K. Osabe, H. Muramatsu, “Improvement of Radiated Emission Measurement Reproducibility with VHF-LISN Obtained from Final Results of International Inter-laboratory Comparison on Termination Control of Power Line,” *Asia-Pacific Symposium on Electromagnetic Compatibility (APEMC)*, pp. 589-592, May 26-29, 2015.

[78] C. Miyazaki, K. Tanakajima, M. Yamaguchi, S. Satake, J. Kawano, “Improvement of Dispersion of Radiated Emission Measurement Results by VHF-LISN,” *IEEE International Symposium on Electromagnetic Compatibility*, pp. 1-4, Aug. 18-22, 2008.

[79] Y. C. Tang, J. S. Chen, C. H. Lee, C. N. Chiu, “A Case Study on the Consistency Improvement in Radiated-Emission Testing by Using LISN,” *International Symposium on Electromagnetic Compatibility*, Tokyo, pp. 259-262, May, 2014.

[80] CISPR/I/WG2, “Artificial Mains Networks for the boundary of the EMC test volume,” *A supporting paper on CISPR/I/541/CD*, August 2017.

[81] D. M Lauder, R. C Marshall, “Measurement Uncertainty and Cable Balance-with Implications for the CDNE-M,” *International Symposium on Electromagnetic Compatibility*, pp. 251-254, Sep. 2014.

[82] S. B. Worm, “On the relation between radiated and conducted RF emission tests”, *13th International, Zurich Symposium & Technical Exhibition on EMC*, pp. 515-520, Feb. 16-18, 1999.

[83] M. Sørensen, O. Franek; S. K. Christensen; G. F. Pedersen; H. Ebert, “Assessment of the Usability of the Workbench Faraday Cage Method,” *IEEE International Symposium on Electromagnetic Compatibility*, pp. 399-404, Aug. 14-19, 2011.

[84] Richard Thompson, “Comparing NPL measurements between OATS and GTEM with Worm,” NPL, 25th July 2008. Informal circulation to interested parties.

[85] Available online at: https://www.keysight.com.

[86] CISPR/TR 16-1-2, Specifications for radio disturbance and immunity measuring apparatus and method.

[87] Available online at: https://www.cst.com/company/news/press-releases/agilent-technologies-and-cst-announce-integration-advances-for-rf-and-microwave-circuit-design.

[88] K. Osabe, N. Kuwabara, H. Muramatsu, “Impacts to Measurement Uncertainty of Radiated EMI Measurement by Setting Terminating Condition of AC Mains Cable Leaving from Test Area” *IEEE Asia-Pacific Symposium on Electromagnetic Compatibility (EMC/APEMC)*, May, 2018.

[89] CISPR/TR 16-4-1, Specifications for radio disturbance and immunity measuring apparatus and method- Part 4-1: Uncertainties, statistics, and limit modelling – Uncertainties in standardized EMC tests.

[90] Available online at: https://www.matlab.com.

[91] CISPR/I/WG2, “Artificial Mains Networks for the boundary of the EMC test volume,” *A supporting paper on CISPR/I/541/CD*, August 2017.

[92] “CISPR 22”, Information technology equipment -Radio disturbance characteristics- Limits and methods of measurement, Edition 5.2, 2006-03.

[93] S.J. Mason, Feedback theory – Some properties of signal flow graphs, Proc. IRE 41 (1953) 1144–1156.

[94] CISPR 16-1-2 Edition 1.2, Table 7.2 “Characteristics of the asymmetric artificial network”.

[95] M.J. Coenen, "Common Mode Impedance Measurements on Cables in the Frequency Range 30 MHz–1 GHz," EIE 92004, Philips Semiconductors 1992.

VITA

Hossein Rezaei received his B.E. degree in electrical engineering from Islamic Azad University Najafabad Branch (IAUN), Najafabad, Iran, in 2004, and his M.S. degree in electrical engineering from Shiraz University of Technology (SUTech), Shiraz, Iran, in 2011. He received his Ph.D. degree in electrical engineering from the EMC Laboratory, Missouri University of Science and Technology, Rolla, USA in May 2021. His research interests included electromagnetic compatibility, signal integrity, electromagnetic susceptibility, RF desense, and numerical simulation.